Spectroscopy and X-ray Storage Capability of Rare-Earth Ions Doped and Undoped BaLiF3

Author:
Chowdhury, Nishita

Publication Date:
2022

DOI:
https://doi.org/10.26190/unsworks/1999

Spectroscopy and X-ray Storage Capability of Rare-Earth Ions Doped and Undoped $BaLiF_3$

Nishita Chowdhury

A thesis submitted in partial fulfillment of the requirements

for the degree of Doctor of Philosophy

School of Science

The University of New South Wales, Canberra

February 2022

Thesis/Dissertation Sheet

Surname/Family Name	:	**CHOWDHURY**
Given Name/s	:	**NISHITA**
Abbreviation for degree as give in the University calendar	:	**Ph.D.**
Faculty	:	**University of New South Wales, Canberra**
School	:	**School of Science**
Thesis Title	:	**Spectroscopy and X-ray Storage Capability of Rare-Earth Ions Doped and Undoped $BaLiF_3$**

Abstract 350 words maximum

Storage phosphors have found widespread applications in dosimetry and computed radiography. To date, BaFBr(I):Eu^{2+} is the most commercially successful phosphor used in computed radiography. Due to their limited signal to noise ratio and erasure of stored information, investigations of alternative phosphor materials are crucial and $BaLiF_3$ has emerged as a potential candidate.

This thesis focuses on a thorough understanding of the luminescence phenomena and X-ray storage capability of single-doped ($BaLiF_3$:Eu^{3+}, $BaLiF_3$:Sm^{3+} and $BaLiF_3$:Tm^{3+}), co-doped ($BaLiF_3$:Yb^{3+}, Er^{3+}), and undoped $BaLiF_3$. The doped and undoped $BaLiF_3$ powder were prepared by ball milling and characterized using powder X-ray diffraction, transmission and scanning electron microscopy, energy dispersive spectroscopy and X-ray photoelectron spectroscopy. Their optical properties were characterized by photoluminescence, upconversion luminescence and photoluminescence excitation spectroscopy in external magnetic field (9 T). Photoluminescence properties of nanocrystalline $BaLiF_3$:Eu^{3+}, $BaLiF_3$:Sm^{3+} and $BaLiF_3$:Tm^{3+} before and after X-irradiation was studied to quantify their X-ray storage capability of such host-activator systems. It is demonstrated that $BaLiF_3$ is a potential host which can enable luminescence within a broad optical range (UV–infrared) depending on the activator. In addition, upconversion luminescence in $BaLiF_3$:Yb^{3+}, Er^{3+} was investigated and shown to increase by 2 orders of magnitude upon treatment by annealing at higher temperatures. Furthermore, the reduction of Er^{3+} upconversion luminescence as well as Yb^{3+} and Er^{3+} photoluminescence in $BaLiF_3$:Yb^{3+}, Er^{3+} as a function of increasing X-ray doses were explored in detail. It is demonstrated that Yb^{3+} and Er^{3+} co-doped $BaLiF_3$ exhibits desirable sensitivity to X-ray radiation. 2D X-ray images were recorded based on the observed upconversion luminescence which demonstrated their potential for X-ray imaging along with dosimetry. Finally, a F_3^+ colour centre is reported in undoped $BaLiF_3$ upon annealing, which display a zero-phonon line at 764.8 nm. The zero-phonon line exhibited Zeeman effects in large magnetic fields due to a triplet ground state. This is the first observation of singlet to triplet luminescence of colour centre. The photoluminescence properties and X-ray storage capability of the F_3^+ centre was rigorously explored.

Significantly, this thesis advances the understanding of luminescent properties of activated and pure $BaLiF_3$ and sheds light on the utilization of these nanocrystals for practical implementations.

ORIGINALITY STATEMENT

'I hereby declare that this submission is my own work and to the best of my knowledge it contains no materials previously published or written by another person, or substantial proportions of material which have been accepted for the award of any other degree or diploma at UNSW or any other educational institution, except where due acknowledgement is made in the thesis. Any contribution made to the research by others, with whom I have worked at UNSW or elsewhere, is explicitly acknowledged in the thesis. I also declare that the intellectual content of this thesis is the product of my own work, except to the extent that assistance from others in the project's design and conception or in style, presentation and linguistic expression is acknowledged.'

Signed …….....

Date …….....

INCLUSION OF PUBLICATIONS STATEMENT

UNSW is supportive of candidates publishing their research results during their candidature as detailed in the UNSW Thesis Examination Procedure.

Publications can be used in their thesis in lieu of a Chapter if:

- The candidate contributed greater than 50% of the content in the publication and is the "primary author", ie. the candidate was responsible primarily for the planning, execution and preparation of the work for publication
- The candidate has approval to include the publication in their thesis in lieu of a Chapter from their supervisor and Postgraduate Coordinator.
- The publication is not subject to any obligations or contractual agreements with a third party that would constrain its inclusion in the thesis

Please indicate whether this thesis contains published material or not:

☐ This thesis contains no publications, either published or submitted for publication
(if this box is checked, you may delete all the material on page 2)

☒ Some of the work described in this thesis has been published and it has been documented in the relevant Chapters with acknowledgement
(if this box is checked, you may delete all the material on page 2)

☐ This thesis has publications (either published or submitted for publication) incorporated into it in lieu of a chapter and the details are presented below

CANDIDATE'S DECLARATION

I declare that:

- I have complied with the UNSW Thesis Examination Procedure
- where I have used a publication in lieu of a Chapter, the listed publication(s) below meet(s) the requirements to be included in the thesis.

Candidate's Name	Signature	Date (dd/mm/yy)

Dedication

To my Super Mom Mrs. Juthika Chowdhury who always sacrificed her special moments and comforts to ensure a secured life and better future for me.

Acknowledgements

First and foremost, I am indebted to my supervisor, Professor Hans Riesen for providing me the golden opportunity to pursue my PhD research on a fascinating and innovative field. His extensive research experience, sincerity and dedication to research always inspire me. I am deeply indebted to him for his constant support, motivation, appreciation and for driving me into the depth of this research field. He taught me how to execute a new research idea even with limited resources, which will be a hallmark in my future endeavours. I am grateful to him for helping me in progressing in my research by providing feedback, suggestions and guideline. In our personal interaction I have found him as a person with high integrity, and I feel fortunate to have him as my supervisor who made my PhD journey memorable.

I would like to thank my co-supervisor Dr. Wayne Hutchison for his support during my PhD journey. I gratefully acknowledge his kind help with the Zeeman experiment.

I would like to express my sincere gratitude to Dr. Nicolas Riesen from the University of South Australia for his great support with scanning electron microscopy, transmission electron microscopy and energy dispersion spectroscopy. I also thank him for his valuable suggestions and feedback on my manuscripts.

I would like to express gratitude to Professor Elmars Krausz, Julien Langley, and Dr. Robin Purchase from the Australian National University (ANU) for their help with preliminary Zeeman experiment. I would also like to thank Dr. Bin Gong from the University of New South Wales Mark Wainwright Analytical Centre for his help with the X-ray photoelectron spectroscopy.

On a personal level, I would like to convey gratitude to my colleagues Siti Rozaila Zahariman and Norfadira Wahib for their friendship.

Special thanks of gratitude to the people of science mechanical workshop of UNSW Canberra, whose technical support is vital for my project. I specifically acknowledge the great support of Phillip Donohue and Todd Bell throughout my PhD project.

I would also like to thank Ms. Kate Badek for her help from the beginning of my PhD and Dr. Barry Gray for his assistance regarding building and supply matters. Special thanks to Dr. Anthony Day, Professor Clifford Woodward and Dr. Lynne Wallace for sharing laboratory resources. I am grateful to all the UNSW administrative staffs for their kind co-operation during my candidature.

My heartfelt gratitude goes to the University of New South Wales for providing me the University International Postgraduate Award and the HDR completion scholarship which made it possible to complete my PhD study.

Special thanks to my husband Dr. Shimul Kanti Nath who always have had trust in my potential and continuously encouraged me to pursue my dreams. He has been the greatest support system during my tough periods and a constant motivator in my life.

I am extremely thankful to my parents Mrs. Juthika Chowdhury and Mr. Narayan Chowdhury for their unconditional love, care and sacrifices for bringing me up and providing their unwavering support to complete my education. I am highly grateful to my brother-in-law Mr. Anupam Chowdhury, my sister Mrs. Esita Chowdhury and my lovely niece Adrisha Chowdhury for their support, love and care. Special thanks to my uncle Mr. Pradip Kumar Das for his unconditional love and support in every sphere of my life.

Finally, thanks to my God (my Bhagavan) for his greatness, blessings and mercy.

List of Publications

1. **N. Chowdhury**, N. Riesen, and H. Riesen, 'Efficient Generation of Stable Sm^{2+} in Nanocrystalline $BaLiF_3$:Sm^{3+} by UV- and X-Irradiation', **The Journal of Physical Chemistry C**, Vol. 123, No. 41, pp. 25477-25481 (2019).

2. **N. Chowdhury**, N. Riesen, and H. Riesen, 'Yb^{3+} and Er^{3+} Codoped $BaLiF_3$ Nanocrystals for X-ray Dosimetry and Imaging by Upconversion Luminescence', **ACS Applied Nano Materials**, Vol. 4, No. 7, pp. 6659-6667 (2019).

3. **N. Chowdhury**, N. Riesen, and H. Riesen, 'Photoluminescence of X-ray-Induced Divalent Tm Ions in $BaLiF_3$:Tm^{3+} Nanocrystals', **The Journal of Physical Chemistry C**, Vol. 125, No. 39, pp. 21543-21549 (2021).

4. **N. Chowdhury**, W. Hutchison, N. Riesen, E. Krausz and H. Riesen, 'Spin-Forbidden Near-Infrared Luminescence from a F_3^+ Colour Centre Generated in Mechanochemically Prepared Nanocrystalline $BaLiF_3$ upon Annealing', **Nanoscale**, (2022, in press).

Conference Presentation

N. Chowdhury, and H. Riesen, 'Efficient X-ray storage capability of Sm^{3+} doped Nanocrystalline $BaLiF_3$ and $Ba_{0.8}Sr_{0.2}LiF_3$', presented (poster) in 'International Conference on Nano Science and Nanotechnology (ICONN)', 09 February -13 February 2020, Brisbane, Australia.

Abstract

Storage phosphors have found widespread applications in the field of dosimetry and computed radiography due to their impressive properties, including large dynamic ranges and passive storage modalities. A conventional storage phosphor consists of a host lattice and an activator, and BaFBr(I):Eu^{2+} (host-activator) is the most commercially successful phosphor used in computed radiography. However, they still suffer from some drawbacks, such as limited signal to noise ratio and erasure of stored information. Consequently, investigations of alternative phosphor materials have drawn significant recent attention and rare-earth ions doped $BaLiF_3$ has emerged as a potential candidate. This thesis focuses on a thorough understanding of the luminescence phenomena and X-ray storage capability of single-doped ($BaLiF_3$:Eu^{3+}, $BaLiF_3$:Sm^{3+} and $BaLiF_3$:Tm^{3+}), co-doped ($BaLiF_3$:Yb^{3+}, Er^{3+}) and undoped $BaLiF_3$. The doped and undoped $BaLiF_3$ powders were prepared by ball milling method and characterized using powder X-ray diffraction, transmission electron microscopy (TEM), scanning electron microscopy (SEM) , TEM and SEM energy dispersive spectroscopy (EDS) and X-ray photoelectron spectroscopy (XPS). Their optical properties were characterized by photoluminescence (PL) and upconversion luminescence (UCL) spectroscopy and photoluminescence excitation (PLE) spectroscopy in magnetic field up to 9 T.

Photoluminescence properties of nanocrystalline $BaLiF_3$:Eu^{3+}, $BaLiF_3$:Sm^{3+} and $BaLiF_3$:Tm^{3+} before and after X-irradiation was studied to quantify the X-ray storage capability of such host-activator systems. It is demonstrated that $BaLiF_3$ is a potential host which can enable luminescence within a broad optical range from UV to infrared depending on the activator. In addition, upconversion luminescence in $BaLiF_3$:Yb^{3+}, Er^{3+} was investigated and shown to increase by 2 orders of magnitude upon heat treatment by annealing at higher temperatures.

Furthermore, the reduction of Er^{3+} upconversion luminescence as well as Yb^{3+} and Er^{3+} photoluminescence in $BaLiF_3$:Yb^{3+}, Er^{3+} as a function of increasing X-ray doses were explored in detail. It is demonstrated that Yb^{3+} and Er^{3+} co-doped $BaLiF_3$ exhibits desirable sensitivity to X-ray radiation. Additionally, 2D X-ray images were recorded based on the observed upconversion luminescence which demonstrated their potential for X-ray based imaging along with X-ray dosimetry. Finally, a F_3^+ colour centre is reported for the first time in undoped $BaLiF_3$ upon annealing ($\geq$500 °C), which display a zero-phonon line at 764.8 nm and weak electron-phonon coupling. The zero-phonon line exhibited Zeeman effects in large magnetic fields due to a triplet ground state. To the best of our knowledge, this is the first report of singlet to triplet luminescence of colour centre. The photoluminescence properties and X-ray storage capability of the F_3^+ centre was rigorously explored.

Significantly, this thesis advances the understanding of luminescent properties of activated and pure nanocrystalline $BaLiF_3$ and sheds light on the utilization of these nanocrystals for practical implementations.

Contents

List of Figures

List of Tables

Chapter 1

Introduction

1.1 Motivation

With the technological advancements achieved in the past century, advanced X-ray-based imaging techniques have emerged as fundamental building blocks in the fields of computed radiography [1–3] and medical diagnosis [4, 5]. In early years, conventional photographic films were used for medical imaging [6, 7]. However, because of their poor response to X-irradiation, high doses were required, which have an adverse effect on human health [8]. To address this shortfall, scintillator screens were used to convert X-ray energy to visible luminescence for which conventional photographic film is much more sensitive; the photographic film then acts as the storage device [9]. Later, in the 1980s it was established that similar functionalities can be obtained by replacing the scintillator screen-film system by a storage phosphor (known as X-ray storage phosphor) coated plate which can directly store the radiation image that can be read-out by a laser based 'flying-spot' method [10].

The performance of X-ray storage phosphor based computed radiography and that of a conventional film system is compared in Figure 1.1. The storage phosphor based computed radiography technology is highly sensitive in the X-ray region, and exhibits significantly higher sensitivity by at least an order of magnitude [11] and a much higher dynamical range (10^4-10^5) for image formation [12]. Hence, high X-ray doses are no longer required in the storage phosphor based computed radiography which replaced the conventional film-screen method in

many medical imaging applications [13].

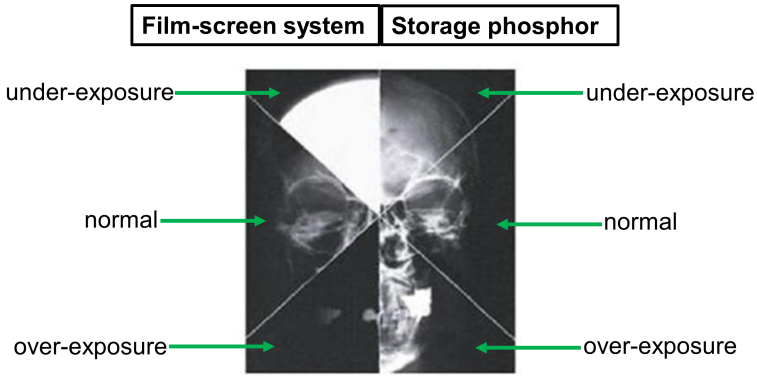

Figure 1.1: Comparison of storage phosphor based computed radiography (CR) and conventional radiography [12, 14].

Traditionally, a computed radiography (CR) system comprises five components, namely, imaging plate, optical read-out system, image processing unit, storage device and display unit [15]. It utilizes photostimulable phosphor as the imaging plates material that store radiation energy as latent images rather than producing luminescence immediately after exposure [15, 16]. The stored energy can be read-out by scanning the imaging plate with an external energy source such as a laser which stimulates the emission of trapped energy as photostimulated light [17]. Subsequently the emitted luminescence is detected by a photomultiplier tube and the signal is digitalized (by analog-to-digital converter) to form the image on a point-by-point basis [18]. Over recent decades, computed radiography has found widespread application in X-ray based imaging [15, 19], including intraoral dental imaging [1], dosimetry [20], and preventive healthcare measurements such as breast-screening programs [21, 22].

A schematic illustration of the working principle of computed radiography is shown in Figure 1.2. At first, an object in front of the phosphor coated imaging plate is exposed to X-ray radiation and the storage phosphor renders a latent image of the object by the distribution of absorbed dose; this phase is termed as 'image acquisition' [23, 24]. The absorbed dose is measured in the 'image read-out' phase by the photostimulated emission of the storage phosphor coated photographic plate by utilizing the 'flying-spot' method. In this process, a focused red helium-neon laser beam is scanned across the imaging plate and the resulting photostimulated

emission in the blue region of the visible spectrum as measured by a photomultiplier (PM) is converted pixel-by-pixel into a digital signal [13, 25]. In computed radiography, BaFBr(I):Eu^{2+} is the most commercially used photostimulable X-ray storage phosphor [19, 26]. However, this phosphor still suffers from some drawbacks such as limited spatial resolution, erasure of stored information caused by the photostimulated light, and a limited signal-to-noise ratio.

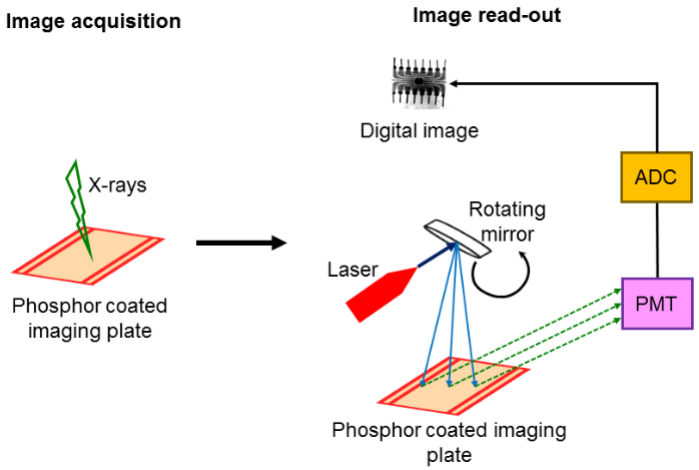

Figure 1.2: Principle of computed radiography (CR) used to convert X-ray energy to visible luminescence. An experimental object equipped with the photographic plate is exposed to X-ray. A latent image is formed on the phosphor coated photographic plate by X-ray exposure. The read-out of the photostimulated luminescence by the imaging plate is carried-out by 'flying-spot' laser.

In recent years, X-ray storage phosphors have also found widespread applications in the field of dosimetry (radiation monitoring system) [20, 27–29] due to their impressive properties, including large dynamic range, and passive storage mode [4, 5, 30].

With all these successful developments of the last 40 years in mind, realizing an efficient X-ray storage phosphor, optimizing their preparation condition, and understanding their dependence on material-specific properties are highly important for future advances.

1.2 Outline of this thesis

An X-ray storage phosphor comprises a host matrix and an activator ion which is then combined with a sensitive luminescence-stimulation system and its successful implementa-

tion mostly depends on a suitable combination of these two components [18]. Specifically, a transparent host along with a strong emitting ion as activator are the key requirements for desirable luminescence properties [12]. Importantly, the crystal structure of the host lattice significantly influences the optical properties of an activator, since different crystal structures provide different crystal field splitting and transition probabilities [11, 31]. Therefore, selecting a host matrix with an appropriate crystal structure, and an activator that well incorporates into that structure is crucial for their functioning.

The aim of this thesis is to investigate the radiation storage capability of barium lithium fluoride ($BaLiF_3$) as the host matrix activated with rare-earth elements. $BaLiF_3$ belongs to the inverse-perovskite family and was chosen because of its non-hygroscopic properties, whereas many of the halide perovskite hosts are very hygroscopic e.g., $CsPbF_3$, $CsCaF_3$, $CsSrF_3$, $CsCaCl_3$ and $CsBaCl_3$ [32–34]. Most importantly, a wide range of optically-active ions can readily be incorporated into this system which may lead to interesting luminescence phenomena [35–37]. Additionally, the inverse perovskite structure of $BaLiF_3$ is itself very interesting and may exhibit interesting optical phenomena.

The thesis is organized in 8 chapters:

Chapter 1 and **2** provide the motivation and background of rare-earth ions doped $BaLiF_3$ relevant to the objective of this thesis.

Chapter 3 describes the experimental methods employed in the thesis, including the preparation process and the spectroscopic methods utilized to study the luminescence property of doped and pure $BaLiF_3$.

Chapter 4-7 include the experimental results and discussions. Specifically, **Chapter 4** describes the UV and X-ray storage capacity of nanocrystalline $BaLiF_3$ doped with Sm^{3+} ($BaLiF_3$:Sm^{3+}) and reports on the stability of X-ray generated Sm^{2+} ions upon blue excitation light. The property of $Ba_{0.8}Sr_{0.2}LiF_3$:Sm^{3+} is also discussed in this chapter.

Chapter 5 provides infrared photoluminescence spectroscopy of nanocrystalline $BaLiF_3$ activated with Tm^{3+}. X-ray reduction ($Tm^{3+} + e^- \rightarrow Tm^{2+}$) and stability of X-ray induced Tm^{2+} in $BaLiF_3$:Tm^{3+} is presented in detail.

Chapter 6 describes the upconversion luminescence properties of Er^{3+} and Yb^{3+} co-doped nanocrystalline $BaLiF_3$. Additionally, this chapter demonstrates the performance of $BaLiF_3$:

(Er^{3+}, Yb^{3+}) for real-world applications such as X-ray imaging and X-ray dosimetry. To the best of our knowledge, this is the first report that demonstrates computed radiography by upconversion luminescence.

Chapter 7 reports on a new colour centre in pure nanocrystalline $BaLiF_3$ including its generation and stability, and sensitivity to X-ray radiation.

Chapter 8 presents a summary of this thesis with a discussion of the experimental results and their potential for applications in dosimetry, computed radiography, and solid-state laser technology.

Chapter 2

Background

2.1 Luminescence properties of X-ray storage phosphors

Storage phosphors typically absorb incident X-rays and exhibit a diverse range of luminescence phenomena when excited with an appropriate excitation source [25, 38]. Specifically, depending on the optical properties of the activator, the storage phosphor/host-activator system can display spectral emission spanning from the ultraviolet to the infrared [5, 11]. The luminescence mechanism is based on absorption and subsequent emission of photons [39, 40] where the emission can be excited by employing a range of excitation sources. Based on the energy of the incident photon relative to the emission, phosphors exhibit Stokes (incident energy > emission energy) and anti-Stokes (incident energy < emission energy) shifts [41, 42]. More explicitly, photoluminescence-based phosphors follow the Stokes law whereas photostimulated and upconversion materials typically display anti-Stokes luminescence.

2.1.1 Photoluminescence

Photoluminescence is a quantum mechanical process where a material absorbs incident photons and the energy is used to excite optical centres from the electronic ground state to an electronically excited state [43]. Subsequently, the excited state is deactivated to the ground state by the emission of a photon i.e., by photoluminescence light where the emitted photon is of lower energy than the absorbed photon. The photoluminescence process can be categorized as fluorescence and phosphorescence. Fluorescence refers to a spin allowed transition from the

excited to the ground state and in this case the spin multiplicity (S) of both states is same e.g., singlet-singlet and triplet-triplet transition. On the other hand, phosphorescence is a spin forbidden transition where the excited and ground state have different spin multiplicities i.e., spin triplet (S = 1) and spin singlet (S = 0) and the transition between these states can only happen because of spin-orbit coupling. As a consequence, phosphorescence lifetimes (typically 1 ms - 10 s) are much longer than fluorescence lifetimes (typically 0.1 - 10 ns).

In a phosphor, an activator acts as an individual atom in the host lattice and the exciting radiation is absorbed by the activator, raising it to an excited state, and returns to the ground state by emission of radiation (R) and/or nonradiative (NR) process. A basic luminescence mechanism of a phosphor material is schematically shown in Figure 2.1a and b. The principle of a photoluminescent (PL) material is shown in Figure 2.1c to illustrate the definition.

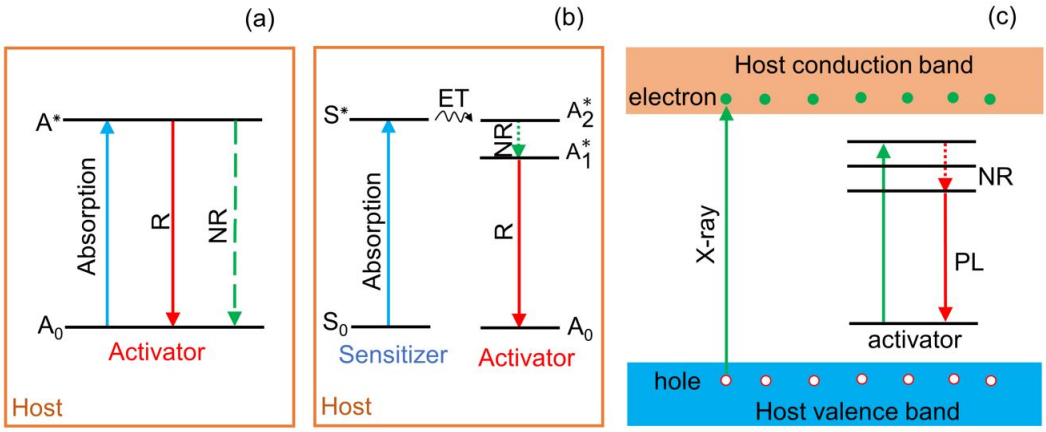

Figure 2.1: Diagram of basic luminescence mechanism of (a) direct and (b) indirect excitation in host-activator system and (c) photoluminescent (PL) phosphor.

2.1.2 Photostimulated luminescence

After absorbing high energy radiation (UV/X-ray), electrons and holes are generated that are trapped by defects in the host lattice resulting in metastable states. The electrons can be easily liberated upon exposure to long-wavelength light such as near-infrared light and recombine with the holes by resulting photostimulated luminescence (PSL) at shorter wavelength [44]. Conventional phosphor, Eu^{2+} doped BaFBr(I) displays photostimulated emission [18, 45]

upon red laser excitation. A schematic diagram of possible PSL mechanism is shown in Figure 2.2.

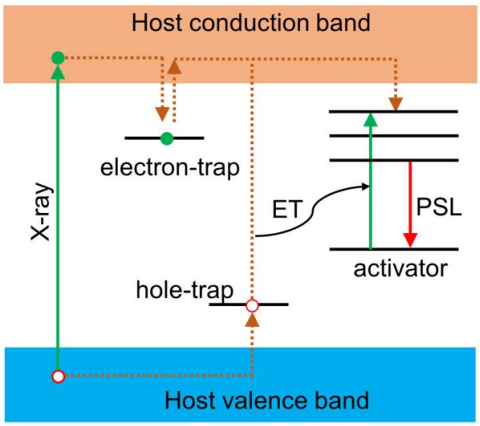

Figure 2.2: Schematic diagram of luminescent material that display photostimulated luminescence (PSL).

2.1.3 Upconversion luminescence

Upconversion is an optical process where two or more near-infrared photons are absorbed by several intermediate energy states of a material [41, 46–49]. Importantly, the emitted luminescence of an upconversion material is shorter in wavelength compared to that of the absorbed light. Efficient generation of upconversion luminescence is typically based on excitation energy transfer from a sensitizer to an activator. A sensitizer is a strong absorbing ion that transfers the energy to the activator [50]. To generate efficient upconversion luminescence, finding a suitable sensitizer-activator pair is important. In addition, the energy transfer from the sensitizer to the activator is possible when the near-infrared excitation energy is absorbed by the sensitizer whereas the activator exhibits no absorption at that wavelength. In addition to the energy transfer based upconversion (ETU) mechanism, upconversion can also be induced by the excited-state absorption (ESA) and photon avalanche (PA) mechanisms as is illustrated in Figure 2.3 for a three-level system [50, 51].

In the case of excited-state absorption (ESA), an ion is excited from the ground G to the excited state E_1 ($G \rightarrow E_1$) by the absorption of a photon, and then a second photon promotes

the excited ion from state E_1 to higher-lying excited state E_2 , yielding upconversion emission from E_2 ($E_2 \rightarrow G$).

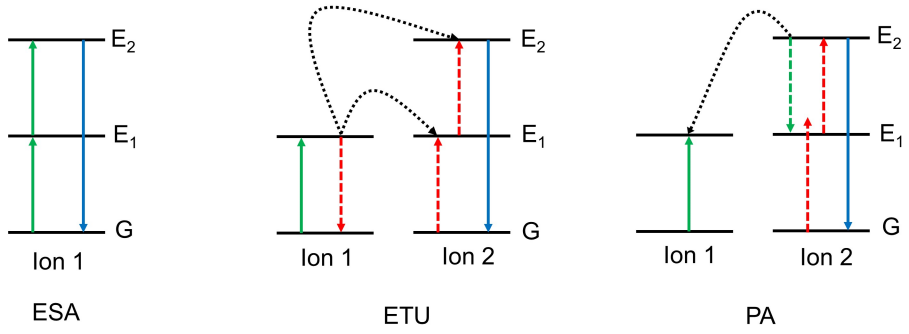

Figure 2.3: Upconversion by the excited-state absorption (ESA), energy transfer (ETU) and photon avalanche (PA) mechanisms (reprinted from ref. [50]).

Similar to ESA, the energy transfer upconversion (ETU) process also utilizes two photons, however it involves two ions. Specifically, two neighboring ions (ion 1 and 2) absorb a pump photon of equal energy and populate metastable states E_1. Subsequently one of the ions (ion 2) is promoted to the upper emitting state E_2 while other ion (ion 1) loses its excitation energy and is back to the ground state G. This energy transfer mechanism results in upconversion emission ($E_2 \rightarrow G$) and in this case ion 1 and ion 2 act as sensitizer and activator, respectively. An efficient generation of upconversion luminescence strongly depends on the distance (R) between the sensitizer and the activator ions as the energy transfer process is strongly dependent on R. For example, the transfer probability for dipole-dipole interaction is inversely proportional to the sixth power of the interionic distance (R^{-6}).

The photon avalanche (PA) upconversion mechanism is a more complicated process and was discovered by Chivian and co-workers [52] in a Pr^{3+} based quantum counter. It mostly depends on the pump power and requires a pump intensity above a certain threshold value. The PA process starts by populating the excited metastable state E_1 level by ground state absorption (GSA) from G to E_1. After the metastable state population, cross-relaxation energy transfer occurs between the excited ion and a neighboring ground state ion. Therefore, both ions occupy the intermediate state E_1 and start to populate the visible-light-emitting level E_2 to initiate further cross-relaxation. The population of E_2 level exponentially increases by the

resonant excited-state absorption (ESA) process and results in upconversion luminescence by the PA process [50].

2.2 Rare-earth ions as activators

Recently, rare-earth ions (lanthanides) have received significant attention as activators in storage phosphors because of their relative insensitivity to the crystalline environment which results in intense and sharp optical transitions [53, 54]. In the periodic table, the lanthanides (Ln) comprise a series of 15 elements between La (Lanthanum) and Lu (Lutetium) [55] as illustrated in Figure 2.4 (red marked). These elements are known as rare-earth elements (RE) since they were initially found in small quantities in oxide ores.

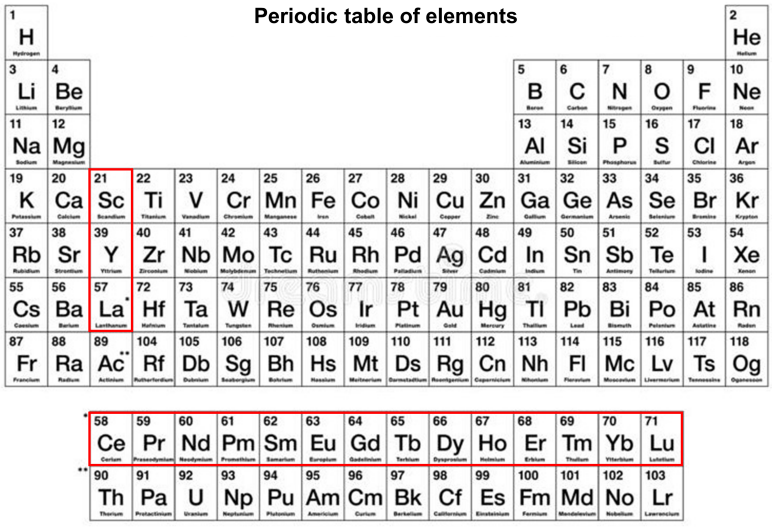

Figure 2.4: Rare-earth elements in periodic table (marked by red boxes). Note that Sc and Y are considered as rare-earth elements because they display similar chemical properties to the rare-earth elements due to the similar size and trivalent oxidation state.

The most common oxidation state for the rare earth ions is 3+ (trivalent) [56]. The trivalent rare-earth have partially filled 4f shells with the electronic configuration $4f^n 5s^2 5p^6$ where n = 0 to 14 [57, 58]. The inner filled 5s and 5p shells play a vital role to shield the 4f electrons from perturbation caused by the surrounding environment (host) [59]. The rare-earth elements are distinguished by their ionic radius which decreases with increasing atomic number as shown in

Table 2.1. This is known as 'lanthanide contraction' which is due to the increase of nuclear charge even though the f-electrons are shielded from the environment.

Generally, rare-earth elements do not only occur in the trivalent oxidation state but can also be stable in the divalent state if they are incorporated in certain hosts. As shown in **Table 2.1**, compared to other rare-earth ions Eu^{3+}/Eu^{2+}, Yb^{3+}/Yb^{2+} and Sm^{3+}/Sm^{2+} have the highest standard reduction potentials, -0.35 V, -1.04 V and -1.57 V, respectively [60, 61].

Table 2.1: Summary of the atomic number, electronic configuration, ionic radius, and standard reduction potential of trivalent rare-earth ions.

Rare-earth element (RE^{3+})	**Atomic number** (Z)	**Electronic configuration of RE^{3+}**	**Ionic radius of RE^{3+}** (pm)	**Standard reduction potential** $RE^{3+} + e^- \rightarrow RE^{2+}$ (V)
La (Lanthanum)	57	$4f^0 5s^2 5p^6$	116.0	-3.74
Ce (Cerium)	58	$4f^1 5s^2 5p^6$	114.3	-3.76
Pr (Praseodymium)	59	$4f^2 5s^2 5p^6$	112.6	-3.03
Nd (Neodymium)	60	$4f^3 5s^2 5p^6$	110.9	-2.62
Pm (Promethium)	61	$4f^4 5s^2 5p^6$	109.3	-2.67
Sm (Samarium)	62	$4f^5 5s^2 5p^6$	107.9	-1.57
Eu (Europium)	63	$4f^6 5s^2 5p^6$	106.6	-0.35
Gd (Gadolinium)	64	$4f^7 5s^2 5p^6$	105.3	-3.82
Tb (Terbium)	65	$4f^8 5s^2 5p^6$	104.0	-3.47
Dy (Dysprosium)	66	$4f^9 5s^2 5p^6$	102.7	-2.42
Ho (Holmium)	67	$4f^{10} 5s^2 5p^6$	101.5	-2.80
Er (Erbium)	68	$4f^{11} 5s^2 5p^6$	100.4	-2.96
Tm (Thulium)	69	$4f^{12} 5s^2 5p^6$	99.4	-2.27
Yb (Ytterbium)	70	$4f^{13} 5s^2 5p^6$	98.5	-1.04
Lu (Lutetium)	71	$4f^{14} 5s^2 5p^6$	97.7	——

2.2.1 Spectroscopy of rare-earth ions

As discussed above, rare earth ions have a partially filled 4f shell and due to the shielding by 5s and 5p electrons, the 4f electrons exhibit minimal interaction with the host lattice and show only a slight dependence on the surrounding. This leads to dominant and narrow zero-phonon line emissions (f $\rightarrow$ f transitions) which have attracted spectroscopists for a long time [62]. For a free rare-earth ion, electric dipole transitions between the 4f levels are parity forbidden.

However, in a crystal, electric dipole transitions can occur on non-centrosymmetric sites whilst centrosymmetric sites can show magnetic dipole allowed transitions. In addition, vibrational coupling may induce transition intensity. In highly symmetric crystals where electric dipole transitions are forbidden, an admixture of opposite parity or presence of any defects can break the symmetry rule by partially inducing electric dipole transition intensity. The spectroscopy of trivalent rare-earth has been nicely summarized by Dieke [63] a while ago, and his famous diagram is illustrated in Figure 2.5.

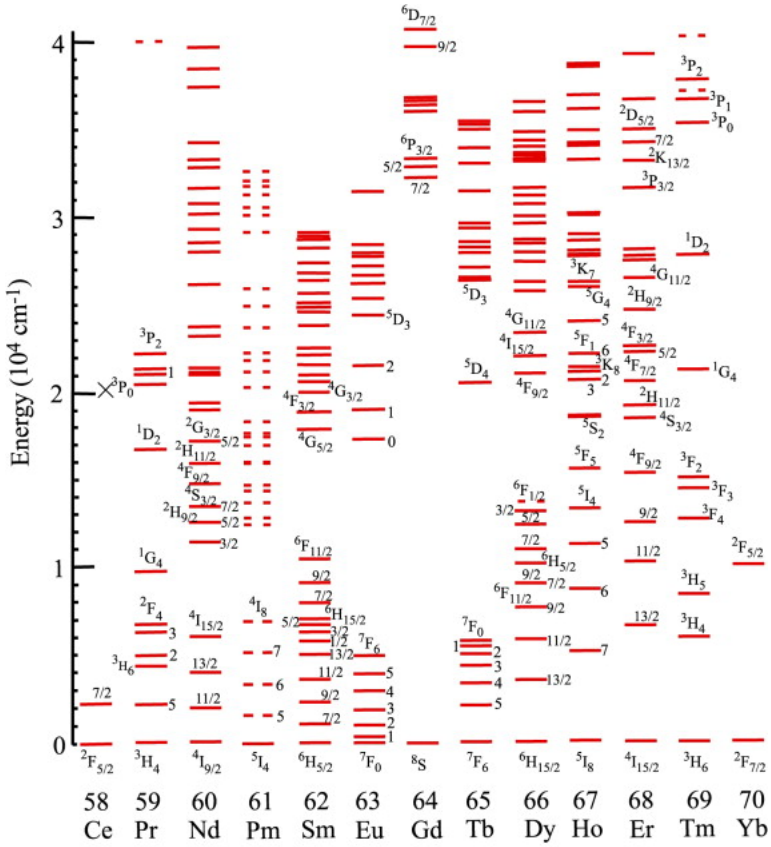

Figure 2.5: Energy level diagram of trivalent rare-earth elements (RE^{3+}) in LaF_3:RE^{3+} crystal (reprinted with permission from ref. [63]).

Partial energy level diagrams of specific rare-earth ions (which are investigated in this thesis) are presented in Figure 2.6.

Among the rare-earth elements, divalent Eu^{2+}, Sm^{2+} and Yb^{2+} can be readily observed in crystals due to their broad 4f $\rightarrow$ 5d absorption band and narrow $4f^n \rightarrow 4f^n$ emission [60, 64–70].

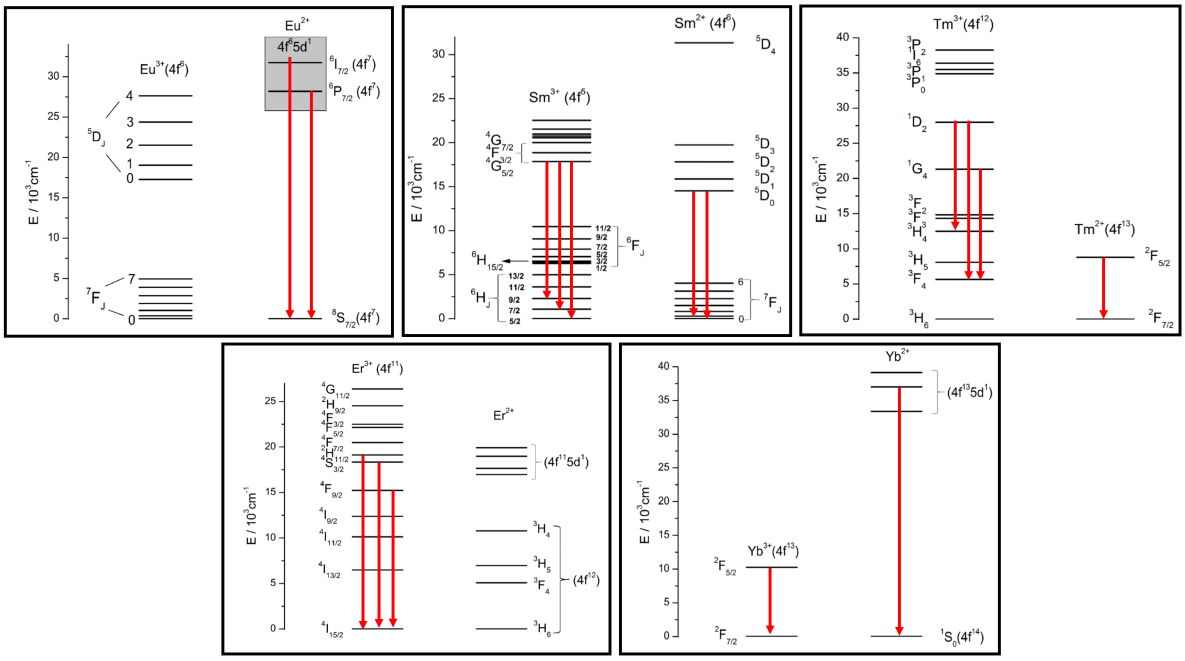

Figure 2.6: Partial energy level diagrams of Eu, Sm, Tm, Er and Yb in their 3+ and 2+ oxidation states. The observed transitions are indicated by red arrows (reprinted with permission from ref. [63]).

In addition, rare-earth ions exhibit distinct luminescence properties which allow the investigation of a system within a broad optical range spanning from the UV to the infrared (380-1800 nm), facilitating photostimulated, photoluminescence and upconversion luminescence light.

2.3 $BaLiF_3$ as a host matrix

To explore new luminescent systems for their application as phosphors, investigations of the interaction between the optically active ions and the host lattice is crucial. The following section includes a brief description of $BaLiF_3$ as a potential host matrix for rare earth ions along with the preparation process, optical properties, and X-ray storage capability.

$BaLiF_3$ crystallizes in a cubic phase with space group Pm-3m (O_h^1) [71, 72]. It is a member of the fluoroperovskite family with the general formula ABF_3 (A = Li, Na, K, Rb, Cs and B = Be, Mg, Ca, Sr, Ba) where $BaLiF_3$ is the only compound with a low Goldschmidt tolerance factor (t) ~0.596 which is even out of the range for distorted perovskites. The Goldschmidt tolerance factor has been extensively used to predict the stability of the perovskite structure

(ABF_3) by using the Equation 2.1 [73, 74]

$$t = \frac{r_A + r_F}{\sqrt{2}(r_B + r_F)} \tag{2.1}$$

where r_A, r_B and r_F are ionic radii of A, B and F (Figure 2.7a). For normal perovskites this factor (t) is ~0.995 [72]. When t is lower than 0.75, the structure tends to deviate from the ideal perovskite structure so that the bonding strain is reduced [75, 76]. The low tolerance factor results in $BaLiF_3$ adopting an inverse perovskite structure, and unlike classic perovskites, the cation with the higher charge (Ba^{2+}) occupies the position of the higher coordination number in the lattice. Particularly, the $BaLiF_3$ structure comprises fluoride (F^-) octahedra around the lithium (Li^+) and cuboctahedra around the barium (Ba^{2+}) ions, where they are coordinated in a fashion of two compressed square pyramids [72]. The Wyckoff position for the Ba, Li and F atoms are (0, 0, 0), ($\frac{1}{2}$, $\frac{1}{2}$, $\frac{1}{2}$) and (0, $\frac{1}{2}$, $\frac{1}{2}$) respectively. Despite the inverse perovskite phase, the crystal symmetry of $BaLiF_3$ remains the same as that of normal perovskites (O_h^1). However, the inverse arrangement results in different crystal field interactions. Figure 2.7 displays the unit cell structure of a classic perovskite ABF_3 (Figure 2.7 a) and the inverse perovskite structure of $BaLiF_3$ (Figure 2.7 b).

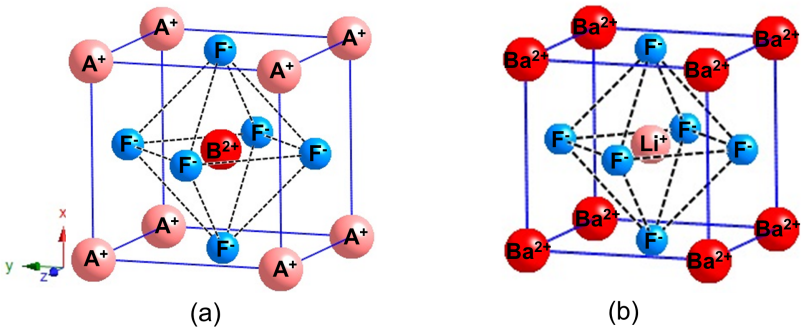

Figure 2.7: Unit cell structure of (a) a classic perovskite (ABF_3) and (b) the inverse perovskite $BaLiF_3$.

2.3.1 Preparation of $BaLiF_3$

It is well documented that the synthesis method plays an important role on the properties of a functional material. For example, nanocrystalline materials can show good ionic conductivity and luminescent properties compared to their microcrystalline counterparts [77, 78]. $BaLiF_3$ can be prepared by following mechanochemical and conventional high temperature synthesis routes.

2.3.2 Single crystal growth

Single crystal growth is an important technique that has been widely used for many decades for realizing electronic and optoelectronic materials [30, 79]. Crystals can be grown by utilizing a variety of techniques such as from melt, solution, hydrothermal and gel. Among them, crystal growth via melt is the most widely used technique comprising Bridgman-Stockbarger, Kyropoulos, Czochralski, and Verneuil (flame fusion) methods. Amongst these different melt-based methods, Czochralski is the most used commercial technique [80] to grow high purity large-size single crystals, which is almost impossible to obtain by any other existing methods. Importantly, the melt temperature remains constant throughout the process [81]. Thus, it provides a virtually constant growth rate for the crystal.

Bensalah et al., [79] utilized a vacuum tight Czochralski system equipped with a high-purity graphite heater and an automatic diameter control system to grow pure $BaLiF_3$ crystals. The crystal was grown from the melt of a non-stoichiometric mixture of 43% BaF_2 (Rare Matels Co., Ltd., purity 99.99%) and 57% LiF (Rare Matels Co., Ltd., purity 99.99%) in a platinum crucible of 60 mm in diameter. A <100> direction oriented $BaLiF_3$ seed was used to control the growth of the crystal in the <100> direction at a pulling rate of 1 mm/h and a rotation rate of 10 rpm. The growth chamber was evacuated to $\sim 10^{-3}$ Pa and the system was heated from room temperature to 550 °C for 12 h to eliminate the water and oxygen from the chamber and starting materials. Then the compounds were melted and treated under a high purity CF_4 gas flow for 5-6 h. Finally, the crystal (20 mm in diameter and 80 mm in length) was cooled to room temperature at a rate of 30 °C/h.

Similarly, *Baldochi et al.*, used the Czochralski method to prepare pure $BaLiF_3$ crystals from

the melt of BaF_2 (43%) and LiF (57%) in a carbon crucible at 700 °C under a flow of CF_4 [82]. Furthermore, Wiedemann et al., [72] obtained a transparent and colour less $BaLiF_3$ crystal (18 mm diameter and 75 mm long) in a HF environment by following the former route [82]. It is well documented that non-stoichiometric molar ratio such as 44% BaF_2 and 56% LiF needs to be used to grow high quality $BaLiF_3$ crystal [35] as $BaLiF_3$ melts incongruently and must be grown from a melt of excess LiF to avoid other phase formation.

2.3.3 High temperature sintering

High temperature sintering is a conventional solid-state synthesis process where raw materials are sintered with or without applying external pressure at a high temperature [83, 84]. In this process some or all properties of the system change due to the reduction of free enthalpy [85]. *Bron* reported that in oxide mixtures sintering causes excess lattice disorder due to an extension of the lattice which results in bond loosening [83]. On the other hand, sintering of organic materials is impossible because of their extremely small self-diffusion coefficients. *Oel* reported that crystallite size plays an important role during the sintering process since it influences the effectiveness of grain boundaries as sinks for vacancies [86]. Furthermore, the powder from single-crystal particles exhibits slight grain growth at high sintering temperatures, while polycrystalline particles show a strong grain growth because of their higher activity [86]. It was also found that a sintering atmosphere has an extremely important influence e.g., inert or reducing gases can cause fundamental differences during the process.

Duvel et al., [77] reported a high temperature synthesis route for $BaLiF_3$. In brief, an equimolar mixture of BaF_2 and LiF was fired at 750 °C for 5 h under a reducing nitrogen atmosphere, yielding polycrystalline $BaLiF_3$.

2.3.4 Ball milling

Mechanochemistry refers to the chemical synthesis by grinding two or more chemical compounds with no or minimal solvent [87–93]. One of the mechanochemical methods, high energy ball milling, is a versatile synthesis process for the preparation of fine nanocrystalline powder. It is a non-manual method where mechanical action of milling balls introduces a strong collision force in the ball milling jar to break the reagents into fine powder with smaller particle

size. The advantage of using mechanical synthesis over conventional chemical routes is to avoid multi-phase formation and any evaporation of light elements. Therefore, mechanochemically obtained products are relatively pure, stoichiometric and anhydrous [77].

Historically, the ball milling method was widely used to prepare metal alloys and inorganic oxides, and also metal halides including fluoride perovskite-type compounds. For example, in 1820 *Michael Faraday* conducted the mechanochemical transformation of AgCl → Ag in the presence of Zn, Cu and Sn/Fe, by grinding them by a pestle and mortar [94]. Mechanochemical transformations were first conducted to synthesize alloys by ball milling the raw materials (powder) for a relatively long time under an inert gas atmosphere to prevent oxidation [87]. In some cases, reducing agent such as methanol and benzene was used to control the synthesis atmosphere. A brief description of the mechanical synthesis of a few selected alloys is presented in **Table 2.2**.

Table 2.2: Mechanochemical preparation of inorganic alloys.

Alloys	**Starting materials**	**Synthesis atmosphere**	**Ball milling time**	**Equipment**
$Ni_{75}Nb_{12}B_{13}$ [95]	Ni (powder, 70-100 mkm) + Nb (powder, 100 mkm) + B (amorphous)	Argon	2-8 hours	Water-cooled planetary ball mill (MAPF-2M)
Ti-Al-B [96]	Ti (electrolytic powder) + Al (sprayed powder) + B (amorphous powder)	Benzene (agent)	12 hours	Planetary ball mill
Cu-Co [84]	Co (powder, 20 μm) + Cu (powder, $<$ 75 μm)	Methanol (agent)	100 hours (120 rpm)	Planetary ball mill (Pulverisette)
$Fe_{80}Mo_{20}$ and $Fe_{50}Mo_{50}$ [97]	Fe (powder, 40 μm) + Mo (powder, 20 μm)	Argon	1-80 hours (250 rpm)	Planetary ball mill (Fritsch Pulverisette P5)
$Fe_{0.45}Mn_{0.25}Al_{0.3}$ [98]	Fe (powder) + Mn (powder) + Al (powder)	Air	4 -24 hours (280 rpm)	Planetary ball mill (Pulverisette P5)

In contrast to alloys, the mechanochemical preparation of inorganic oxides from their metal

oxide powder can be carried out in air because all the materials are already oxidized. Additionally, oxide materials with nano-size can be produced by a shorter period of ball milling such as 8-24 h. Some examples of metal oxides synthesis by ball milling are given in **Table 2.3**.

Table 2.3: Mechanochemical preparation of inorganic oxide

Oxide compounds	**Synthesis route**	**Synthesis atmosphere**	**Ball milling time**	**Equipment**
$CrVO_4$ [99]	$Cr(OH)_3{\cdot}nH_2O + V_2O_5 \rightarrow 2CrVO_4 + nH_2O$	air	15-240 min (700 rpm)	Planetary ball mill (Pulverisette-7)
$LaVO_4$ [100]	$La_2O_3 + V_2O_5 \rightarrow 2LaVO_4$	air	15-240 min (700 rpm)	Planetary ball mill (Pulverisette-7)
$LaCrO_3$ [101]	$La_2O_3 + Cr_2O_3.nH_2O \rightarrow 2LaCrO_3 + nH_2O$	air	15-240 min (700 rpm)	Planetary ball mill (Pulverisette-7)
$PbTiO_3$ [102]	$PbO + TiO_2 \rightarrow PbTiO_3$	air	50 hours	SPEX 8000 Mixer Mill
$ZnFe_2O_4$ [103]	$ZnO + \alpha\text{-}Fe_2O_3 \rightarrow ZnFe_2O_4$	air	24 hours	Planetary ball mill (Pulverisette-4)
$NiFe_2O_4$ (23 nm) [104]	$NiO + \alpha\text{-}Fe_2O_3 \rightarrow NiFe_2O_4$	air	8 hours (600 rpm)	Planetary ball mill (KM-10)

In some cases, a direct mechanochemical combination of oxides cannot produce a homogenous phase, and solid-state sintering needs to be employed. However, the mechanical activation reduces the formation temperature. For example, $CaZrO_3$ can be prepared by sintering ZrO_2 and CaO at 1100 °C, but 20 hours ball milling before this process reduces the sintering temperature of $CaZrO_3$ from 1100 °C to 800 °C [105]. Similar behaviour was observed for $ZrTiO_4$ [106], $MgTa_2O_6$ [107] and $Bi_4Sr_{n-3}Ti_nO_{3n+3}$ (n = 4, 5) [108]. Also, the presence of a reducing metal and use of an inert gas can significantly reduce the ball milling time, such as Ti in the formation of $FeTiO_3$ [109], Fe in Fe_2GeO_4 [110] and Zn in $ZnFe_2O_4$ [111].

Fluoride perovskite-type compounds with the general formula ABF_3 including $NaSn_2F_5$ [112], $RbPbF_3$ [113], $Pb_{1-x}Sn_xF_2$ [114] have been prepared by mechanochemical synthesis route for the applications in fast ion conductors. Similarly, nanoscale particles of $KMCl_3$ (M = Ti, Cr, Mn, Fe, Co, Ni, Cu, Zn) and KMF_3 (M = Mg, Zn, Mn, Ni, Cu and Co) have been prepared

by the same preparation route as shown in **Table 2.4**.

Table 2.4: Mechanochemical preparation of halide perovskite

Halide compounds	Synthesis route	Synthesis atmosphere	Ball milling time	Equipment
$KMCl_3$ (M = Ti, Cr, Mn, Fe, Co, Ni, Cu, Zn) [115]	$NaF + MF_2 \rightarrow NaMF_3$	Argon	60-130 min (750 rpm)	Planetary ball mill (Pulverisette-7)
KMF_3 (M = Mg, Zn, Mn, Ni, Cu and Co) (20 nm) [116, 117]	$KCl + MCl_2 \rightarrow KMF_3$	Air	20 min	SPEX 8000 Mixer Mill

Nanocrystalline $BaLiF_3$ has been prepared by ball milling an equimolar mixture of BaF_2 and LiF for 3 h [77]. Similarly, alloyed $Ba_{1-x}Sr_xLiF_3$ [118] has been synthesized by using BaF_2, SrF_2 and LiF as starting materials. However, the mixed phase is highly sensitive to heat treatment and due to this fact long time milling at high energy resulted in a Sr free $BaLiF_3$ phase when the x value and the milling time were > 0.4 and 3 h, respectively.

2.4 Phosphors: Current state of the art and future development

2.4.1 Rare-earth doped alkaline earth fluorohalides

BaFBr(I):Eu^{2+}: To date, alkaline earth fluorohalides MFX (M = Ca, Sr, Ba; X = Cl, Br, I) in particular BaFBr(I) doped with divalent Eu^{2+} have found widespread applications as commercial X-ray storage phosphors and BaFBr(I):Eu^{2+} is widely used in computed radiography [13, 18, 119, 120]. In particular, the imaging technology based around this phosphor is the modality of choice for intraoral dental X-ray examinations [2, 16, 121]. Typically, X-irradiation induces F-centre as electron traps; two possible F-centre in BaFBr are F(Br^-) and F(F^-) where electrons are trapped at Br^- and F^- vacancy sites [13, 18, 25, 122, 123]. Upon red laser excitation, the electrons recombine with the holes and transfer the recombination energy to Eu^{2+}. This process yields broad $4f^65d \rightarrow 4f^7$, Eu^{2+} emission at ~390 nm i.e., anti-

Stokes emission. Despite the significant developments established for the improvement of this phosphor, they still suffer from some drawbacks such as erasure of stored information due to the spontaneous or thermally activated electron hole recombination by photostimulation light and limited signal to noise ratio [8, 20, 124].

To bridge these gaps there has been a tremendous revival of interest in exploring new luminescent materials with high X-ray sensitivity which is crucial for preventive health-care examinations. More explicitly, much of the focus of storage phosphor-based research is on developing a new phosphor material that can potentially exceed the sensitivity of BaFBr(I):Eu^{2+}, allowing a reduction of applied dose.

BaFCl:Sm^{2+}: Studies have shown that, alkaline-earth fluorohalides based phosphors [125–129] such as BaFCl doped with Sm^{3+} shows significant photoluminescence properties [130, 131] and the rare feature of room temperature hole-burning [132]. As a result, in the context of dosimetry and computed radiography this system has been investigated extensively over the last few years as a photoluminescent X-ray storage phosphor [26, 78, 133]. Significantly, it was observed that the BaFCl:Sm^{3+} phosphor with an average crystallite size of ∼200 nm exhibits ∼500,000 times higher X-ray sensitivity in comparison with the microcrystalline phosphor [134]. The storage mechanism is based on the reduction of Sm^{3+} ions to Sm^{2+} upon exposure to ionizing radiation. The X-ray induced Sm^{2+} ions in BaFCl can be efficiently excited by the parity allowed $4f^6 \rightarrow 4f^5 5d$ transition at ∼420 nm and read-out as photoluminescence by $^5D_J \rightarrow {}^7F_J$ f-f transitions. It was also demonstrated that the reduction of $Sm^{3+} \rightarrow Sm^{2+}$ in BaFCl occurs upon UV-irradiation due to the presence of oxide impurities such as $O^{2-}/(O_2)^{2-}$ [124]. The UV storage phenomena of BaFCl:Sm^{3+} has potential application in rewritable multilevel optical data storage devices. In addition, admixture of halides in BaFCl:Sm^{3+} ($BaFBr_{0.9}Cl_{0.1}$:Sm^{3+}, $Ba_{0.6}Sr_{0.4}FCl$:Sm^{3+}, $Ba_{0.1}Sr_{0.9}FCl$:Sm^{3+}, $Sr_{0.8}Ca_{0.2}FCl$:Sm^{3+}) allows engineering of Sm^{2+} inhomogeneous linewidth [135] to perform the room-temperature hole-burning spectroscopy which is crucial for optical data storage applications [136–138]. In addition, BaFCl doped with a wide range of rare-earth element including Eu and Tm was also investigated for practical implementations [139–142].

2.4.2 Storage capability of Alkali halides and Elpasolites

The X-ray storage ability of alkali halides crystals has been also investigated and it was found that CsBr:Eu^{2+}, RbBr:Ga^{+} and CsBr:Ga^{+} are the best candidates for photostimulable storage phosphor application [6, 13, 31].

Eu^{2+} doped CsBr exhibits fast read-out times, low stimulation energy and high conversion efficiency for photostimulated luminescence [143]. In this case, the incident X-ray creates electron-hole pairs, and the electrons are trapped in anion vacancies (F-centre) of the host lattice CsBr but the hole trapping mechanism still remains subject of investigations. According to EPR measurement by *Loncke et al.*, [144] the holes are trapped as V_K centre in the neighboring Eu^{2+} located at Cs^{+} sites by resulting in the formation of Eu^{2+}-V_K centres. During photostimulation (λ = 680 nm) the electrons are liberated from the F-centre into their non-relaxed excited state. Subsequently, each electron is either thermally excited to the conduction band with a subsequent capture of a Eu^{2+}-V_K centre or can tunnel directly to a neighboring Eu^{2+}-V_K site. The electron recombines with the V_K centre and transfers the recombination energy to the adjacent Eu^{2+} ion. This process leads to the 4f-5d excitation and subsequent relaxation which results in photostimulated emission at 440 nm [145, 146].

The storage mechanism of RbBr:Ga^{+} [147] and CsBr:Ga^{+} [148] is quite simple, where X-irradiation simultaneously produces electron traps (F-centres) and Ga^{+} ions act as holes trap centre, resulting in Ga^{2+}. Importantly, two types of Ga^{2+} centres (type-I and type-II) were observed; type-I stay isolated on a Rb^{+}/Cs^{+} site which takes part in the photostimulation process, and type-II Ga^{2+} centre creates a complex between Ga^{2+} on Rb^{+}/Cs^{+} sites and nearest cation vacancy.

In addition, elpasolites such as Cs_2NaYF_6:Ce^{3+} [149] also shows promising phenomena for practical implementation [13]. In this case, the storage mechanism is based on the pairing of F-centres and activators (Ce^{3+}) where the F-centres are generated upon exposure to X-ray radiation and the activator ions Ce^{3+} act as a hole trap.

2.4.3 Luminescence properties of undoped and doped $BaLiF_3$

$BaLiF_3$ activated with rare-earth ions: Spectroscopy of divalent rare earth ions/transition metals in inverse perovskite $BaLiF_3$ has been the subject of a few studies and this section provides a review on the experimental works reported in the literature to study the luminescence properties of rare-earth elements (RE) in centrosymmetric $BaLiF_3$, as these are relevant to this thesis [150–152].

Generally, rare-earth ions occupy the centrosymmetric Ba^{2+} site where only magnetic dipole and vibrationally induced electric dipole transitions are allowed. In this regard the most studied materials are $BaLiF_3$:Eu^{2+} and $BaLiF_3$:Sm^{2+}. *Meijerink* observed the divalent Eu^{2+} transition $^6P_{7/2} \rightarrow {}^8S_{7/2}$ upon $^8S_{7/2} \rightarrow 4f^65d$ excitation in a macroscopic $BaLiF_3$:Eu^{2+} crystal [153]. Additionally, it was demonstrated that in $BaLiF_3$:Eu^{2+}, vibronic transition probabilities are 100 times larger in comparison with $BaLiF_3$:Gd^{3+} which is due to the small energy separation (1000 cm^{-1}) of Eu^{2+} $4f^7$ states and the opposite parity state $4f^65d$. In a subsequent paper, *Meijerink* along with *Dirksen* reported that this difference is ∼five times larger in $BaLiF_3$:Sm^{2+}. As a result, the admixture of Sm^{2+} $4f^65d$ state is considerably less in $BaLiF_3$:Sm^{2+} [151]. Based on these experimental demonstrations, it was concluded that $BaLiF_3$:Eu^{2+} is an ideal system for the observation of vibronic transitions.

The possibility of $BaLiF_3$:Eu^{2+} and $BaLiF_3$:Sm^{2+} as phosphor materials were explored by *Gros et al.*, and *Xia et al.*, [150, 152] respectively. *Quang et al.*, reported the upconverted luminescence of Ho^{3+} from $^5F_3$, $^5S_2/{}^5F_4$, $^5F_5$ states in microcrystalline $BaLiF_3$:Yb^{3+}, Ho^{3+} under near-infrared excitation. Here the upconversion mechanism was followed by the ground-state absorption (GSA) along with Yb^{3+} assisted energy transfer. Similar anti-stoke luminescence was also detected for Er^{3+} ion in Yb^{3+} and Er^{3+} co-doped $BaLiF_3$.

Additionally, trivalent Ce^{3+} and Tb^{3+} doped $BaLiF_3$ were synthesized by a hydrothermal process at 200 °C where Ce^{3+} and Tb^{3+} ions replaced the Ba^{2+} ions. Interestingly an efficient energy transfer from Ce^{3+} to Tb^{3+} was observed in Ce^{3+} and Tb^{3+} co-doped $BaLiF_3$. It was expected that this system can be utilized as a green photoluminescent phosphor in tricolour lamps [154].

$BaLiF_3$ activated with transition metals: Transition metal doped $BaLiF_3$, including

$BaLiF_3$:Ni^{2+} and $BaLiF_3$:Co^{2+} were also investigated [35, 155, 156]. In these cases, divalent Ni^{2+} and Co^{2+} dominantly entered the lattice in the octahedral position of Li^+ in $BaLiF_3$ crystals due to their similar ionic radii. In addition to storage phosphors, these systems can be also utilized for laser applications. **Table 2.5** provides a summary of the spectroscopy of $BaLiF_3$ activated with rare-earth ions and transition metal ions respectively.

Table 2.5: A brief summary of the spectroscopy of activated $BaLiF_3$.

Phosphor	**Activator site in $BaLiF_3$**	**Type of emission**	**Excitation wavelength**	**Emission wavelength**
$BaLiF_3$:Eu^{2+} [152]	Centrosymmetric (Ba^{2+})	Photoluminescence	230-275 nm 275-335 nm	Eu^{2+} 359.1 nm (359 nm, 359.006 nm, 359.060 nm)
$BaLiF_3$:Sm^{2+} [151]	Centrosymmetric (Ba^{2+})	Photoluminescence	240-500 nm	Sm^{2+} 693.8 nm
$BaLiF_3$:Yb^{3+}, Ho^{3+} [36]	Centrosymmetric (Ba^{2+})	Upconversion luminescence	980 nm	Ho^{3+} 485 nm, 543 nm, 653 nm, 750 nm
$BaLiF_3$:Yb^{3+}, Er^{3+}	Centrosymmetric (Ba^{2+})	Upconversion luminescence	980 nm	Er^{3+} 522 nm, 541 nm, 676 nm
$BaLiF_3$:Ce^{3+} [37]	Centrosymmetric (Ba^{2+})	Photoluminescence	265 nm/299 nm	Ce^{3+} 367 nm
$BaLiF_3$:Tb^{3+} [154]	Centrosymmetric (Ba^{2+})	Photoluminescence	217 nm	Tb^{3+} 544 nm
$BaLiF_3$:Ni^{2+} [35]	Octahedral (Li^+)	Photoluminescence	390 nm, 700 nm, 1180 nm	Ni^{2+} 480 nm, 740 nm, 1500 nm
$BaLiF_3$:Co^{2+} [35]	Octahedral (Li^+)	Photoluminescence	500 nm, 1210 nm	Co^{2+} 1588 nm

Considering the above discussions, it is noteworthy that the storage mechanism of $BaLiF_3$ doped with a wide range of rare-earth elements is less explored, and further systematic studies are clearly required to advance the understanding. In this regard, it would be interesting to explore the radiation storage capability of nanocrystalline $BaLiF_3$ when activated with a wide

range of rare-earth ions, including Eu, Sm, Tm, Er and Yb.

Undoped/Pure $BaLiF_3$: Luminescence of undoped $BaLiF_3$ is dominated by colour centres/F-centre aggregates which are a ubiquitous feature of ionic crystals, in particular halides, and generally consist of electrons trapped at sites of missing anions. They have a characteristically broad and strong optical transition band, with a large Stokes shift and they have been applied as tunable solid-state lasers [31]. Their prominent luminescence phenomena can be utilized in the development of optical data storage and radiation dosimeters [157]. In addition, colour centres often display a narrow and pure electronic zero-phonon line at low temperature with potential applications in quantum information processing and optical sensing. The formation of intrinsic colour centres such as F-centre aggregates mostly depends on the mobility of defects within the crystal lattice. In crystals, defects can be produced by slightly changing the stoichiometry and upon exposure to radiation. The first colour centre based laser action was observed in an alkali halide crystal ($KCl:Li^+$) at a wavelength of 2.7 μm [158]. Subsequently, this system was used as tunable laser source in the spectral range 2.6-2.8 μm [159] which paved the way for application in tunable continuous wave colour centre lasers.

So far, several colour centres have been demonstrated in pure $BaLiF_3$ upon irradiation. For example, a $BaLiF_3$ crystal grown by the Czochralski method in the <100> and <111> directions exhibited five absorption bands at 260 nm, 386 nm, 420 nm, 480 nm, and 632 nm upon electron irradiation. By comparing $BaLiF_3$ with LiF [160] and $KMgF_3$ [161–163] crystals, these bands were assigned to F, F_3, F_2, F_3^+ and F_2^+ centres, respectively [164]. Surprisingly, the F_2^+ band at 630 nm was detected only in the crystal grown in the <100> direction [164]. It was also observed that F-aggregate defects in $BaLiF_3$ crystal were quite stable in the <100> compared to that in the <111> direction. This might be due to the crystalline quality which depends on the number of crystalline domains formed during the growth process [165]. X-ray irradiated $BaLiF_3$ crystals were studied by *Tale et al.*, who observed a hole centre and F-type defects absorption at 420 nm and 470-770 nm respectively [166]. *Bensalah et al.*, demonstrated the potential of $BaLiF_3$ (grown in the <100> direction) crystals for application in laser-based visible ultraviolet projection lithography [79]. **Table 2.6** summarizes the spectral properties of colour centres observed in fluoride crystals.

Table 2.6: Summary of spectral properties of colour centres in fluoride crystals including LiF, $KMgF_3$ and $BaLiF_3$.

Colour centre	**System**					
	LiF		**$KMgF_3$**		**$BaLiF_3$**	
	Absorption	**Emission**	**Absorption**	**Emission**	**Absorption**	**Emission**
	/nm	/nm	/nm	/nm	/nm	/nm
F	250	—	270 [161]	—	260 [164]	—
F_2	445 [160]	670 [160]	445 [161]	566 [162]	420 [160]	—
F_2^+	630 [160]	910	—	—	632 [160]	702 [164]
F_3	380 [167]	—	395 [161]	416 [162]	386 [165]	—
F_3^+	458 [168]	539 [160]	—	—	480 [165]	—

The above studies clearly demonstrated that the formation of F-centre aggregates in $BaLiF_3$ depends on the preparation method, including purity, growth conditions of crystals, and on the post-preparation treatments (e.g., electron irradiation, exposure to ionizing radiation, high temperature annealing etc.). As such, it is expected that high temperature annealing may introduce such defects in mechanochemically prepared $BaLiF_3$ nanocrystals which might be interesting for future laser applications.

2.5 Aim of this thesis

This thesis is focused on the investigation of $BaLiF_3$ as host matrix, and doped with various rare-earth ion as activators, and explore the luminescence properties of these systems. Specifically, the principle aims of this dissertation are as follows:

1. Mechanochemical synthesis of rare earth ion doped $BaLiF_3$

Several studies have reported the preparation of doped and undoped $BaLiF_3$ crystals by high temperature and hydrothermal synthesis routes. One of the main objectives of this thesis is to prepare nanocrystals of rare-earth ions doped $BaLiF_3$ (∼30-40 nm) by utilizing a mechanochemical synthesis route, such as ball milling. The rare-earth elements (RE) will be incorporated into the host lattice in their trivalent oxidation state (RE^{3+}). The reduction of trivalent to divalent state will be carried out by X-irradiation (X-ray radiation).

2. Investigation of Storage capability of the as-prepared phosphors

The X-ray storage capability and mechanism of the as-prepared phosphors will be explored by

investigating their photoluminescence and upconversion luminescence properties. Explicitly, the reduction of trivalent (RE^{3+}) $\rightarrow$ divalent (RE^{2+}) rare-earth ions will be quantified as a function of X-ray dose. The luminescence properties of rare-earth activated $BaLiF_3$ will be investigated in the spectral range from the UV to the near-infrared.

3. Colour centre in undoped $BaLiF_3$

The generation of intrinsic colour centre in undoped $BaLiF_3$ (synthesized by ball milling) will be explored which might be useful for tunable solid-state laser, radiation monitoring system and optical data storage phosphor.

Chapter 3

Experimental details

This chapter contains a brief description of the synthesis methods of doped and undoped $BaLiF_3$ nanocrystals, characterization techniques and spectroscopic analysis of the nanoparticles, including the experimental procedures employed for the studies in the subsequent chapters. The nanocrystalline materials i.e., $BaLiF_3$ doped with Sm^{3+} /Tm^{3+} /Eu^{3+} / (Er^{3+}, Yb^{3+}) and undoped $BaLiF_3$ were prepared utilizing high energy ball milling method. Their structural properties, average crystallite size and chemical states were characterized by powder X-ray diffraction (XRD), transmission and scanning electron microscopy (TEM and SEM), TEM and SEM based energy dispersive X-ray spectroscopy and X-ray photoelectron microscopy (XPS). The optical properties of the nanomaterials were rigorously investigated by photoluminescence and upconversion luminescence spectroscopy.

3.1 Synthesis of rare-earth ions doped $BaLiF_3$

Rare-earth ions (RE) doped $BaLiF_3$ was prepared mechanochemically by ball milling a mixture of BaF_2, LiF and $RECl_3.6H_2O$/REF_3. BaF_2 was prepared by the co-precipitation of $Ba(NO_3)_2$ (May and Baker Australia PTY LTD) and NH_4F (Sigma-Aldrich) solutions according to the following chemical equation,

$$Ba(NO_3)_2 + 2NH_4F \rightarrow BaF_2 \text{ (white precipitate)} + 2NH_4NO_3$$

Two separate aqueous solutions of $Ba(NO_3)_2$ (0.4 $molL^{-1}$) and NH_4F (8 $molL^{-1}$) were pre-

pared and then transferred in a 1000 mL beaker. The mixture was kept at room temperature for half an hour. After that, a white precipitate of nanocrystalline BaF_2 was formed which was separated from the solution by filtration. The resultant white precipitate was washed sequentially by using ethanol, methanol, and Milli-Q water, and further dried in an oven (Labec, Laboratory Equipment Pty. Ltd., Sydney, Model H323) at 50 °C for 24 hours. Finally, the powder was thoroughly ground by a mortar and pestle.

LiF and the RE compounds (see **Table 3.1**) were purchased from commercial suppliers, such as Ajax chemicals and Sigma-Aldrich respectively.

3.1.1 Ball milling method

Nanocrystalline $BaLiF_3:RE^{3+}$ was prepared by mechanochemical synthesis at room temperature utilizing a high energy ball milling method according to the following solid-state reaction [77, 118],

$$BaF_2 + LiF + RE^{3+} \rightarrow \text{nanocrystalline } BaLiF_3:RE^{3+}$$

A Retsch Mixer Mill 200 with a 10 mL zirconia lined jar and two 12 mm diameter (5.5 gm) zirconia balls were used for the ball milling process.

For the studies presented in this thesis, Sm^{3+}, Eu^{3+}, Tm^{3+}, Er^{3+} and Yb^{3+} were used as the optically active ions. These ions were introduced by using specific compounds as listed in **Table 3.1**.

As an example, the preparation of ball-milled $BaLiF_3:Sm^{3+}$ is discussed in the following:
1 mmol BaF_2, 1 mmol LiF and 0.005 mmol $SmCl_3.6H_2O$ were ball milled at a frequency of 20 Hz for 90 min. Then the resultant powder sample was transferred into a petri dish and dried in an oven (Labec, Model H323) at a temperature around 50 °C for 1 hour. Subsequently, the ball milling process was continued for another 90 min at 20 Hz.

Very similar preparation methods were used for the synthesis of nanocrystalline $BaLiF_3:Eu^{3+}$,

$BaLiF_3$:Tm^{3+}, $BaLiF_3$:Er^{3+}, Yb^{3+} and nominally undoped $BaLiF_3$ [36, 140, 169]. Details of the preparation conditions are given in **Table 3.1**.

Table 3.1: Preparation methods of nanomaterials investigated in this thesis

Sample	**Synthesis method**	**Starting materials**	**Preparation process**
Nanocrystalline $BaLiF_3$:Sm^{3+}	Ball milling	1 mmol BaF_2 (Sigma-Aldrich), 1 mmol LiF (Ajax Chemicals) and 0.005 mmol $SmCl_3.6H_2O$ (Sigma-Aldrich, ACS grade)	(i) 90 min ball milling (ii) 30 min at 50 °C (iii) 90 min ball milling
Nanocrystalline $BaLiF_3$:Sm^{3+}	Ball milling	(1-x) mmol BaF_2 (Laboratory made), 1 mmol LiF (Ajax Chemicals) and x mmol SmF_3 (Sigma-Aldrich, ACS grade)	(i) 2 hours ball milling (ii) 1 hour at 50 °C (iii) 2 hours ball milling
Nanocrystalline $BaLiF_3$:Tm^{3+}	Ball milling	1 mmol BaF_2 (Laboratory made), 1 mmol LiF (Ajax Chemicals) and 0.005 mmol $TmCl_3.6H_2O$ (Sigma-Aldrich)	(i) 90 min ball milling (ii) 30 min at 50 °C (iii) 90 min ball milling
Nanocrystalline $BaLiF_3$:Eu^{3+}	Ball milling	1 mmol BaF_2 (Sigma-Aldrich), 1 mmol LiF (Ajax Chemicals) and 0.005 mmol $EuCl_3.6H_2O$ (Sigma-Aldrich)	(i) 90 min ball milling (ii) 30 min at 50 °C (iii) 90 min ball milling
Nanocrystalline $BaLiF_3$:Yb^{3+}, Er^{3+}	Ball milling	(1-x) mmol BaF_2 (Laboratory made), 1 mmol LiF (Ajax Chemicals), 0.01 mmol $ErCl_3.6H_2O$ (Sigma-Aldrich) and x mmol YbF_3 (Sigma-Aldrich)	(i) 2 hours ball milling (ii) 1 hour at 50 °C (iii) 2 hours ball milling
Nanocrystalline $BaLiF_3$	Ball milling	1 mmol BaF_2 (Laboratory made) and 1 mmol LiF (Ajax Chemicals)	(i) 90 min ball milling (ii) 30 min at 50 °C (iii) 90 min ball milling

3.1.2 Annealing process

Some of the as-prepared powder samples were annealed after the ball milling process. This was carried out using either a Labec box furnace (CEMLS-SD) or muffle tube furnace (GSL-1100). All samples were annealed while contained in open crucibles. The atmosphere in the muffle tube furnace was controlled by a slow gas flow (argon/nitrogen/hydrogen/oxygen).

3.2 Structural characterization of powder samples

3.2.1 Powder X-ray Diffraction (XRD)

The crystal structure of the powder samples was investigated by utilizing a Rigaku Miniflex 600 benchtop diffractometer operated at 40 kV and 15 mA with a Cu-Kα ($\lambda = 0.154$ nm) X-ray source. The diffractometer was calibrated by using a Rietveld refinement of the Lanthanum hexaboride (LaB_6) pattern. All the powder X-ray diffraction data were collected at room temperature in the 2-θ range of 10° to 90° with a step size of 0.02° and a scan speed of 0.5° min^{-1}. Rietveld refinements of measured X-ray diffraction patterns was performed by using the MAUD (Material Analysis Using Diffraction) software package [170] and initial information on the space group and lattice parameters taken from the literature [171].

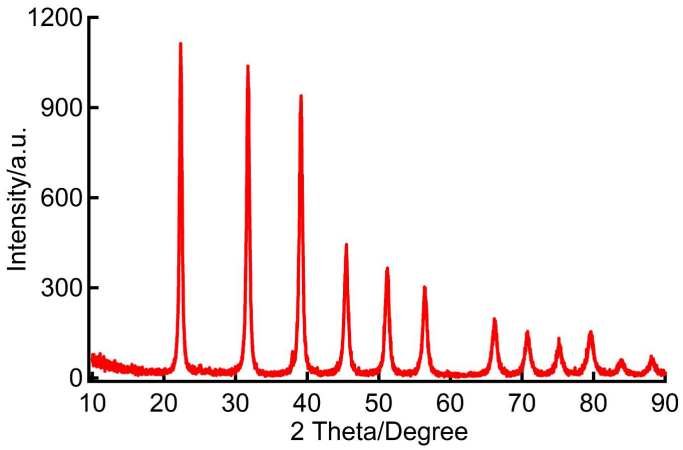

Figure 3.1: A typical powder X-ray diffraction pattern of ball-milled $BaLiF_3$ doped with Sm^{3+} measured by a Rigaku Miniflex 600 benchtop diffractometer.

3.2.2 Transmission Electron Microscopy (TEM)

TEM micrographs and energy-dispersive X-ray (EDS) map of samples were recorded on a FEI Tecnai G2 Spirit transmission electron microscope and on a JEOL JEM-2100F field emission transmission electron microscope with an accelerating beam voltage of 200 kV. Prior to perform the experiment the powder samples were suspended in ethanol and then dispersed on a copper grid. Particle size distributions were evaluated by inspecting the micrographs with ImageJ [172].

3.2.3 Scanning Electron Microscopy (SEM)

The Scanning electron microscopy (SEM) and SEM based energy-dispersive X-ray (EDS) mapping of nanocrystalline materials were performed with a Zeiss Crossbeam 540 with SDD EDS (Oxford Instruments X-MaxN).

3.3 X-ray Photoelectron Spectroscopy (XPS)

XPS measurement was carried out on a ESCALAB250Xi (Thermo Scientific, UK) X-ray photoelectron spectrometer to investigate the oxidation states of atoms of selected powder samples. The XPS spectra were excited by a mono-chromated Al Kα (energy 1486.68 eV) X-ray radiation source (spot size 500 μm) and operated with a power of 120 W (13.8 kV $\times$ 8.7 mA). The photoelectron take-off angle was 90° with a pass energy of 100 eV for survey scans or 20 eV for region scans. Binding energy scale calibration was performed by utilizing gold (Au $4f^7$ = 83.96 eV), silver (Ag $3d^5$ = 368.21 eV) and copper (Cu $2p^3$ = 932.62 eV) as calibrants. C 1s = 284.8 eV was used as adventitious hydrocarbon for binding energy reference. Avantage software was used for data processing.

3.4 Ultra-violet to visible (UV-VIS) spectroscopy

Transmission spectra of optical filters that were used for spectroscopic measurements were recorded on a CARY-50 UV/Vis spectrophotometer. Data were collected in the wavelength range of 190-1100 nm after a baseline correction.

3.5 Photoluminescence (PL) Spectroscopy

Photoluminescence measurements of nanocrystalline powder samples were performed at in the temperature range of 2 K to 293 K. Powder samples were manually pressed with a glass slide into a round and shallow counterbore (5 mm diameter and 0.5 mm depth) located at the centre of a black round/square sample holder (25 mm × 25 mm × 1.5 mm) as shown in Figure 3.2. To protect the powder sample, the counterbore was covered by a commercial Sellotape with minimal autofluorescence. Finally, the black dosimeter was mounted on the sample holder, in a Fluoromax-3 fluorometer or of a closed cycle cryostat (CTI-Cryogenics Cryodyne model 22) or of a cold stage of a closed cycle refrigerator (Janis/Sumitomo SHI-4.5) [173].

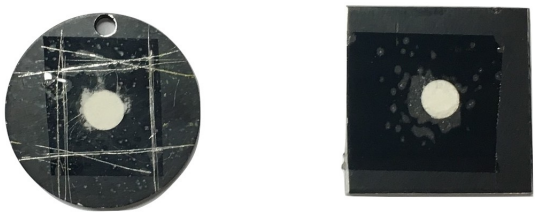

Figure 3.2: Round and square dosimeters (filled with powder samples) used for the photoluminescence spectroscopy.

The photoluminescence measurements were performed using a Fluoromax-3 spectrometer and a Spex 500M monochromator and a Spex 1704 1m monochromator [174].

The Fluoromax-3 spectrometer comprises an ozone free xenon arc lamp, two monochromators located before (Czerny-Turner excitation monochromator with 1200 gr/mm grating blazed at 330 nm) and after (Czerny-Turner emission monochromator with 1200 gr/mm grating blazed

at 550 nm) the sample holder, a photomultiplier tube, and a reference photodiode to measure the excitation light intensity.

Figure 3.3 illustrates a representative photoluminescence spectrum of nanocrystalline $BaLiF_3$:Sm^{3+} after X-irradiation which was measured at room temperature using the Fluoromax-3 spectrometer as described above. In this case, a blue band-pass (Schott, BG25) and a yellow long-pass optical glass filter (Schott, GG475) were placed at the entrance and exit of the sample compartment, respectively. The luminescence spectrum was recorded with a single scan ranging from 520-750 nm.

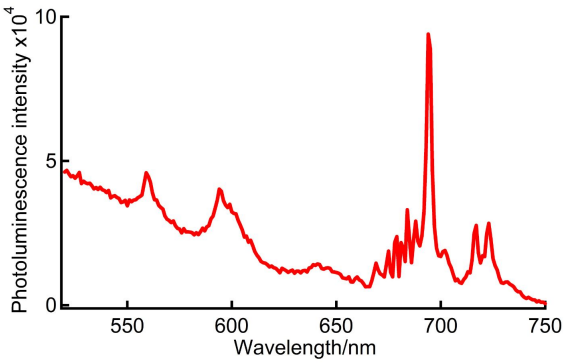

Figure 3.3: Room temperature photoluminescence spectrum of X-irradiated $BaLiF_3$:Sm^{3+}.

Alternatively, and in particular for measurements at various temperatures, a Spex 500M monochromator (150 or 1200 gr/mm grating blazed at 500 nm) equipped with either Andor iDus camera (Model DV401A-BV Si CCD) or Andor iDus InGaAs camera (Model DU490A-1.7, 600-1700 nm) was used to record the room temperature and low temperature photoluminescence spectra of nanocrystalline powder samples. In this case, both cameras were cooled down to -60 °C. For the temperature-dependent photoluminescence measurements, a closed-cycle cryostat, with a two-stage Gifford-McMahon cooling cycle, (CTI-Cryogenics Cryodyne model 22) was employed to achieve temperatures within the range of 8-293 K. The cold head of the cryostat was connected to a helium compressor unit (CTI- Cryogenics 8200), a Pfeiffer

turbomolecular vacuum pump station and an auto-tuning temperature controller (Scientific Instruments, Model 9700). A schematic of the experimental setup using the Spex 500M monochromator is depicted in Figure 3.4.

A continuous wave LED or a laser diode was used to illuminate the sample. The light source was filtered and collimated before focusing onto the sample. The emitted light from the sample was collimated and focused on to the entrance slit of a Spex 500M monochromator (either 150 or 1200 grooves/mm grating blazed at 500 nm) equipped with a highly efficient CCD camera (either Si CCD for ultraviolet to near-infrared light or InGaAs CCD for infrared light emission). A filter, selected according to the wavelength range, was placed into the light path of the collected emission to avoid excitation light reaching the cameras.

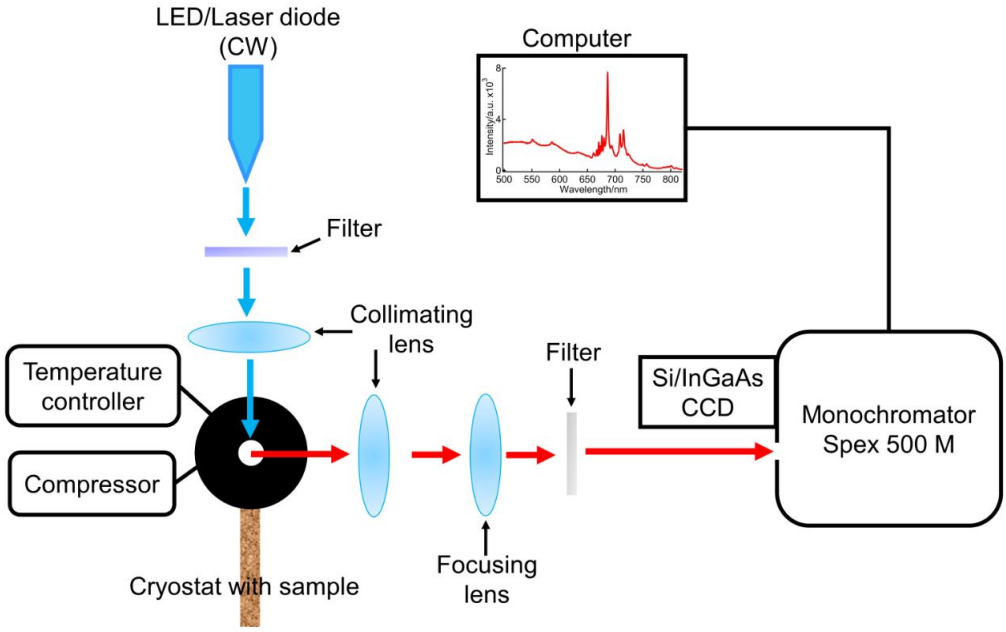

Figure 3.4: Schematic diagram of the experimental setup for photoluminescence spectroscopy with a SPEX 500M monochromator equipped with CCD camera (Si CCD or InGaAs CCD).

Representative spectra of X-irradiated $BaLiF_3:Sm^{3+}$ collected on the Spex 500 M monochromator equipped with two different diffraction gratings are shown in Figure 3.5. The spectra illustrate the X-ray induced Sm^{2+} peak at 694 nm in nanocrystalline $BaLiF_3:Sm^{3+}$.

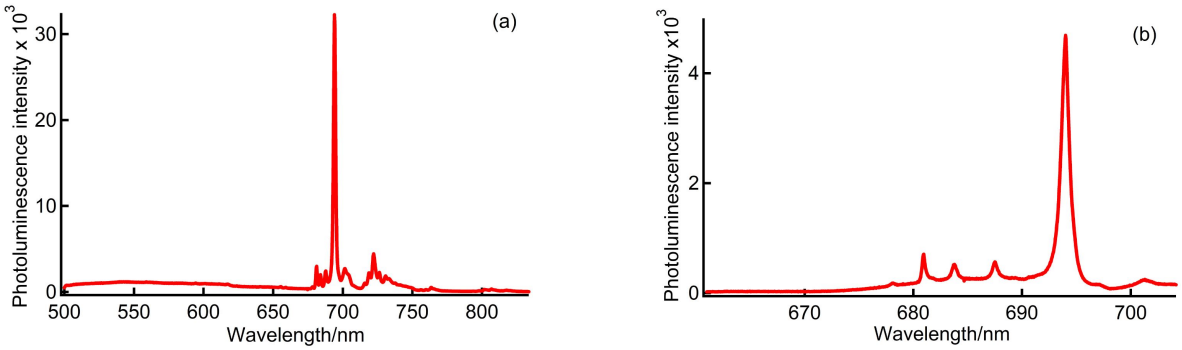

Figure 3.5: Low temperature photoluminescence spectroscopy of X-irradiated $BaLiF_3:Sm^{3+}$ collected on the Spex 500M monochromator/spectrograph equipped with a (a) 150 gr/mm or (b)1200 gr/mm diffraction grating respectively. The spectra were measured on the Si CCD camera.

3.5.1 High resolution photoluminescence spectroscopy

High resolution photoluminescence measurements were conducted by employing a Spex 1704 1m monochromator equipped with a 1200 grooves/mm grating blazed at 500 nm. Figure 3.6 illustrates a schematic diagram of the overall experimental setup used for high resolution photoluminescence measurements.

First, the sample was mounted on the cold finger of a closed-cycle refrigerator (Janis/Sumitomo SHI-4.5). The cryostat was controlled by a Sumitomo CKW-21 Helium compressor unit, a Pfeiffer turbomolecular vacuum pump and a Lakeshore 330 autotuning temperature controller. The sample was illuminated by a LED or laser diode (continuous wave mode). Then the collimated luminescence was mechanically chopped by an optical chopper (Thorlabs MC1000) before being focused onto the entrance slit of the Spex 1704 1 m monochromator. The emission was detected by a photomultiplier tube (Hamamatsu R928) and processed by a current to voltage preamplifier (Femto DLPCA-200) and a lock in amplifier (Stanford Research System, Model SR810 DSP).

A typical photoluminescence spectrum obtained using this setup is shown in Figure 3.7. The

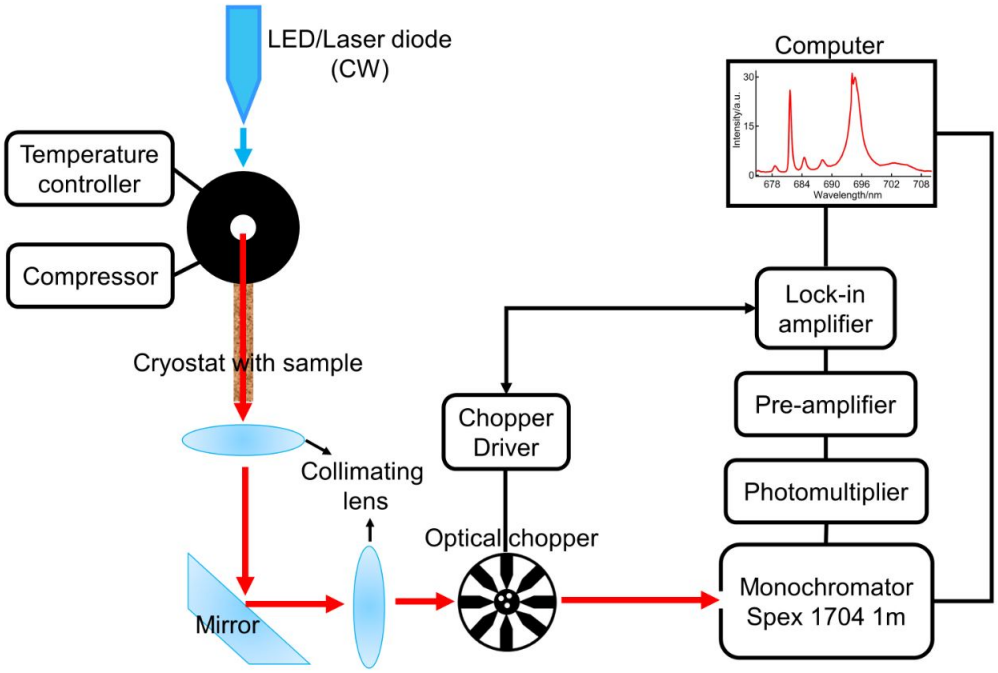

Figure 3.6: Schematic diagram of the experimental setup for high resolution photoluminescence spectroscopy.

spectrum shows the emission pattern of nanocrystalline $Ba_{0.8}Sr_{0.2}LiF_3:Sm^{3+}$ within wavelength range of 672 – 708 nm after X-irradiation.

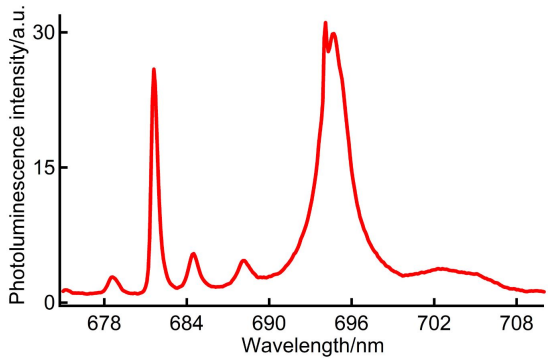

Figure 3.7: Low temperature photoluminescence spectra of $Ba_{0.8}Sr_{0.2}LiF_3:Sm^{3+}$ after X-irradiation accumulated on Spex 1704 1m monochromator.

Detail of the specific photoluminescence setup for different rare earth ions doped $BaLiF_3$ samples is given in **Table 3.2**.

Table 3.2: A brief description of photoluminescence measurement carried out in this thesis.

Sample	Excitation source	Read-out	Optical filters	Cameras
$BaLiF_3:Sm^{3+}$	462 nm laser diode	Sm^{2+} $^5D_0 \rightarrow {}^7F_1$ (694 nm), $^5D_0 \rightarrow {}^7F_0$ (680 nm)	FB 450-40 FEL 500	Model DV401A-BV
$BaLiF_3:Tm^{3+}$	365 nm LED, 462 nm laser diode	Tm^{3+} $^1D_2 \rightarrow {}^3F_4$ (451 nm), $^1G_4 \rightarrow {}^1F_4$ (642 nm), $^1D_2 \rightarrow {}^3H_2$ (649 nm) Tm^{2+} $^2F_{5/2} \rightarrow {}^2F_{7/2}$ (1136 nm)	FEL 500, FEL 1000	Model DV401A-BV, Model DU490A-1.7
$BaLiF_3:Eu^{3+}$	265 nm LED	Eu^{3+} $^5D_0 \rightarrow {}^7F_1$ (593 nm), $^5D_0 \rightarrow {}^7F_2$ (613 nm) Eu^{2+} $^6P_{7/2} \rightarrow {}^8S_{7/2}$ (360 nm), $4f^5 5d \rightarrow 4f^7$ (423 nm)	265 nm band pass, 300 FH 90-25	Model DV401A-BV
$BaLiF_3:Yb^{3+}$, Er^{3+}	980 nm laser diode, 365 nm LED	Er^{3+} $^2H_{11/2} \rightarrow {}^4I_{15/2}$ (521 nm), $^4S_{3/2} \rightarrow {}^4I_{15/2}$ (540 nm), $^4F_{9/2} \rightarrow {}^4I_{15/2}$ (650 nm) Yb^{3+} $^2F_{5/2} \rightarrow {}^2F_{7/2}$ (980 nm)	FES 750, FGUV-UG-1, FEL 700	Model DV401A-BV
$BaLiF_3$	462 nm laser diode	$F_3{}^+$ (765 nm)	FEL 500	Model DV401A-BV

3.6 Lifetime measurements

The excited state lifetime of UV and X-ray induced Sm^{2+} ions and the $F_3{}^+$ centres in nanocrystalline $BaLiF_3:Sm^{3+}$ and pure $BaLiF_3$ respectively was measured. The experimental setup used in these cases is shown in Figure 3.8. A blue LED (430 nm for $BaLiF_3:Sm^{3+}$ and 470 nm for pure $BaLiF_3$) was operated in pulsed mode by employing a pulse generator (TGP 110 10 MHz). The data were collected by the Spex 1704 1m monochromator (Sm^{2+} and $F_3{}^+$ emission was monitored at 694 and 765 respectively) using the photomultiplier tube (Hama-

matsu R928). The optical signals from the photomultiplier was pre-amplified and averaged by a preamplifier (Femto DLPCA-200) and a digital oscilloscope (LeCroy Wavesurfer 422), respectively.

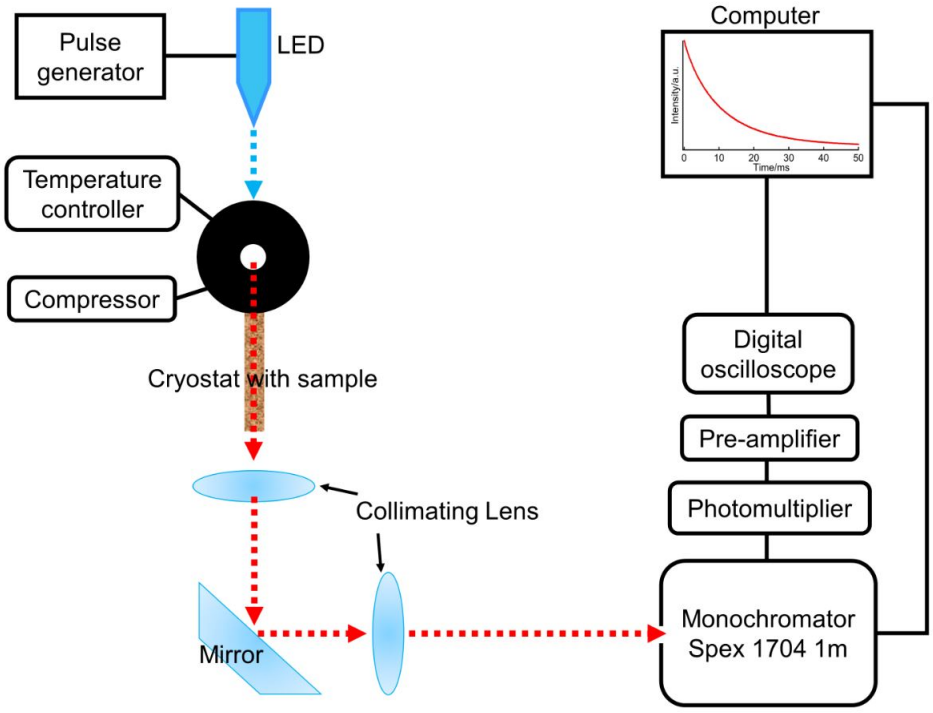

Figure 3.8: Schematic diagram of the experimental setup for excited state lifetime measurement.

3.7 Measurement of excitation spectra

Low temperature excitation spectrum of the F-centre aggregate (F_3^+) in $BaLiF_3$ was also measured on the Fluoromax-3 spectrometer and the setup is depicted schematically in Figure 3.9. The excitation monochromator was scanned within the range of 400-720 nm and the emission was monitored at 765 nm. The fluorometer was operated by the DataMax spectroscopy software. To achieve low temperatures, the sample was mounted in a liquid nitrogen (N_2) cryostat (laboratory made) which allowed the measurement of samples at a temperature as low as 77 K. The cryostat was placed into the Fluoromax sample compartment and the

sample was aligned by real time control (RTC) to obtain an optimal signal. The excitation and emission monochromator slits were set to 0.5 nm and 2 nm bandpass respectively. A short-pass filter FGS 900 and band-pass filter FB750 (FWHM 40) were used as excitation and emission filters respectively. Data were collected with single scan of 0.5 nm step increment with an integration time of 0.5 s.

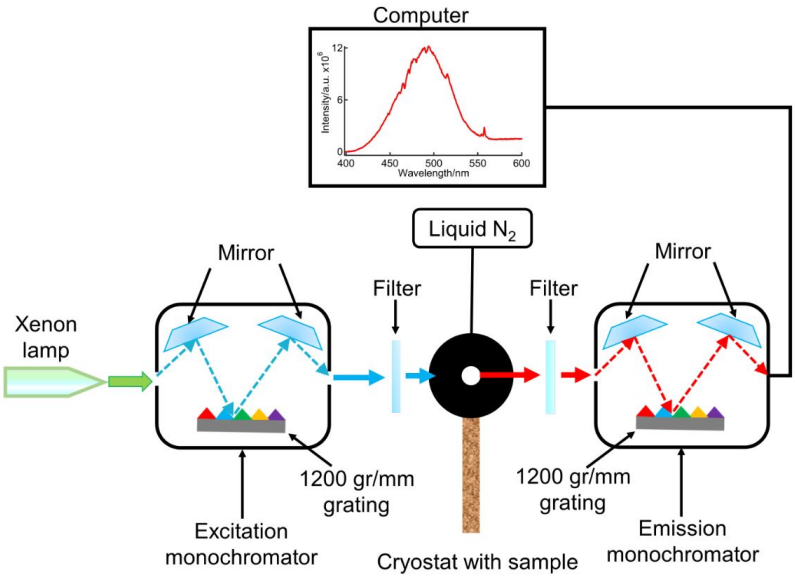

Figure 3.9: Excitation spectrum of an annealed $BaLiF_3$ sample (λ_{em} = 765 nm) at 77 K.

3.7.1 Low resolution excitation spectra

The excitation spectra of the F_3^+ band in $BaLiF_3$ in the 765 nm region was measured separately. This experiment was designed to observe the F_3^+ vibrational sideline emission at 810 nm upon 763 - 767 nm excitation at low temperature. A schematic of the experimental set-up is illustrated in Figure 3.10. The Fluoromax-3 served as the excitation fluorometer in this case and measurements were conducted at one wavelength at a time i.e. point-wise. The slit width of the Fluoromax excitation monochromator was set to 0.5 nm. A yellow long pass square colour filter (Schott, GG475) was placed to filter the excitation light. Then the light beam was collimated by using 200 mm and 125 mm lenses respectively and directly sent onto the sample mounted in the closed-cycle cryostat (8 K). To read-out the luminescence at 810

nm upon 763-767 nm excitation (Xenon lamp) the Spex 500M monochromator (1200 gr/mm grating blazed at 500) equipped with the Andor iDus Si CCD was employed. A Thorlabs long pass filter (FEL 500) was used in front of the emission monochromator.

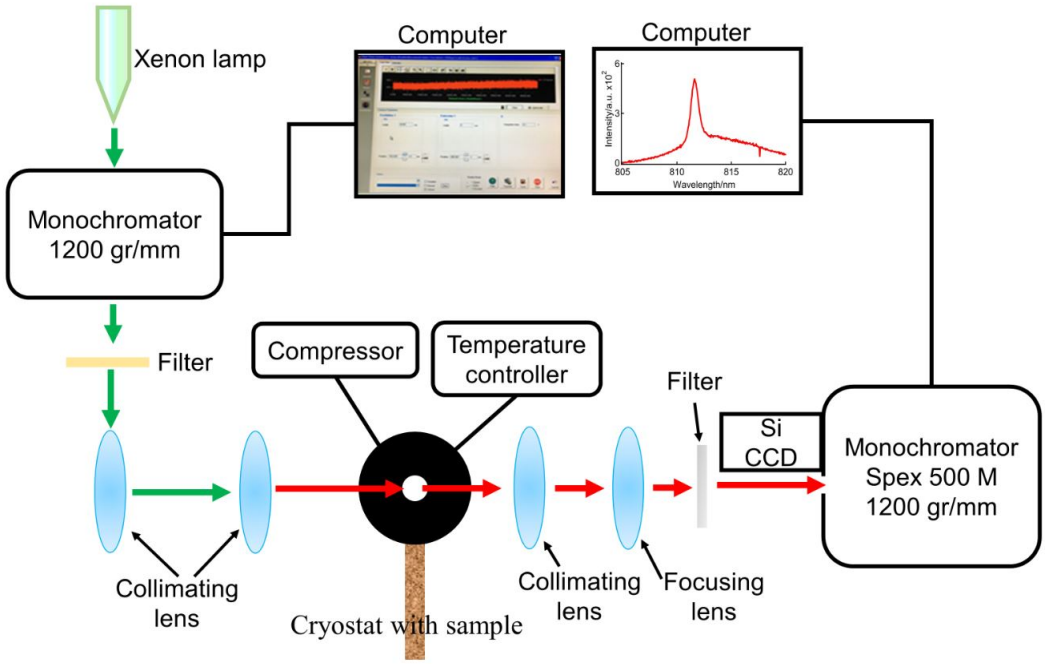

Figure 3.10: Excitation spectrum of $BaLiF_3$ at ~763-767 nm region monitoring the emission at λ_{em} = 810 nm by combining the Fluoromax-3 spectrometer as the excitation source with the Spex 500M monochromator as the emission spectrometer.

3.7.2 High resolution excitation spectra

The high-resolution excitation spectra of the F_3^+ band within 760-770 nm range was measured further. The experimental setup is illustrated in schematic diagram shown in Figure 3.11. A 780 nm LED light source (equipped with Thorlabs FES 800 filter) was used as excitation source and passed through the entry slit of the Spex 1704 1m monochromator (1200 gr/mm grating). The output light from exit slit was chopped by an optical chopper (Thorlabs MC1000 controlled by a chopper driver) and collimated by the collimating lens (200 mm and 75 mm respectively). Afterward, the collimated light beam was sent to the sample mounted in liquid helium (2 K) cryostat. A photomultiplier tube (Hamamatsu R943-02) attached with a PMT

cooler controller (Edinburgh Instruments, Model No. 7602, Serial No. 616194) was set after the sample cryostat to detect the signal. The photomultiplier tube was equipped with a RG 780, a FEL 800 and three FB 810-10 Thorlabs filters and with two 75 mm lenses. The final signal was processed by utilizing a current-voltage pre-amplifier along with a lock-in amplifier before visualizing in the PC.

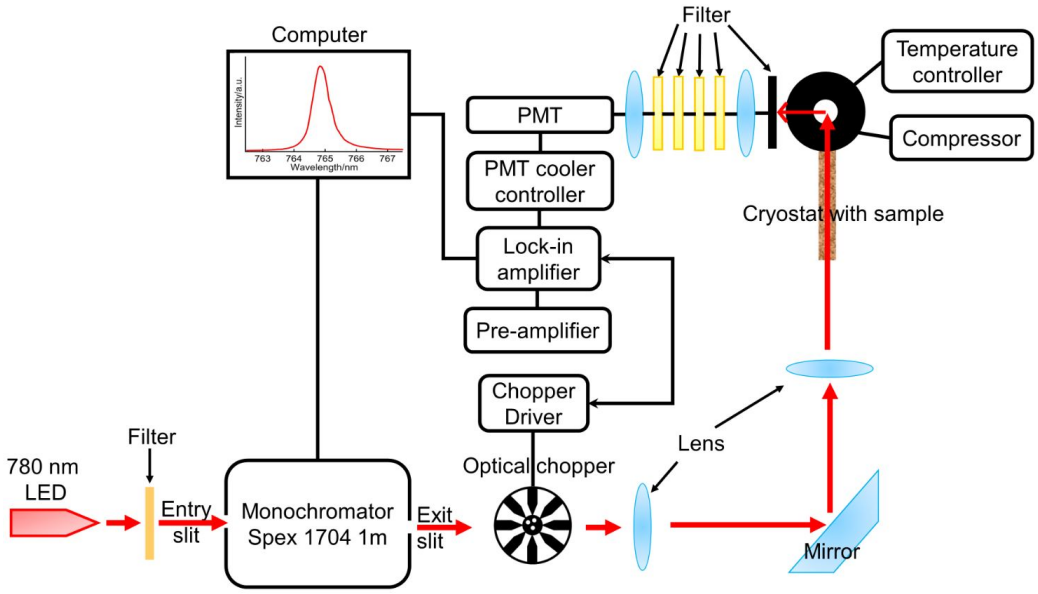

Figure 3.11: High resolution excitation spectrum of F_3^+ band in $BaLiF_3$ at 765 nm region measured on Spex 1704 1m monochromator.

3.8 Zeeman Experiment

Zeeman experiments were performed on a commercial physical property measurement system (PPMS-9, Quantum Design) which mainly comprises of a liquid helium cryostat and a superconducting magnet [175]. The cryostat temperature is variable within the range of 2–293 K and the magnet can produce a maximum magnetic field up to 9 Tesla.

For optical measurements, the PPMS system was coupled to the photoluminescence spectroscopy setup (Figure 3.4, excluding closed-cycle helium cryostat) by a 2 m-long optical fiber (Thorlabs BF13LSMA02) as shown in Figure 3.12. The powder sample was placed in the coun-

terbore (5.05 mm diameter, 1.70 mm depth) created on top of the sample puck (laboratory made). One end of the fiber was fixed with the sample by using a laboratory made sample rod guide tube. The tube equipped with the fiber and puck was inserted into the PPMS sample chamber and centered by the PPMS automatic sample centering unit ACMS-II (operated by ACMS-II software). The other end of the fiber was mounted in front of a dichroic filter (which reflects blue light and transmits red light) with the help of a Thorlabs fiber holder. A 462 nm laser diode (continuous wave mode) was used to excite the 765 nm luminescence in $BaLiF_3$. The dichroic filter was placed in such an angle that reflected blue light from the laser can pass through the fiber to excite the sample fixed at the end of the fiber. Then the red luminescence generated from $BaLiF_3$ sample was guided through the fiber bundle and transmitted by the dichroic and finally captured in a Spex 500 M monochromator (1200 gr/mm blazed at 500 nm) equipped with an Andor iDus Si CCD camera. The Zeeman effect at 765 nm in nanocrystalline $BaLiF_3$ was measured in the range of 0-9 Tesla magnetic field at a temperature 2 K. The cryostat temperature and magnetic field were controlled by the MultiVu software packages.

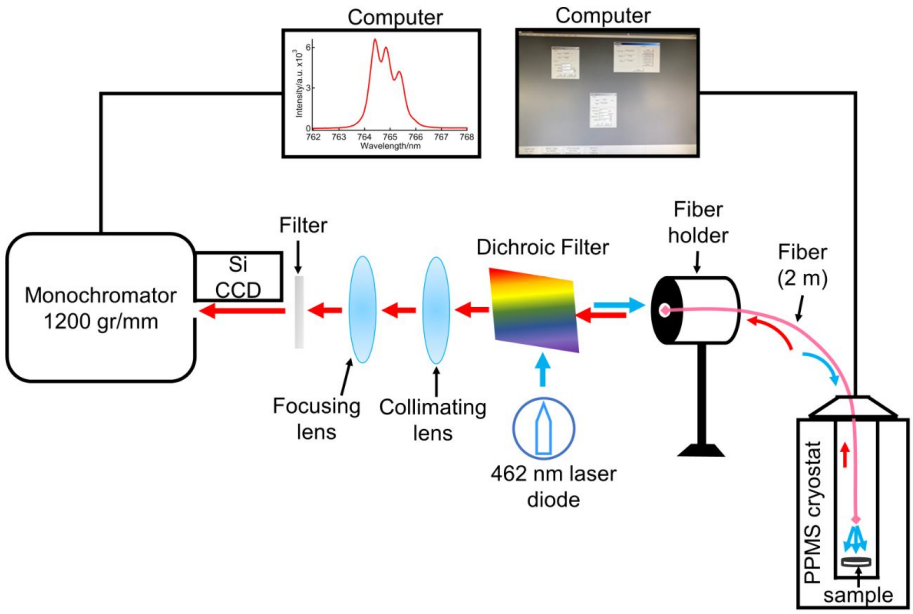

Figure 3.12: Schematic of Zeeman experiment using physical property measurement system (PPMS) setup.

Chapter 4

Generation of Sm^{2+} in nanocrystalline $BaLiF_3$:Sm^{3+}

⋆⋆⋆*The work related to this chapter has been peer-reviewed and published in The Journal of Physical Chemistry C. Dr. Nicolas Riesen is acknowlegded for his support with the transmission electron microscopy. The published article can be accessed as:*

Chowdhury, N.; Riesen, N.; Riesen, H. Efficient Generation of Stable Sm^{2+} in Nanocrystalline $BaLiF_3$:Sm^{3+} by UV- and X-irradiation. The Journal of Physical Chemistry C, 2019, 123(41), 25477-25481.⋆⋆⋆

4.1 Introduction

$BaLiF_3$ is a highly transparent optical material in the vacuum-ultraviolet (VUV) range of electromagnetic spectrum, ideal for application in many optical devices, including lenses [79]. In recent years, transition-metals-doped-$BaLiF_3$ have been a subject of increasing interest as promising laser-active medium [35, 37, 155, 156, 176] and also for its prospect in quantum computing devices and storage phosphors [36, 152]. In regard to their application as storage phosphors, investigating rare-earth ions doped $BaLiF_3$ is of fundamental scientific, and technological interest.

This chapter explores and demonstrates the UV and X-ray storage capability of Sm^{3+} doped $BaLiF_3$ obtained by a mechanochemical synthesis route. The room temperature photoluminescence spectra of nanocrystalline $BaLiF_3$:Sm^{3+} before and after UV and X-ray irradiation

are thoroughly investigated. Additionally, low temperature photoluminescence spectra of the powder samples are also measured on nanocrystalline $BaLiF_3$:Sm^{3+}. Dependence of Sm^{2+} ions as a function of radiation doses (UV and X-ray) and excitation power is explored.

4.2 Experimental details

Nanocrystalline $BaLiF_3$ doped with Sm^{3+} was prepared by ball milling using a Retsch Mixer Mill MM 200. ACS reagent grade chemicals were used without any further purification. In a first step, 1 mmol (0.175 g) BaF_2, 1 mmol (0.026 g) LiF and 0.005 mmol (2 mg) $SmCl_3.6H_2O$ (0.27 atom%) powder was ground manually by using a mortar and pestle. In a second step, the mixture was transferred into a 10 ml zirconia-lined jar with two zirconia balls of 12 mm diameter and the mixture was ball milled at 20 Hz for 3 h to yield nanocrystalline $BaLiF_3$:Sm^{3+} powder.

For comparison, a $Ba_{0.8}Sr_{0.2}LiF_3$:Sm^{3+} sample was prepared by ball milling BaF_2, LiF, SrF_2 and $SmCl_3.6H_2O$. This material is sensitive to heat-treatment as a result ball milling process was carried out in a planetary ball mill (Fritsch, PL premium line) at rotation speed of 600 rpm for 3 h.

The phase purity of the material was verified by powder X-ray diffraction (XRD), employing a Rigaku MiniFlex-600 benchtop powder diffractometer. The measurement was performed with Cu-Kα ($\lambda = 0.154$ nm) radiation operating at 40 kV and 15 mA. The powder diffraction pattern was collected in the 2-θ range of 10-90° with a step size of 0.02° and a scan speed of 0.5° min^{-1}.

Room temperature and low-temperature photoluminescence spectra were excited by the focused light of a 462 nm laser diode. The emission spectra were collected by a Spex 500 M monochromator (150 or 1200 grooves per mm grating blazed at 500 nm) equipped with an Andor iDus camera (DV401A-BV Si CCD) cooled to -60 °C.

The nanocrystalline $BaLiF_3$:Sm^{3+} powder was X-irradiated by the Rigaku MiniFlex diffractometer or exposed to UV irradiation by a Hg(Ne) UV lamp (Newport 6034 Hg(Ne) calibration pen lamp). The dose rate of the Rigaku diffractometer was cross-calibrated by a Sirona Heliodent dental X-ray source with known radiation doses.

4.3 Characterization of as-prepared $BaLiF_3:Sm^{3+}$ sample

4.3.1 Powder X-ray diffraction (XRD) pattern

$BaLiF_3$ is an inverse perovskite and crystallizes in a simple cubic structure with the space group Pm-3m [71, 177, 178]. The XRD pattern of nanocrystalline $BaLiF_3:Sm^{3+}$ as-prepared by ball milling is shown in Figure 4.1. All the prominent peaks can be indexed to the aforementioned structure. The Rietveld refinement (using the MAUD software package) [170] shown in Figure 4.1 indicates a slight expansion of the lattice parameter (a = 4.003(3) Å) by about 0.2% from the standard value reported in the literature (a = 3.996(3) Å) [71] and an average crystal size of 36 ± 1 nm. The Rietveld refinement converged with final fitting parameters of R_{wp} = 19.6% and R_{exp} = 13.1% respectively, yielding a goodness of fit G = R_{wp}/R_{exp} of 1.49. It is noted here that G < 2 values are considered to indicate good refinements [179].

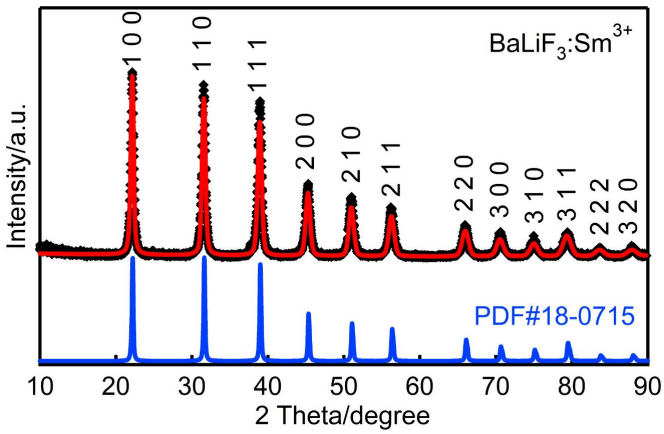

Figure 4.1: Powder X-ray diffraction pattern of nanocrystalline $BaLiF_3:Sm^{3+}$. Experimental data points are shown as black diamonds, the solid (red) trace is the Rietveld refinement and standard data for cubic $BaLiF_3$ (PDF # 18-0715) is shown as the solid blue trace.

4.3.2 Transmission electron microscopy (TEM) of $BaLiF_3:Sm^{3+}$

Figure 4.2 displays a typical transmission electron microscopy (TEM) micrograph of the Sm^{3+}-doped $BaLiF_3$ nanocrystals prepared by 3 h of high energy ball milling.

The average particle size from TEM micrographs was determined to be 31 nm (TEM) which is reasonably close to the XRD result (36 ± 1 nm). The histogram in Figure 4.2 was generated from the analysis of 40 crystallites in four TEM images (only well-separated crystallites were

taken into account) to illustrate the crystallite size distribution.

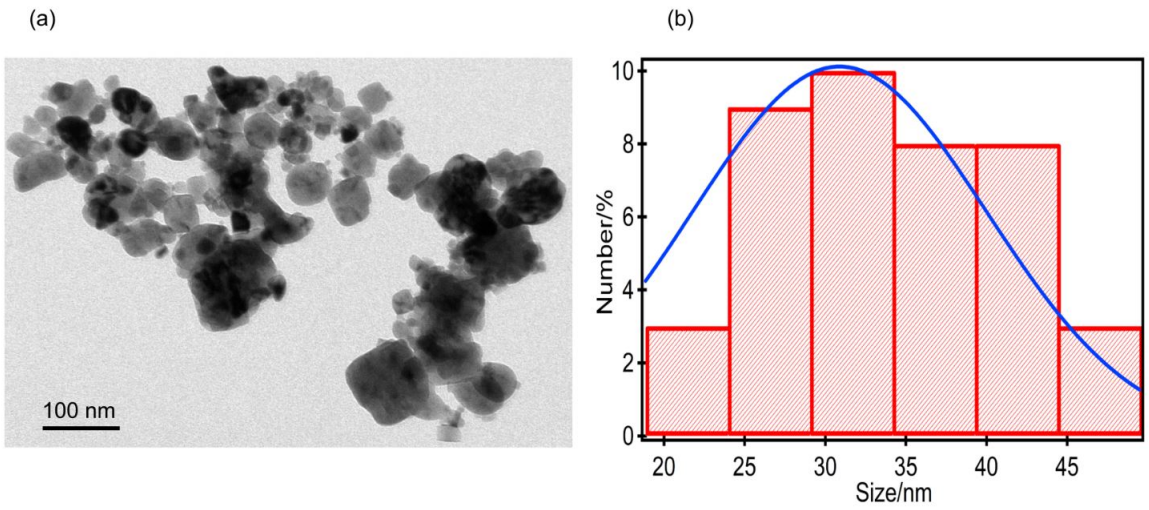

Figure 4.2: Typical TEM image of nanocrystalline $BaLiF_3:Sm^{3+}$ prepared by ball milling. The size distribution of 40 crystallites is illustrated as a histogram with a Gaussian fit with full width at half maximum of ∼20 nm (solid blue line).

4.4 Photoluminescence spectroscopy of $BaLiF_3:Sm^{3+}$

4.4.1 X-ray sensitivity of $BaLiF_3:Sm^{3+}$ nanophosphor

The reduction of Sm^{3+} to Sm^{2+} in the $BaLiF_3$ host upon X-ray exposure was monitored by photoluminescence measurements. Figure 4.3 illustrates the room temperature photoluminescence spectra of the $BaLiF_3:Sm^{3+}$ nanophosphor (a) before and (b) after X-irradiation.

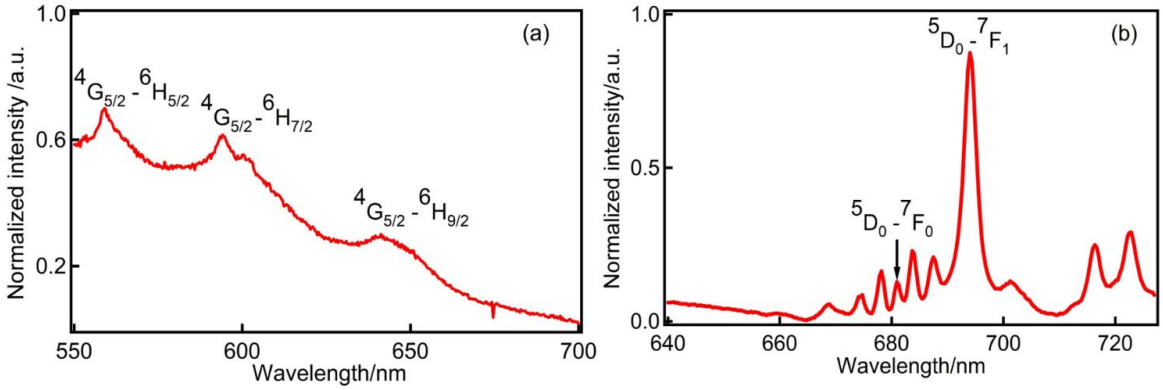

Figure 4.3: Photoluminescence spectra of nanocrystalline $BaLiF_3:Sm^{3+}$ (a) before and (b) after X-ray irradiation (35 Gy dose) at 293 K. The luminescence was excited at 462 nm.

Before X-irradiation only relatively broad Sm^{3+} peaks are visible at around 559, 594 and 641 nm which can be assigned to the $^4G_{5/2} \rightarrow {}^6H_{5/2}$, $^4G_{5/2} \rightarrow {}^6H_{7/2}$ and $^4G_{5/2} \rightarrow {}^6H_{9/2}$ transitions, [78] respectively. These transitions superimpose on a broad luminescence background that most likely arises from intrinsic defects in the $BaLiF_3$ host such as oxide ion impurities. Importantly, no Sm^{2+} peaks are observed before the X-irradiation. Upon X-irradiation, a relatively narrow peak at 694 nm along with some strong vibronic sidebands begins to appear. This relatively intense and sharp peak at 694 nm can be assigned to the $^5D_0 \rightarrow {}^7F_1$ f-f transition of Sm^{2+} [150].

4.4.2 Low temperature photoluminescence spectroscopy of $BaLiF_3$:Sm^{3+}

Figure 4.4a illustrates the temperature dependence of the photoluminescence spectrum of Sm^{2+} generated by X-irradiation of the $BaLiF_3$:Sm^{3+} nanophosphor. Again, the 462 nm laser diode was employed as the excitation source and the photoluminescence spectra were recorded in the temperature range of 16-240 K. With increasing temperature, the most prominent peak of Sm^{2+} at 694 nm ($^5D_0 \rightarrow {}^7F_1$) becomes slightly broader and the vibronic sidebands (Vb) show increased intensity. From this temperature dependence, the weak line at 681 nm can be assigned to the $^5D_0 \rightarrow {}^7F_0$ transition. This transition is magnetic dipole forbidden because of the inversion symmetry of the Ba^{2+} site where the Sm^{2+} substitutes and hence is very weak. In contrast, the magnetic dipole allowed $^5D_0 \rightarrow {}^7F_1$ transition at 694 nm is the most prominent feature in the spectrum at all temperatures.

Figure 4.4b illustrates the temperature dependence photoluminescence spectrum of Sm^{2+} generated by X-irradiation in $Ba_{0.8}Sr_{0.2}LiF_3$:Sm^{3+}. Interestingly, it shows that an admixture of SrF_2 in $Ba_{0.8}Sr_{0.2}LiF_3$:Sm^{3+} slightly breaks the centre of symmetry ($BaLiF_3$) rule and enhances the luminescence intensity of electric-dipole forbidden Sm^{2+} $^5D_0 \rightarrow {}^7F_0$ (681 nm) transition. However, the magnetic dipole forbidden $^5D_0 \rightarrow {}^7F_1$ Sm^{2+} transition (694 nm) dominates the photoluminescence spectra of nanocrystalline $Ba_{0.8}Sr_{0.2}LiF_3$:Sm^{3+} as like as $BaLiF_3$:Sm^{3+} nanophosphor (shown in Figure 4.4a).

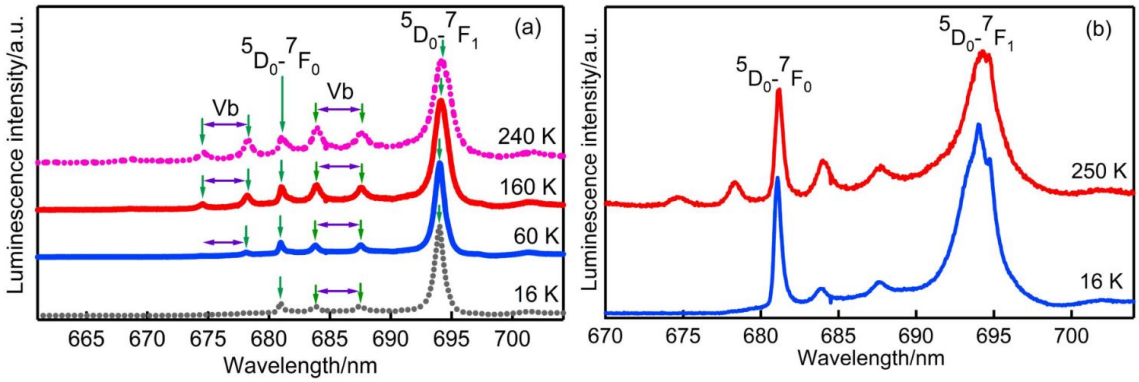

Figure 4.4: Temperature dependence of the photoluminescence spectra of X-irradiated (a) $BaLiF_3:Sm^{3+}$ and (b) $Ba_{0.8}Sr_{0.2}LiF_3:Sm^{3+}$. The Sm^{2+} emission lines at 681 and 694 nm are assigned to the $^5D_0 \rightarrow {}^7F_0$ and $^5D_0 \rightarrow {}^7F_1$ transitions, respectively. The spectra were excited at 462 nm.

4.4.3 X-ray dose dependency

The build-up of Sm^{2+} in nanocrystalline $BaLiF_3:Sm^{3+}$ as a function of cumulative X-ray dose is illustrated in Figure 4.5.

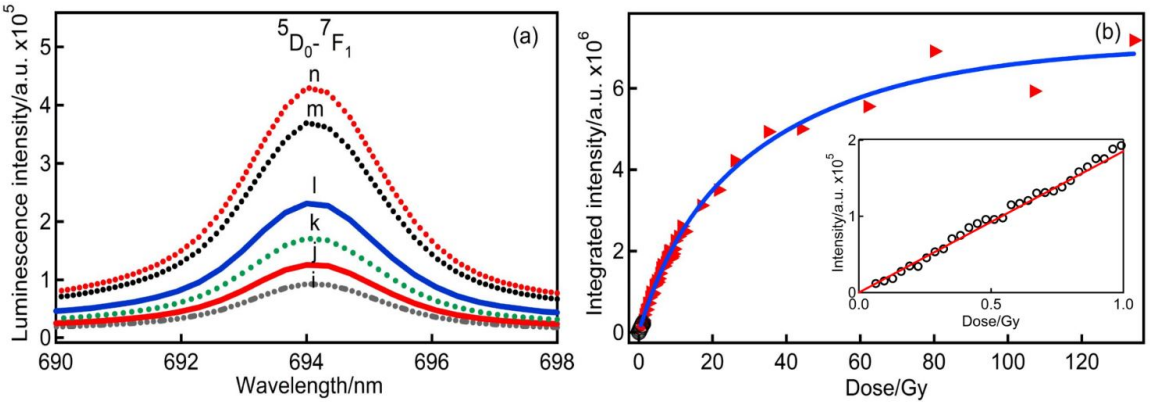

Figure 4.5: Room temperature photoluminescence spectra of $BaLiF_3:Sm^{3+}$ in the region of the $^5D_0 \rightarrow {}^7F_1$ transition (a) for increasing X-irradiation (i) 3.6, (j) 5.4, (k) 9, (l) 12, (m) 26 and (n) 35 Gy, respectively. (b) Integrated intensity of the $^5D_0 \rightarrow {}^7F_1$ Sm^{2+} transition at 694 nm as a function of increasing X-ray dose (red triangles) with a fit to a double exponential (blue trace). Calibrated data obtained from Sirona Heliodent dental X-ray is presented in black circles and is also shown as an inset.

The buildup of Sm^{2+} concentration is approximately linear up to 1.6 Gy and starts to saturate at around 80 Gy. The X-ray dose dependence of the Sm^{2+} $^5D_0 \rightarrow {}^7F_1$ transition intensity (at 694 nm) in $BaLiF_3$ was fitted by the following double exponential function, yielding rate

constants $k_1 = 0.02$ Gy^{-1} and $k_2 = 0.1$ Gy^{-1}.

$$I_{Sm^{2+}} = a_1(1 - e^{(-k_1 \times dose)}) + a_2(1 - e^{(-k_2 \times dose)}) \tag{4.1}$$

where $I_{Sm^{2+}}$ is the concentration of Sm^{2+} ions and a_1 and a_2 are amplitudes.
This double exponential fit (Figure 4.5b) provides evidence that the gradual increase of Sm^{2+} with increasing X-ray dose follows first-order dispersive kinetics i.e., there is a dispersion of rate constants. This is plausible since the Sm^{3+} needs to be charge compensated by another defect, and hence there is a distribution of Sm^{3+}-defect separations. Importantly, oxide ion impurities play an important role in the $BaLiF_3$:Sm^{3+} system and charge-compensate the Sm^{3+} centres. We note here that even for high X-ray doses, no reduction of the Sm^{3+} luminescence intensity is observed in contrast to BaFCl:Sm^{3+} [134]. This may be because the absolute conversion to Sm^{2+} is still minimal, and hence the Sm^{3+} change is not measurable within the experimental error, or the Sm^{2+} is exclusively generated from Sm^{3+}-defect pairs that are initially nonluminescent.

4.4.4 UV sensitivity and dose dependency of $BaLiF_3$:Sm^{3+}

The response of nanocrystalline $BaLiF_3$:Sm^{3+} to UV-C (185 nm; ~0.6 mW/cm^2) light is demonstrated in Figure 4.6a where the room temperature photoluminescence spectrum was measured before and after UV exposure. The sample was exposed to UV light for 1 h by using a Hg(Ne) lamp with a power density of ~0.6 mW/cm^2.
Before the UV exposure, only Sm^{3+} peaks are observed, and after UV irradiation, again the well-defined Sm^{2+} luminescence peaks appear.

Figure 4.6b summarizes the dependence of the $^5D_0 \rightarrow {}^7F_1$ transition intensity on the UV exposure. Upon 1.1 J cm^{-2} UV-fluence, the absolute concentration of Sm^{3+} centres is about 32 times lower compared to X-ray-induced reduction with 130 Gy, as follows from the absolute luminescence intensity. The photoluminescence intensity of the $^5D_0 \rightarrow {}^7F_1$ transition of Sm^{2+} ions at 694 nm follows a nearly linear response to UV irradiation within the investigated range. Clearly, the $BaLiF_3$:Sm^{3+} also has the capability of storing UV radiation in addition to the

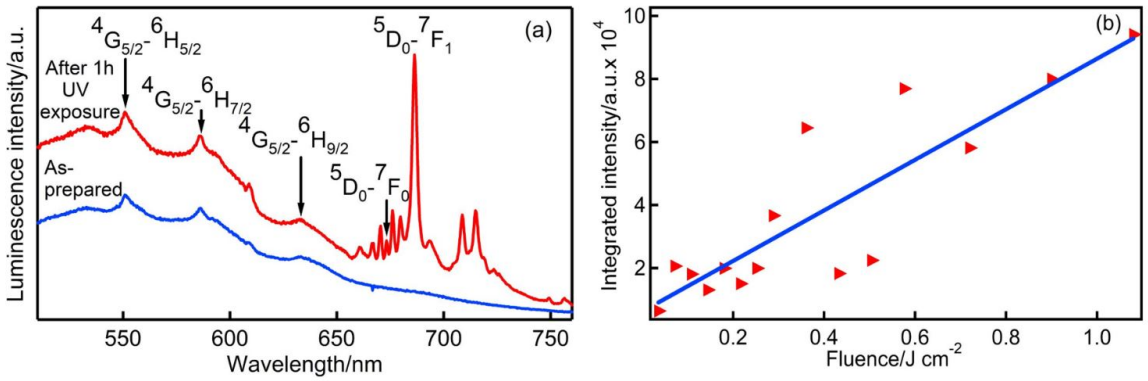

Figure 4.6: Photoluminescence spectra of nanocrystalline $BaLiF_3:Sm^{3+}$ before (blue trace) and after (red trace) UV exposure (~0.6 mW.cm^{-2}; 185 nm radiation; 1 h) at 293 K. (b) Dependence of Sm^{2+} luminescence ($^5D_0 \rightarrow {}^7F_1$) at 694 nm on UV-C exposure at 185 nm. Blue solid line represents a linear fit function. A 462 nm laser diode was used as the excitation source.

X-ray storage capacity. The UV storage effect is most likely based on photoinduced electron transfer from oxide ion impurities to the Sm^{3+} centres [124].

4.4.5 Photobleaching effect

The photoionization of Sm^{2+} ions, i.e., the conversion of X-ray generated Sm^{2+} back to Sm^{3+} was also investigated by employing a 462 nm CW (continuous wave) laser diode. In this case, the sample was first exposed to an X-ray dose of 6 Gy and was then bleached by applying ~8 W cm^{-2} of 462 nm laser light. Figure 4.7a illustrates the decreasing Sm^{2+} luminescence intensity in the $^5D_0 \rightarrow {}^7F_1$ region (694 nm) with increasing photobleaching time (from (i) to (n)).

The bleaching process of X-irradiated nanocrystalline $BaLiF_3:Sm^{3+}$ can be rationalized by assuming that the conversion efficiency of Sm^{3+} to Sm^{2+} is correlated with the distribution of the X-ray-induced Sm^{2+} and hole traps in the $BaLiF_3$ host. The separation between Sm^{2+} and hole traps can be described by a standard γ distribution. The photoionization of Sm^{2+} can be explained by dispersive first-order kinetics, where we consider that the electron transfer rate (k) from Sm^{2+} centre to nearby defect depends exponentially on the distance (R) between samarium ions and oxide ion centres.

$$k = k_0 e^{-R/a_f} \tag{4.2}$$

where k_0 is the effective rate constant and a_f is a scaling parameter.

The behaviour of k_0 as a function of excitation power indicates whether the bleaching mechanism is a single or multiphoton process. The bleaching mechanism of Sm^{2+} in the $BaLiF_3$ host can then be modelled by Equation 4.3 [124].

$$N(t) = \int_{R_m}^{\infty} \frac{(R - R_m)^{(\gamma-1)} exp[-(R - R_m)]}{\Gamma(\gamma)} exp(-k_0 e^{(-R/a_f)} t) dR \tag{4.3}$$

where *N(t)* is the normalized photoluminescence decay of Sm^{2+}, R_m is the radius of the excluded volume i.e., the nearest possible distance between the oxygen ion impurity and the Sm^{2+} ion.

In particular, the oxide impurity cannot be on the nearest neighbor F (because this would stabilize the Sm^{3+} ions) and hence the radius for the excluded volume was chosen to be R_m = 5 Å. In Equation 4.3, γ is the deviation from single exponential behaviour, i.e., it is determined by the dispersion of rates.

Figure 4.7b illustrates the bleaching of Sm^{2+} where a global fit was conducted by using Equation 4.3. A near-perfect agreement is obtained with the global parameters a_f = 0.60 ± 0.06 Å and γ = 10.5 ± 1.6, and only k_0 was left to be independent. The result for the parameter γ implies that the Sm^{2+} ions are ∼15 Å (on average) away from the hole traps. It is important to note that these parameters should not be overinterpreted since they are not fully independent. Temperature-induced diffusion of the defect pairs can increase the separation between the electron and the hole trap centres [121]. This separation can render the electron back-transfer mechanism impossible, resulting in residual Sm^{2+} of ∼20-30% for long bleaching times.

The behaviour of the independent rate constant k_0 can be fitted by a simple power law (Figure 4.7c) resulting in an exponent x = 0.8 ± 0.2. This indicates that the photobleaching of Sm^{2+} in $BaLiF_3$ is a single photon process in contrast to the multiphoton ionization in the BaFCl host lattice [124].

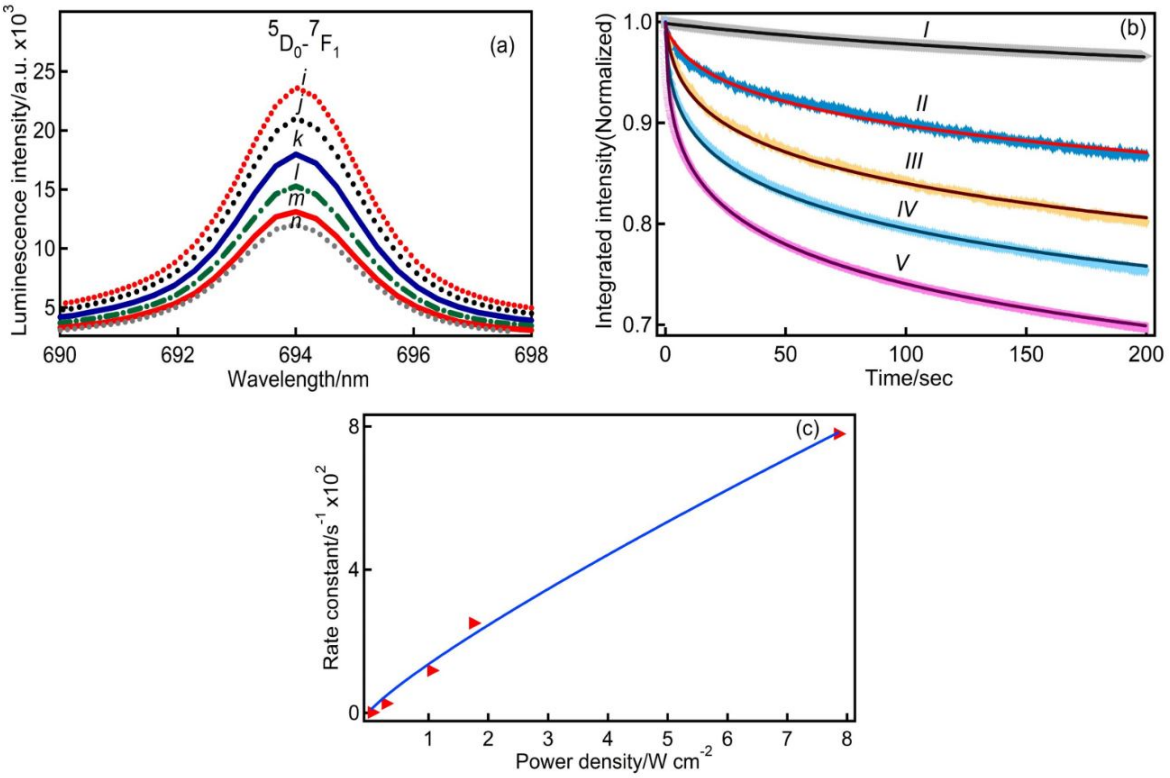

Figure 4.7: (a) Luminescence spectrum of Sm^{2+} in $BaLiF_3$ after a range of photobleaching times in the $^5D_0 \rightarrow {}^7F_1$ region: (i) 10 min, (j) 15 min, (k) 25 min, (l) 40 min, (m) 60 min, and (n) 75 min. (b) Power dependence of the Sm^{2+} photobleaching: (I) 0.06 W. cm^{-2}, (II) 0.29 W. cm^{-2}, (III) 1.05 W. cm^{-2}, (IV) 1.75 W. cm^{-2}, (V) 7.85 W. cm^{-2}, where samples were initially irradiated by a 6 Gy X-ray dose. The solid lines represent a global fit to Equation 4.3. (c) Dependence of the fitting parameter k_0 (Equation 4.2) on the power. The blue solid line is the fit to a power law.

4.5 Lifetime measurement of UV and X-ray induced Sm^{2+} ions

Figure 4.8 illustrates the photoluminescence decay of Sm^{2+} ($^5D_0 \rightarrow {}^7F_1$) excited by a pulsed 430 nm LED. The Sm^{2+} decay curve is well fitted by a double exponential function, and from the fitting parameters, the lifetimes of the X-ray- and UV-induced $^5D_0 \rightarrow {}^7F_1$ transition (694 nm) were determined. In both cases, the double exponential function yields a fast (~4 ms) and a slow (τ_{x-ray} = 12 ms, τ_{uv} = 19 ms) lifetime. Again, a double exponential is the simplest approximation to first-order dispersive kinetics, i.e., there must be a range of excited state lifetimes. It appears that UV-generated Sm^{2+} centres show longer excited state lifetimes than X-ray-generated centres. The excited state lifetime for the $^5D_0 \rightarrow {}^7F_1$ transition in X-ray induced Sm^{2+} in $BaLiF_3$ ranges between 4 and 12 ms whereas in a macroscopic crystal the

lifetime is 37 ms [151]. This indicates that the ball milling process and X-ray irradiation generate a very high concentration of defects in nanocrystalline $BaLiF_3:Sm^{3+}$ that quench the excited state. In particular, the magnetic dipole transition may couple to electric dipole transitions of such defects and hence excitation energy transfer is expected to follow a R^{-4} law [180, 181] where R is the distance between the Sm^{2+} ion and the defect.

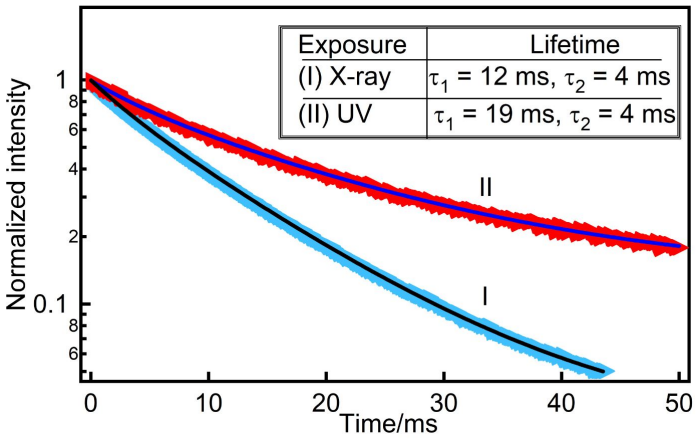

Figure 4.8: Excited state lifetime measurement of Sm^{2+} of (I) X-ray (6 Gy) and (II) UV (1 h) irradiated samples at 694 nm. Solid lines show double exponential fits.

X-irradiation resulted in significant Sm^{2+} concentrations, and hence the excited state decay most likely displays donor-acceptor and donor-donor transfer [180]. In contrast, the low-fluence UV-irradiation in this work lead to about a 32-times lower Sm^{2+} concentration, and hence the excited state decay is most likely governed by donor-acceptor energy transfer only.

4.6 Summary

Nanocrystalline $BaLiF_3:Sm^{3+}$ was prepared by ball milling BaF_2, LiF and $SmCl_3.6H_2O$ for 3 h. The phase purity of the as-synthesized powder sample was verified by powder XRD. The photoluminescence properties were investigated before and after UV and X-ray exposure. The magnetic dipole forbidden $^5D_0 \rightarrow {}^7F_0$ transition is very weak and the magnetic dipole allowed $^5D_0 \rightarrow {}^7F_1$ emission dominates the photoluminescence spectrum. The photoluminescence intensity of Sm^{2+} gradually increases upon increasing X-irradiation with rate constants $k_1 = 0.02\ Gy^{-1}$ and $k_2 = 0.1\ Gy^{-1}$, compared to $\sim$0.3 Gy^{-1} for the BaFCl host [134]. This

indicates that nanocrystalline $BaLiF_3:Sm^{3+}$ is a relatively sensitive and efficient photoluminescent phosphor. The excited state lifetime range of Sm^{2+} (694 nm) in the X-ray and UV irradiated sample is between ∼4 to 12 ms and 19 ms, respectively and the decays are indicative of donor-donor, donor-acceptor, and donor-acceptor only energy transfer.

The photobleaching of Sm^{2+} can be explained by considering a standard gamma distribution which provides evidence that the X-ray induced Sm^{2+} centres are separated from hole traps by a few interionic spacings (∼15 Å). This result is in accord with the observation that the $^5D_0 \rightarrow {}^7F_0$ transition is very weak, i.e., the inversion symmetry prevails. The symmetry would most likely be broken if defects would be within the second or even third coordination sphere, and hence the intensity would increase.

This chapter demonstrates that nanocrystalline $BaLiF_3:Sm^{3+}$ has some potential for applications in the field of dosimetry for X-ray and UV-C radiation.

Chapter 5

Generation of divalent Tm^{2+} ions in $BaLiF_3$:Tm^{3+} nanocrystals

⋆⋆⋆*The work related to this chapter has been peer-reviewed and published in The Journal of Physical Chemistry C. Dr. Nicolas Riesen is acknowledged for his support with the transmission and scanning electron microscopy, and TEM, SEM-based elemental mapping. The published article can be accessed as:*

Chowdhury, N.; Riesen, N.; Riesen, H. Photoluminescence of X-ray Induced Divalent Tm^{2+} in $BaLiF_3$:Tm^{3+} Nanocrystals. The Journal of Physical Chemistry C, 2021, 125(39), 21543-21549.⋆⋆⋆

5.1 Introduction

As discussed in Chapter 1 and 2, to explore the potential of a luminescent system as reliable X-ray storage phosphor, a detailed understanding of the host material incorporated with a broad range of activator (e.g., rare-earth elements) is essential. In addition, considering the X-ray sensitivity of $BaLiF_3$:Sm^{3+} which displays visible Sm^{2+} luminescence (at 694 nm), it is expected that X-irradiation may also generate infrared Tm^{2+} emission in nanocrystalline $BaLiF_3$:Tm^{3+}. Such an investigation allows to examine the potential of $BaLiF_3$ host matrix for solar energy applications, specifically in luminescent solar concentrators [182, 183].

This chapter provides a demonstration of infrared Tm^{2+} emission (at 1136 nm) by X-irradiation generated in nanocrystalline $BaLiF_3$:Tm^{3+} prepared by ball milling. Specifically, the X-ray

storage capability and the photoionization process of X-ray induced Tm^{2+} in $BaLiF_3$:Tm^{3+} nanophosphor are explored rigorously. Additionally, the response of nanocrystalline $BaLiF_3$: Tm^{3+} ($Tm^{3+} \rightarrow Tm^{2+}$) upon X-ray irradiation is compared with that of $BaLiF_3$:Eu^{3+} and $BaLiF_3$: Sm^{3+} nanocrystals prepared by ball milling.

5.2 Experimental Methods

BaF_2 was prepared by co-precipitation of barium nitrate $Ba(NO_3)_2$ and ammonium fluoride NH_4F. The product was then dried at 60 °C for 24 h and its phase purity was characterized by powder X-ray diffraction. Nanocrystalline $BaLiF_3$:Tm^{3+} (i.e., $Ba_{0.995}Tm_{0.005}LiF_{2.985}Cl_{0.015}$) was then synthesized by ball milling BaF_2, LiF and $TmCl_3{\cdot}6H_2O$ using a Retsch Mixer Mill MM 200. First, 0.35 gm BaF_2 (2 mmol), 0.052 g LiF (2 mmol) and 3.8 mg $TmCl_3{\cdot}6H_2O$ (0.01 mmol) were ground manually by a mortar and pestle. The mixture was then transferred into a 10 mL zirconia lined jar with two 12 mm diameter zirconia balls (5.5 gm). Finally, the Retsch mixer mill was operated at a frequency of 20 Hz for 180 min. The total weight of the mixture was about 0.41 g (i.e., ball to reagent mass ratio of 21:1).

For comparison, nanocrystalline $BaLiF_3$:Eu^{3+} and $BaLiF_3$:Sm^{3+} were synthesized by following the same preparation route.

The final products were characterized by powder X-ray diffraction employing a Rigaku Miniflex-600 benchtop powder X-ray diffractometer with a Cu-Kα ($\lambda = 0.154$ nm) tube operated at 40 kV and 15 mA. The instrumental broadening by the powder diffractometer was determined by a Rietveld refinement of a LaB_6 pattern. The experimental data was recorded in the 2-θ range of 10° to 90° with a step size of 0.02° and at a scan speed of 0.5°/min. The X-irradiation was carried out in the same diffractometer and the X-ray dose was cross-calibrated to a Sirona HELIODENT plus Dental X-ray source.

TEM (transmission electron microscopy) and EDS (energy dispersive spectroscopy) 2D elemental mapping were performed by utilizing a FEI Tecnai G2 Spirit TEM and a JEOL JEM 2100F Field Emission TEM, respectively. To record high resolution TEM images, powder samples were suspended in ethanol and then dispersed onto copper grids.

In addition, SEM (scanning electron microscopy) and SEM-EDS mapping were performed

with a Zeiss Crossbeam 540 with SDD EDS (Oxford Instruments X-MaxN).

The photoluminescence spectra were collected on a Spex 500 M monochromator (150 groves/mm grating blazed at 500 nm) equipped with either an Andor iDus (DV401A-BV) CCD or Andor InGaAs (DU490A-1.7) camera for capturing the visible and infrared range, respectively, and both cameras were cooled to -60 °C. A 462 nm blue laser diode was used to excite the X-ray induced Tm^{2+} ions. The Tm^{3+} luminescence was measured by a Fluoromax-3 fluorometer with excitation wavelengths of 348 nm (adding Thorlabs FGUV11S and FGL435 filters) and 458 nm (adding FES500 and Thorlabs FGL550S filters).

5.3 Characterization of nanocrystalline $BaLiF_3:Tm^{3+}$

5.3.1 Powder X-ray diffraction (XRD) pattern

The powder X-ray diffraction pattern (XRD) of nanocrystalline $BaLiF_3:Tm^{3+}$ prepared by ball milling is displayed in Figure 5.1.

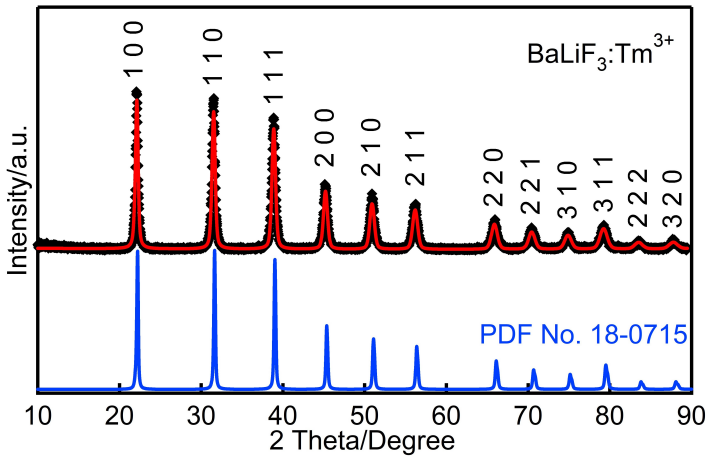

Figure 5.1: X-ray diffraction pattern of nanocrystalline $BaLiF_3:Tm^{3+}$. Experimental data and a Rietveld refinement (MAUD) are shown as black diamonds and a red solid line, respectively. For comparison, the standard X-ray diffraction data pattern of pure $BaLiF_3$ (PDF No. 18-0715) is shown as a blue solid line.

All the prominent peaks could be indexed to the cubic $BaLiF_3$ perovskite structure with the space group Pm-3m, which confirmed the purity of the as-prepared powder sample. A Rietveld refinement was performed by using MAUD 2.78 [170], yielding a unit cell parameter of, a = 4.009(3) Å, with weighted profile and expected R-factors, R_{wp} = 21% and R_{exp} =

14%, respectively, i.e. an acceptable goodness of fit, G = R_{wp}/R_{exp} = 1.5 [179]. A slight lattice expansion of 0.3% compared to the literature value, a = 3.996(3) Å [71], was observed. Surface tension and defects are the most likely reason for this expansion [184]. The Rietveld refinement indicated an average crystallite size of 46 ± 1 nm (isotropic approximation in the standard Delf model in MAUD).

5.3.2 Transmission electron microscopy

The morphology of the as-prepared $BaLiF_3:Tm^{3+}$ nanocrystals is illustrated by a typical TEM image in Figure 5.2a. A histogram of the crystallite sizes was obtained from an analysis of 683 particles in 19 TEM micrographs as shown in Figure 5.2b. An average crystallite size of ∼31 nm with a spread of about 10-80 nm was observed.

Elemental mapping (TEM-EDS) of nanocrystalline $BaLiF_3:Tm^{3+}$ demonstrated uniform distributions of Ba, F, Tm and Cl within the $BaLiF_3:Tm^{3+}$ nanocrystals as is shown in Figure 5.2c.

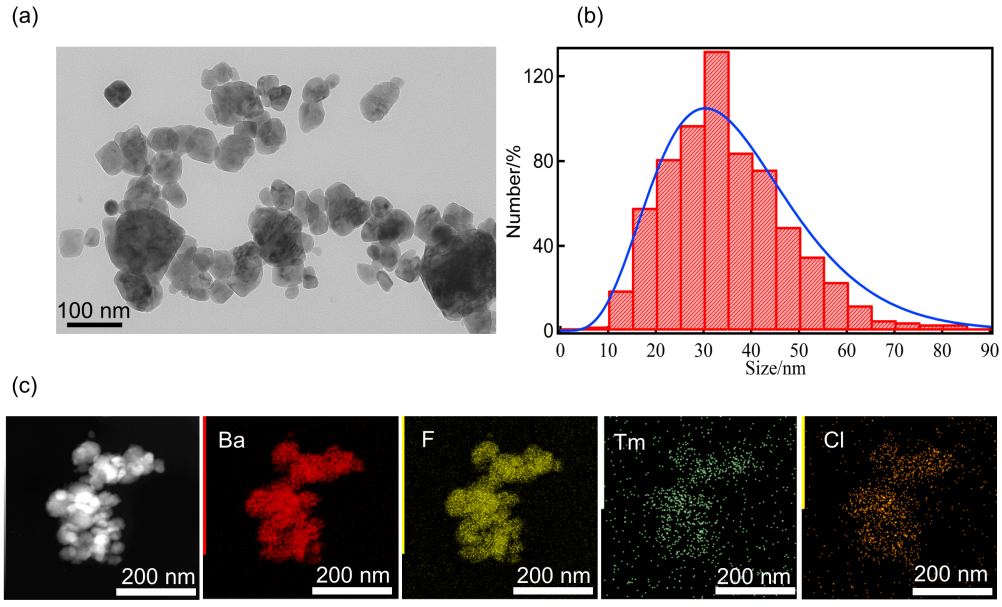

Figure 5.2: (a) Representative transmission electron microscope image of $BaLiF_3:Tm^{3+}$ prepared by ball milling along with (b) a histogram showing the crystallite size analysis of 683 particles. The blue solid line shows a gamma distribution function. (c) TEM-EDS (EDS, energy dispersive spectroscopy) elemental mapping images of Ba, F, Tm and Cl, respectively.

5.3.3 Scanning electron microscopy

Surface morphology of as-prepared ball-milled $BaLiF_3:Tm^{3+}$ was investigated using SEM imaging as illustrated in Figure 5.3a. In addition, the SEM-EDS maps (Figure 5.3b) demonstrate the existence and uniform distribution of detected elements such as Ba, F, Tm and Cl. TEM, SEM and TEM, and SEM based EDS analysis indicates no formation of an amorphous phase.

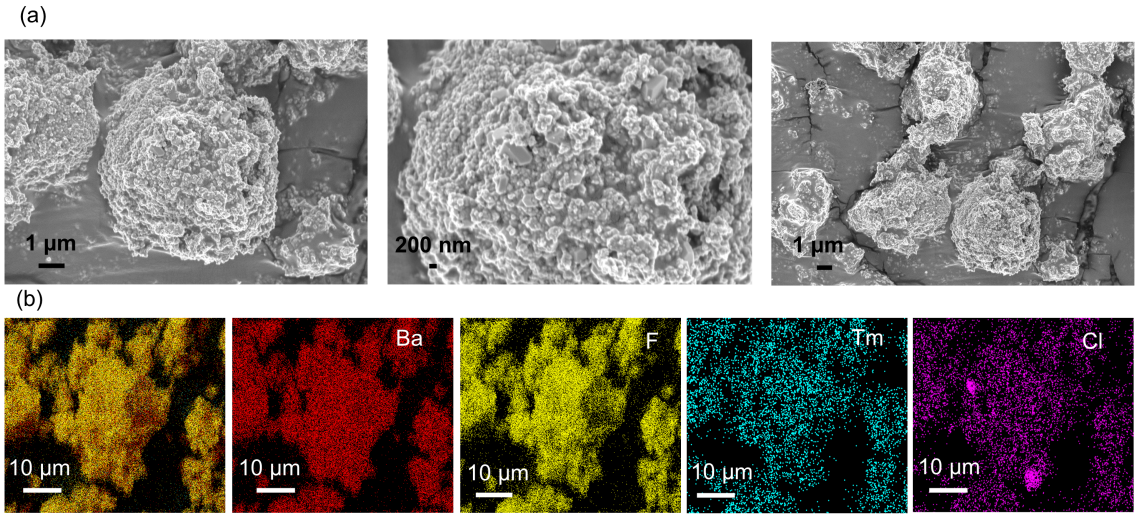

Figure 5.3: (a) SEM images of ball-milled $BaLiF_3:Tm^{3+}$ nanocrystals and (b) 2D SEM-EDS elemental maps of Ba, F, Tm and Cl.

5.4 Photoluminescence spectroscopy

5.4.1 X-ray sensitivity

The room temperature photoluminescence spectrum of nanocrystalline $BaLiF_3:Tm^{3+}$ was measured before (Figure 5.4a) and after X-irradiation (Figure 5.4b).

Before X-ray exposure, only Tm^{3+} peaks at 453 nm (Figure 5.4a), 643 nm and 650 nm (Figure 5.4a, inset) were measurable. The observed transitions could be attributed to the $^1D_2 \rightarrow {}^3F_4$, $^1G_4 \rightarrow {}^3F_4$ and $^1D_2 \rightarrow {}^3H_4$ transitions [137], respectively. After X-irradiation a relatively broad Tm^{2+} $^2F_{5/2} \rightarrow {}^2F_{7/2}$ peak at ~1136 nm appeared (Figure 5.4b).

Interestingly, no d-f luminescence in the visible range could be detected after X-irradiation in

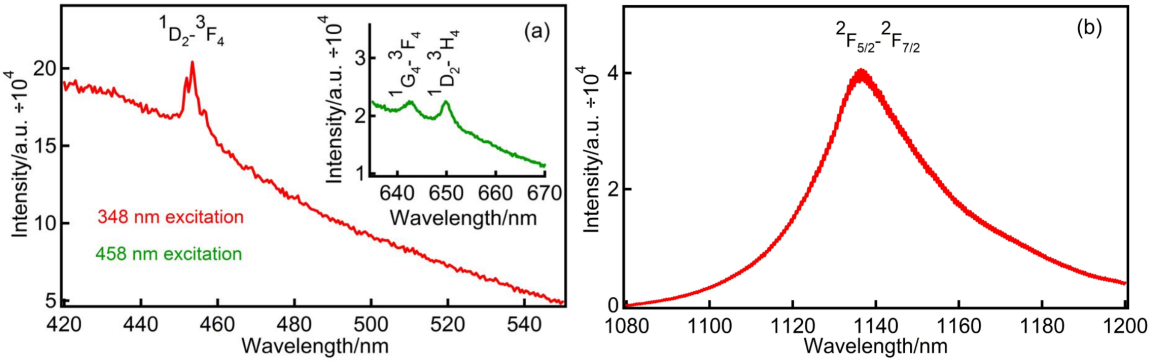

Figure 5.4: Room temperature photoluminescence spectra of nanocrystalline $BaLiF_3$:Tm^{3+} (a) before (red solid line - excited at 348 nm, green solid line - 458 nm excitation) and (b) after X-irradiation (108 Gy dose of Cu-Kα X-ray operated at 40 kV, 15 mA).

contrast to directly Tm^{2+} doped SrB_4O_7, $SrCl_2$, $BaZnCl_4$, $SrZnCl_4$ and $CsCaX_3$ (X = Cl, Br, I) [34, 185, 186].

5.4.2 Temperature dependent photoluminescence spectra

The temperature dependences of the photoluminescence spectra of Tm^{3+} and Tm^{2+} are shown in Figure 5.5a and b, respectively. The $^1D_2 \rightarrow {}^3H_4$ Tm^{3+} transition at 650 nm was the most pronounced transition in the low temperature photoluminescence spectrum of as-prepared $BaLiF_3$:Tm^{3+} (Figure 5.5a), however, with increasing temperature another Tm^{3+} transition was observed at 643 nm which can be assigned to the $^1G_4 \rightarrow {}^3F_4$ transition [140].

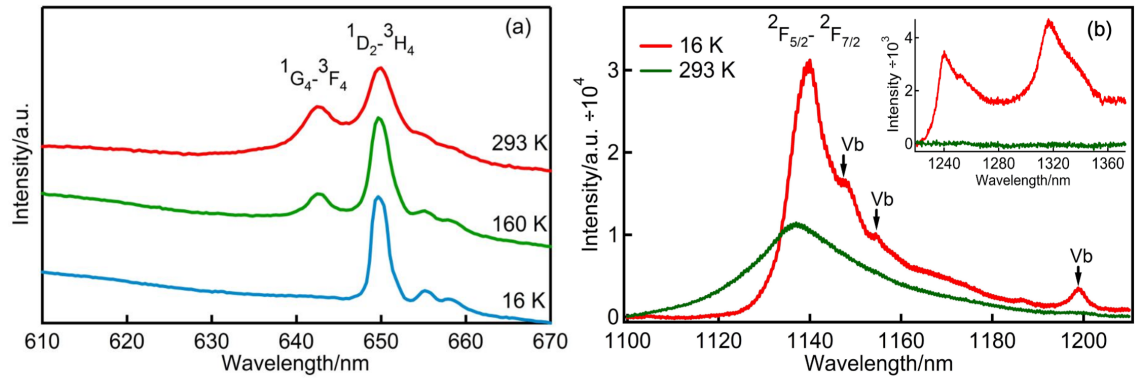

Figure 5.5: Temperature dependence of (a) trivalent and (b) divalent Tm in $BaLiF_3$:Tm^{3+}. The inset (b) shows the luminescence spectra of X-ray induced lattice defects at 1240 nm and 1317 nm. The sample was irradiated with 108 Gy of Cu-Kα X-ray (40 kV, 15 mA) for the spectra of Figure 5.5b. The spectra were excited at 462 nm.

In X-irradiated nanocrystalline $BaLiF_3$:Tm^{3+} (Figure 5.5b, vibrational sidelines are indicated by Vb), the broad Tm^{2+} $^2F_{5/2} \rightarrow {}^2F_{7/2}$ transition at ∼1136 nm became more intense and slightly narrower at low temperatures so that some vibronic sidelines (Vb) become partially resolved. In contrast to nanocrystalline BaFCl:Tm^{3+}, no splitting of the $^2F_{5/2} \rightarrow {}^2F_{7/2}$ transition was observed in $BaLiF_3$:Tm^{3+} [137]. However, two weak defect transitions at 1240 and 1317 nm appeared upon X-ray exposure which were only measurable at low temperature as is shown in the inset of Figure 5.5b. These two defects were also observed in X-irradiated pure $BaLiF_3$ (not shown here) which confirmed that they were intrinsic to the host lattice and are not due to Tm^{2+}. Specifically, both transitions are 10 times weaker than the Tm^{2+} transition (1136 nm) and likely due to X-ray induced F-centres. Also, their luminescence was subject to thermal quenching with increasing temperature (and fully quenched at 293 K). Recently several F-type centres have been identified in irradiated $BaLiF_3$ absorbing at 433, 565, 702 and 1068 nm [164].

5.4.3 X-ray dose dependency

To quantify the X-ray sensitivity of nanocrystalline $BaLiF_3$:Tm^{3+}, the reduction of Tm^{3+} ions to Tm^{2+} was measured by monitoring the photoluminescence intensity of the relatively broad Tm^{2+} $^2F_{5/2} \rightarrow {}^2F_{7/2}$ transition (∼1136 nm) as a function of accumulated X-ray dose. The X-ray dose dependence of the Tm^{2+} generation in nanocrystalline $BaLiF_3$:Tm^{3+} is summarized in Figure 5.6. The reduction mechanism of Tm^{3+} to Tm^{2+} ions depends on the electron and hole pairs created in the $BaLiF_3$ host upon X-irradiation. The X-ray generated electrons reduce Tm^{3+} ions to divalent Tm^{2+}. In $BaLiF_3$ the Tm-ions are located in the divalent Ba^{2+} sites and before X-irradiation Tm^{3+} ions are charge compensated by defects such as oxide impurities, interstitial F^- ions or Li^+ vacancies. The X-ray dose dependency of Tm^{2+} can be expected to follow first-order dispersive kinetics for which a bi-exponential function is a good approximation:

$$I_{Tm^{2+}} = A_1(1 - exp(-k_1 \times dose)) + A_2(1 - exp(-k_2 \times dose)) \tag{5.1}$$

In Equation 5.1, A_1 and A_2 are amplitudes and k_1 and k_2 are rate constants. The double exponential fit yielded dose-based reduction rate constants for Tm^{3+} of $k_1 = 0.019$ Gy^{-1} and $k_2 = 0.08$ Gy^{-1} and amplitudes $A_1 = 3$ and $A_2 = 2.6$.

The X-ray generated Tm^{2+} concentration, as measured by the $^2F_{5/2} \rightarrow {}^2F_{7/2}$ transition, reaches saturation at ~100 Gy. In comparison, saturation was only reached at >250 Gy in BaFCl:Tm^{3+} [140].

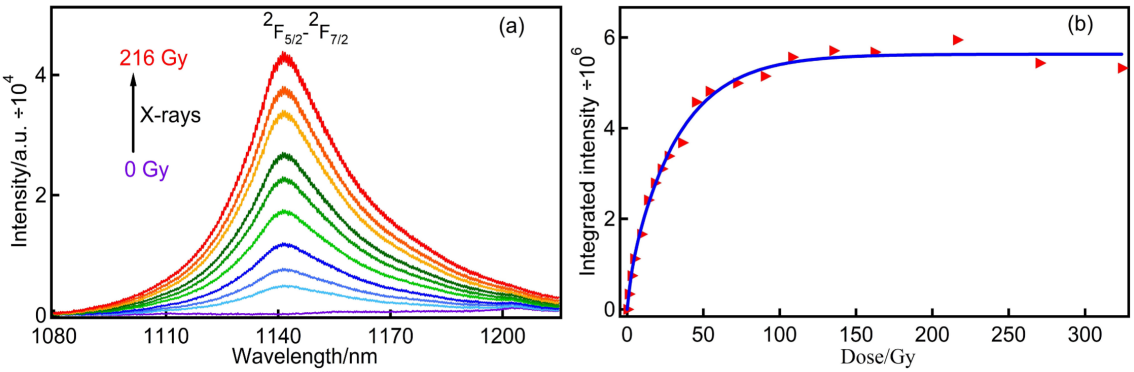

Figure 5.6: Room temperature photoluminescence spectra of X-irradiated nanocrystalline $BaLiF_3$:Tm^{3+} as a function of X-ray dose (0, 3, 5, 9, 14, 23, 36, 45, 90, 216 Gy). (b) Dependence of integrated photoluminescence intensities of the $^2F_{5/2} \rightarrow {}^2F_{7/2}$ Tm^{2+} transition at 1136 nm as a function of X-ray dose. The luminescence spectra were excited by a 462 nm laser diode with a power density of 0.24 W/cm^2. The blue solid line shows a double exponential fit Equation 5.1.

5.5 Photobleaching of X-ray induced Tm^{2+}

The bleaching/photoionization of Tm^{2+} ions with continuous blue light (462 nm laser diode) exposure is illustrated in Figure 5.7. In Figure 5.7a the photoluminescence spectrum is shown for a range of exposure periods to 462 nm light at a power density of 8 W/cm^2. The photobleaching of Tm^{2+} is shown for different excitation power densities in Figure 5.7b. The Tm^{2+} luminescence spectra were then integrated and normalized. The bleaching can be described by a standard gamma distribution (Equation 5.3) where the effective photoinduced electron transfer rate (k) is assumed to follow an exponential trend, as per Equation 5.2, as a function of the distance R between the electron and hole trap centres:

$$k = k_0 e^{-R/a_f} \tag{5.2}$$

Here, the rate constant k_0 is a measure of the photobleaching of Tm^{2+} for a specific excitation power density and a_f is the scaling parameter.

The photoreduction of Tm^{2+} luminescence can be modelled by [124]:

$$I_{Tm^{2+}}(t) = \int_{R_m}^{\infty} \frac{\beta^{\gamma}(R-R_m)^{(\gamma-1)} exp[-(R-R_m)\beta]}{\Gamma(\gamma)} exp(-k_0 e^{(-R/a_f)}t) dR \tag{5.3}$$

where, $I_{Tm^{2+}}$ is the normalized Tm^{2+} concentration, R_m is the radius for the excluded volume which is the nearest possible distance of oxide impurities and Tm^{2+} ions, and $\beta = (1$ Å$)^{-1}$. R, R_m and a_f in Equation 5.3 are all in units of Å. It is worth noting that the oxide impurity cannot be on a nearest neighbor F site as this would strongly stabilize the Tm^{3+} ions. In Equation 5.3, k_0 and γ determine the timescale and dispersion of the bleaching curve, respectively.

A global fit was performed for the data displayed in Figure 5.7b using Equation 5.3 with only k_0 as an individual fit parameter. The fit yielded $a_f = 0.86 \pm 0.11$ Å and $\gamma = 10 \pm 2$ when an excluded volume radius of $R_m = 7$ Å was chosen because the nearest neighbor distance ($\sqrt{2}$ a_0 [187] where a_0 is 3.996 Å) is 5.65 Å. The fitted value obtained for γ indicates that the Tm^{2+} ion is separated from the hole traps by 17 Å. The interatomic distance 17 Å was determined by analyzing the Gamma distribution function on the basis of the results obtained from the global fits (Figure 5.7b). It is important to note that these parameters should not be overinterpreted as they are not fully independent.

The power dependence of the rate constant k_0 shown in Figure 5.7c can be described by a simple power law, given in Equation 5.4, to determine whether the ionization mechanism follows a single or two-photon process:

$$k = A \times p^x \tag{5.4}$$

In Equation 5.4, p denotes the power density of the bleaching light and x is the slope. The global fit yields a power dependence of $x = 0.8 \pm 0.1$, indicating that a single photon ionization process takes part in nanocrystalline $BaLiF_3$:Tm^{3+}.

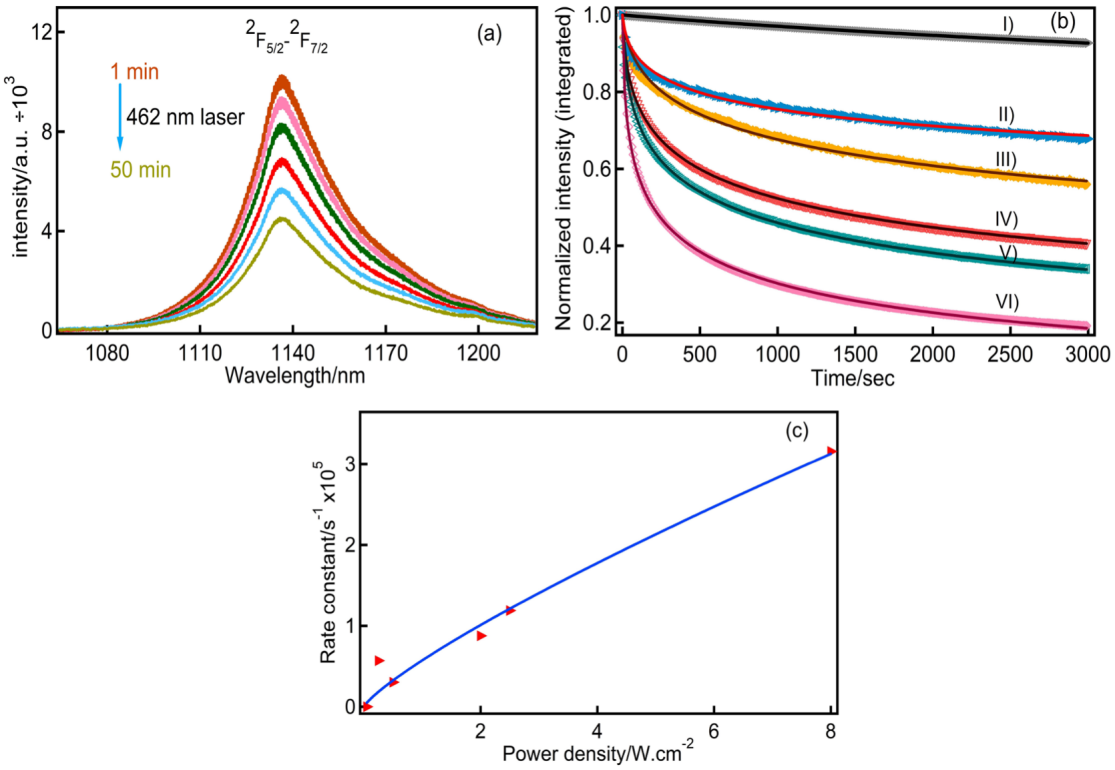

Figure 5.7: (a) Room temperature photoluminescence spectra of Tm^{2+} ($^2F_{5/2} \rightarrow {}^2F_{7/2}$ transition at 1136 nm) in nanocrystalline $BaLiF_3$:Tm^{3+} upon photobleaching with 462 nm laser light over 1, 2, 5, 11, 23, 50 min time periods. (b) Power density and time dependence of the integrated and normalized photoluminescence intensity of the Tm^{2+} luminescence at 1136 nm. A 462 nm laser light with power densities (I) 0.05, (II) 0.25, (III) 0.5, (IV) 2, (V) 3 and (VI) 8 W/cm^2 was used to excite the $^2F_{5/2} \rightarrow {}^2F_{7/2}$ transition. The samples were initially exposed to 108 Gy X-ray. The solid lines are global fits. (c) Rate constant k_0 as a function of power density.

5.6 Stability of X-ray induced Tm^{2+}

The stability of Tm^{2+} ions in nanocrystalline $BaLiF_3$:Tm^{3+} was tested under two conditions. For this experiment, X-irradiated samples were kept in the dark or alternatively exposed to sunlight for several hours, and the broad Tm^{2+} ($^2F_{5/2} \rightarrow {}^2F_{7/2}$, ~1136 nm) luminescence was

periodically measured (Figure 5.8) with short excitation times of 10 s to minimize bleaching by the readout. It was observed that the Tm^{2+} ions are relatively stable in the dark but seem to be photoionized to Tm^{3+} rapidly upon exposure to sunlight.

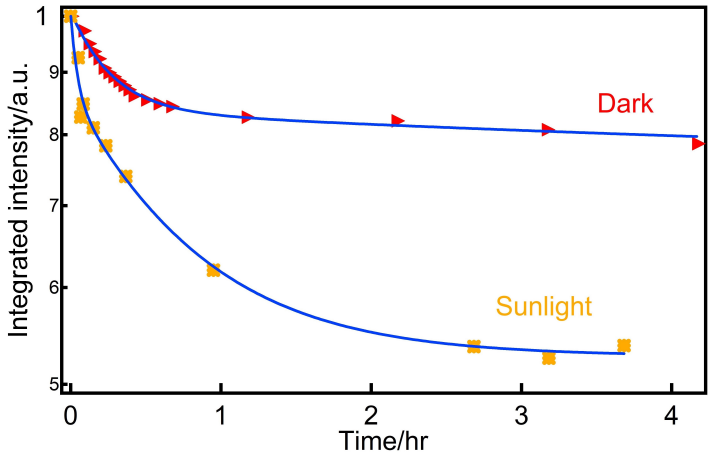

Figure 5.8: Stability of Tm^{2+} in X-irradiated nanocrystalline $BaLiF_3$:Tm^{3+} in the dark (red data points) and in sunlight (yellow data points). Blue solid lines represent double exponential fits. A 462 nm (0.3 Wcm^{-2}) laser light was used to excite the photoluminescence of Tm^{2+} at ~1136 nm. Both samples were initially exposed to an X-ray dose of 108 Gy.

5.7 Storage capability of rare-earth ions (Eu^{3+}, Sm^{3+}, Tm^{3+}) activated $BaLiF_3$

The X-ray sensitivities of $BaLiF_3$:Tm^{3+}, $BaLiF_3$:Eu^{3+} and $BaLiF_3$:Sm^{3+} nanocrystals were compared as is summarized in Figure 5.9.

Figure 5.9a illustrates the photoluminescence spectra of the divalent rare earth ions in ball-milled $BaLiF_3$:Eu^{3+}, $BaLiF_3$:Sm^{3+} and $BaLiF_3$:Tm^{3+} after exposure to X-irradiation (6 Gy Cu-Kα, 40 kV, 15 mA) in the range of the Eu^{2+}, Sm^{2+} and Tm^{2+} luminescence transitions at 361 nm ($^6P_{7/2} \rightarrow {}^8S_{7/2}$), 422 nm ($4f^65d \rightarrow {}^8S_{7/2}(4f^7)$), 694 nm ($^5D_0 \rightarrow {}^7F_1$), and 1136 nm ($^2F_{5/2} \rightarrow {}^2F_{7/2}$), respectively. The build-up of the integrated photoluminescence intensity of the divalent ions (Eu^{2+}, Sm^{2+} and Tm^{2+}) upon cumulative X-irradiation is summarized in Figure 5.9b.

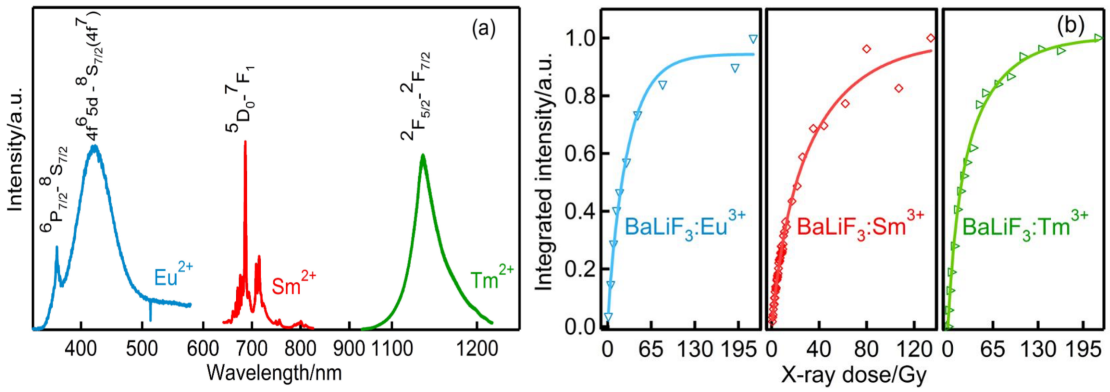

Figure 5.9: (a) Photoluminescence spectra of X-ray induced Eu^{2+} in $BaLiF_3$:Eu^{3+} (blue trace), Sm^{2+} in $BaLiF_3$:Sm^{3+} (red trace, ref. [188]) and Tm^{2+} in $BaLiF_3$:Tm^{3+} (green). (b) Dependence of the integrated luminescence of Eu^{2+} ($4f^6 5d \rightarrow {}^8S_{7/2}$ ($4f^7$)) at 422 nm (blue markers), Sm^{2+} ($^5D_0 \rightarrow {}^7F_1$) at 694 nm (red markers, ref. [188]) and Tm^{2+} ($^2F_{5/2} \rightarrow {}^2F_{7/2}$) at 1136 nm (green markers), as a function of X-ray dose. Solid lines represent double exponential fits. The Eu^{2+} luminescence in $BaLiF_3$:Eu^{3+} was excited by a 262 nm LED whilst the Sm^{2+} and Tm^{2+} emission in $BaLiF_3$:Sm^{3+} and $BaLiF_3$:Tm^{3+}, respectively, were excited by a 462 nm laser diode.

The double exponential fit parameters obtained from the data presented in Figure 5.9b are summarized in **Table 5.1**. It appears that the reduction rates (k_1 and k_2) vary among the samples, with an increasing reduction rate in the order of $BaLiF_3$:Tm^{3+} < $BaLiF_3$:Sm^{3+} and << Ba-LiF_3:Eu^{3+}. This trend is in accord with the standard reduction potentials: $Tm^{3+} \rightarrow Tm^{2+}$ (∼-2.3 V), $Sm^{3+} \rightarrow Sm^{2+}$ (∼-1.6 V) and $Eu^{3+} \rightarrow Eu^{2+}$ (∼-0.3 V) [60, 61]. This result clearly indicates the potential of the $BaLiF_3$ host matrix for real world applications such as for storage phosphors. Additionally, the X-ray sensitivity of rare-earth ions incorporated $BaLiF_3$ is significant for X-ray dosimetry.

Table 5.1: Rate constants derived from the bi-exponential fit Equation 5.1 for the generation of divalent rare earth ions (Eu^{2+}, Sm^{2+}, Tm^{2+}) upon X-ray irradiation.

System	**Emission wavelength** /nm	$\mathbf{k_1}$ /Gy^{-1}	$\mathbf{k_2}$ /Gy^{-1}
$BaLiF_3$:Eu^{3+}	422	0.033 (±0.004)	0.299 (±0.584)
$BaLiF_3$:Sm^{3+}	694	0.023 (±0.009)	0.094 (±0.054)
$BaLiF_3$:Tm^{3+}	1136	0.019 (±0.002)	0.076 (±0.007)

5.8 Summary

In summary, a mechanochemical synthesis approach for nanocrystalline $BaLiF_3$:Tm^{3+} was demonstrated and its X-ray sensitivity was examined by comparing photoluminescence spectra before and after X-irradiation. In particular, a detailed demonstration of the infrared Tm^{2+} emission in $BaLiF_3$:Tm^{3+} by X-ray exposure was presented. After X-ray exposure, Tm^{2+} ions were observed at 1136 nm ($^2F_{5/2} \rightarrow {}^2F_{7/2}$ transition). However, no visible Tm^{2+} emission could be detected in contrast to earlier reports on systems such as $CsCaCl_3$, $CsCaBr_3$ and $CsCaI_3$ [34, 189], where the divalent Tm was incorporated by direct chemical methods. The dispersion of Tm^{2+} photobleaching upon continuous laser illumination was measured and explained by dispersive kinetics assuming a standard gamma distribution function for the Tm-hole trap centre distribution. It appeared that the Tm^{2+} ions are separated from the hole traps by an interionic spacing of 17 Å. The power dependence of Tm^{2+} bleaching implied a single photoionization mechanism. These results signify that the infrared emission of Tm^{2+} in nanocrystalline $BaLiF_3$ may be used in solar radiation converter/concentrator applications, although for such an application the Tm^{2+} should be directly doped by chemical methods. Additionally, the response of $BaLiF_3$:Eu^{3+}, $BaLiF_3$:Sm^{3+} and $BaLiF_3$:Tm^{3+} to X-irradiation was presented and compared. It was found that upon X-irradiation trivalent ions (Eu^{3+}, Sm^{3+}, Tm^{3+}) can be efficiently reduced to their divalent state (Eu^{2+}, Sm^{2+}, Tm^{2+}). This is significant, as it shows that different rare-earth ions (Eu, Sm and Tm) can be readily incorporated into the $BaLiF_3$ host by a facile mechanochemical method, and a broad spectral emission (from infrared to UV) can be achieved by an appropriate selection of the activator ion. These results advance the current understanding of the rare-earth ion doped $BaLiF_3$ activator-host system and demonstrate their potential as X-ray storage phosphors.

Chapter 6

Upconversion luminescence of Yb^{3+} and Er^{3+} Co-doped $BaLiF_3$ Nanocrystals

★★★*The work related to this chapter has been peer-reviewed and published in ACS Applied Nano Materials. Dr. Nicolas Riesen is acknowledged for his support with the transmission and scanning electron microscopy, and TEM, SEM-based elemental mapping. The published article can be accessed as:*

Chowdhury, N.; Riesen, N.; Riesen, H. Yb^{3+} and Er^{3+} Codoped $BaLiF_3$ Nanocrystals for X-ray Dosimetry and Imaging by Upconversion Luminescence. ACS Applied Nano Materials, 2021, 4(7), 6659-6667.★★★

6.1 Introduction

Lanthanide ion doped nanocrystals exhibit attractive upconversion luminescence (UCL) properties and have found potential applications in 3D displays, photocatalysis, infrared quantum counting and as solid-state laser materials [190–192]. To date, hexagonal $NaYF_4$ is the best performing fluoride-based upconversion host for green and blue emission [41, 193–197]. The performance of upconversion materials strongly depend on the crystal structure of the host matrix [198]. In this context, $BaLiF_3$ has been investigated as a potential upconversion host material. For example, microcrystalline $BaLiF_3$ doped with Yb^{3+}, Er^{3+}/ Ho^{3+} (crystal size ~2-4 μm) were prepared by a surfactant-assisted hydrothermal-microemulsion method, and they showed stable red upconversion luminescence [36]. However, for their application in X-ray

imaging and radiation monitoring system, systematic investigation of their X-ray storage capability and mechanism is crucial. Another important aspect of phosphor material is that their sensitivity is dependent on crystallite sizes. For example, it was reported that nanophosphor (∼200 nm) exhibited 500,000 times higher X-ray sensitivity in comparison with microcrystalline materials [134]. Therefore, it is also important to explore the upconversion and X-ray storage properties of $BaLiF_3$:Yb^{3+}, Er^{3+} phosphors prepared in nanocrystalline form.

This chapter presents a successful preparation of nanocrystalline $BaLiF_3$:Yb^{3+}, Er^{3+} that shows infrared-to-visible upconversion luminescence. The effect of X-irradiation on the upconversion luminescence is also investigated. This chapter also presents 2D X-ray imaging of $BaLiF_3$:Yb^{3+}, Er^{3+} nanophosphor by upconversion luminescence.

6.2 Experimental details

6.2.1 Preparation Process

$BaLiF_3$ co-doped with Yb^{3+} and Er^{3+}

BaF_2 was synthesized by co-precipitation of $Ba(NO_3)_2$ (May and Baker) and NH_4F (Sigma Aldrich). Nanocrystalline $BaLiF_3$:Yb^{3+}, Er^{3+} was prepared by ball milling BaF_2, LiF (Ajax), YbF_3 (Sigma Aldrich) and $ErCl_3.6H_2O$ (Sigma Aldrich) for 2, 3 and 4, hours. In brief, to prepare $Ba_{0.99-x}Yb_xEr_{0.01}LiF_{3+x}Cl_{0.03}$ nanoparticles, where x = 0.01, 0.05 and 0.1; (0.99-x) mmol BaF_2, x mmol YbF_3 (x = 0.01, 0.05 and 0.1), 0.01 mmol $ErCl_3{\cdot}6H_2O$ and 1 mmol LiF were premixed and ground together by a mortar and pestle before being transferred into a 10 mL zirconia lined jar with two 12 mm zirconia balls. The milling process was performed on a Retsch Mixer Mill 200 at a frequency of 20 Hz. Post-annealing was conducted in a muffle furnace (Labec, CEMLS-SD) in air.

$NaYF_4$ co-doped with Yb^{3+} and Er^{3+}

For comparison of the UCL efficiencies, hexagonal $NaYF_4$ co-doped with 10% Yb^{3+} and 1% Er^{3+} was also prepared by ball milling a mixture of 1 mmol NaF, 0.89 mmol YF_3, 0.1 mmol YbF_3 and 0.01 mmol $ErCl_3{\cdot}6H_2O$ for 4 h at 20 Hz [140]. The pure hexagonal phase was

verified by powder XRD. For comparison, an Er^{3+} doped YbF_3 (0.4 g of YbF_3 and 0.004 mg of $ErCl_3{\cdot}6H_2O$) sample was also prepared by ball milling for 4 h.

$BaLiF_3$:Yb^{3+}, Er^{3+} coated photographic film

For the imaging experiments, some imaging plates (films) were prepared by depositing a suspension of the phosphor ($BaLiF_3$:5% Yb^{3+}, 1% Er^{3+}) with 5 wt-% of dissolved binder (Kraton stabilized with STANN in toluene: butyl acetate: methylcyclohexane 9:6:5), on a poly(vinyl acetate) substrate of 100 μm thickness with the mixture being spread by a doctor's blade. The resulting coating had a thickness of 20 μm.

6.2.2 Structural property of $BaLiF_3$:Yb^{3+}, Er^{3+}

The phase purity of samples was characterized by X-ray diffraction (XRD) employing a Rigaku Miniflex 600 benchtop powder XRD with a Cu-Kα (λ = 0.154 nm) X-ray tube, operated at 40 kV, 15 mA.

Scanning electron microscopy (SEM) and Energy Dispersive X-ray (EDS) mapping were performed with a Zeiss Crossbeam 540 with SDD EDS (Oxford Instruments X-MaxN). Transmission Electron Microscopy (TEM) and EDS mapping were also performed by utilizing a JEOL JEM-2100F Field Emission TEM. The TEM analysis was further verified with a FEI Tecnai G2 Spirit TEM.

6.2.3 Upconversion and photoluminescence spectroscopy

The upconversion luminescence and photoluminescence spectra were measured using a Spex 500 M monochromator equipped with an Andor iDus Model DV401A-BV CCD camera. A current and temperature controlled near-infrared laser diode (Thorlabs L980P100A controlled by a Thorlabs LDC 500 and Thorlabs TEC 2000 current and temperature controller) focused with a maximum power density of 65 $W.cm^{-2}$ was used to excite the upconversion luminescence at 980 nm. To observe the effect of X-ray exposure, samples were irradiated in the Rigaku Miniflex 600 benchtop powder X-ray diffractometer. The X-ray dose was cross calibrated against a Sirona HELIODENT Plus dental X-ray.

6.2.4 X-ray imaging by upconversion luminescence

For the read-out of imaging plates in 2D, a modified "flying spot" setup built in the laboratory was used. Instead of scanning the laser spot across the imaging plate, the latter was translated in x and y. This was undertaken by two motorized translation stages (Thorlabs MTS50-Z8, 50 mm travel, controlled by Thorlabs T-cube TDC001 controllers) that were mounted in XY configuration. The UCL was excited by focussed 980 nm laser light (1.6 mW) from the laser diode described above. The collimated UCL signal was then passed through a 700 nm short pass filter (Thorlabs FES700) and measured by a miniature photon counting head (Hamamatsu H7467-01). The 2D reader setup was enclosed in a black box and was computer controlled.

6.3 Characterization of $BaLiF_3$:Yb^{3+}, Er^{3+} nanophosphor

6.3.1 Powder X-ray diffraction pattern

The powder X-ray diffraction (XRD) patterns of $BaLiF_3$ doped with 1% of YbF_3 and $ErCl_3$ prepared by ball milling for 2, 3 and 4 h are illustrated in Figure 6.1a. In Figure 6.1b, the XRD patterns for $BaLiF_3$ doped with 1% $ErCl_3$ and three YbF_3 concentrations (1, 5 and 10%) are shown. Finally, XRD patterns of $BaLiF_3$ doped with 1% YbF_3 and $ErCl_3$ annealed at three temperatures are displayed in Figure 6.1c.

The prominent X-ray diffraction peaks in all of the patterns displayed in Figure 6.1, can be indexed to the pure cubic $BaLiF_3$ structure with the space group Pm-3m.

After 2 hours of milling, residual peaks from BaF_2 and YbF_3 are still visible in Figure 6.1a, whereas a more complete nanocrystalline $BaLiF_3$:Yb^{3+}, Er^{3+} phase formation (∼100%) is observed after 3 hours. **Table 6.1** summarizes the X-ray diffraction parameters of the Rietveld refinements (using the MAUD [170] software) that are illustrated in Figure 6.1.

The average crystallite size was determined with the default MAUD "Delf" size-strain model in the isotropic approximation cite196. As shown in **Table 6.1**a, the average crystallite size decreases from 38 ± 1 nm (2 h) to 32 ± 1 nm (4 h) with increasing ball-milling time. Interestingly, a more drastic reduction of the average crystallite size from 32 ± 1 nm to 21 ± 1 nm

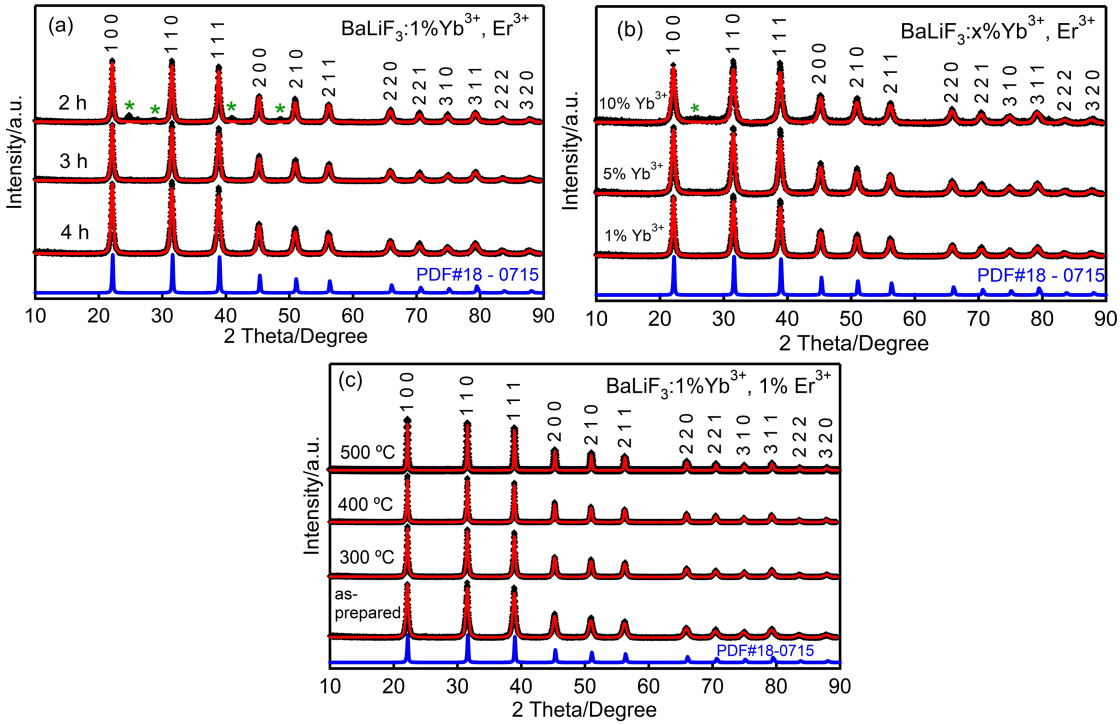

Figure 6.1: Powder XRD patterns of (a) $BaLiF_3$:1% Yb^{3+}, 1% Er^{3+} nanoparticles prepared by ball milling for 2, 3 and 4 h respectively (residual BaF_2 and YbF_3 peaks are indicated by green asterisks), (b) $BaLiF_3$:1% Er^{3+} with different concentrations of Yb^{3+} (1, 5, 10%) ball milled for 4 h, (c) as-prepared and annealed (300, 400 and 500 °C) $BaLiF_3$:1% Yb^{3+}, 1% Er^{3+} samples. Experimental data and Rietveld refinements are shown as black diamonds and red solid lines, respectively. Diffraction peaks from residual reagents are indicated by the green asterisk (∗). For comparison, the standard $BaLiF_3$ data (PDF #18-0715) is also shown (blue line).

is observed when the Yb concentration is increased from 1 to 10% (see **Table 6.1**(b)). This is most likely due to the disruption of the crystal lattice formation by the trivalent dopant. It appears (see also below) that relatively large concentrations of the trivalent Yb^{3+} can be built into the crystal lattice. Charge compensation is achieved by interstitial F^- ions but some compensation by Li^+ vacancies is also possible.

In summary, the average crystallite size of as-prepared $BaLiF_3$:Yb^{3+}, Er^{3+} decreases with increasing ball-milling time and Yb^{3+} concentration. In contrast, as shown in **Table 6.1**(c), the average crystallite sizes of $BaLiF_3$:1% Yb^{3+}, 1% Er^{3+} samples annealed at 300, 400 and 500 °C are 50 ± 1, 88 ± 1 and 153 ± 3 nm, respectively, i.e., the average crystallite size increases with annealing temperature, as expected.

Table 6.1: Summary of Rietveld refinement parameters as obtained from MAUD where R_{wp} and R_{exp} are the weighted-profile R-factor and expected R-factor, respectively. $G = R_{wp}/R_{exp}$ determines the goodness of fit, with $G < 2$ indicating an acceptable refinement.

(a) Ball milling time					
$BaLiF_3$:1% Yb^{3+}, 1% Er^{3+}					
Ball milling time /h	Lattice parameter /Å	Average crystallite size /nm	R_{wp}%	R_{exp}%	G%
2	4.008 (3)	38 ± 1	24.9	13.6	1.8
3	4.008 (3)	35 ± 1	19.2	13.2	1.5
4	4.009 (3)	32 ± 1	18.9	13.4	1.4

(b) Concentration of Yb^{3+}						
$BaLiF_3$:x% Yb^{3+}, 1% Er^{3+}						
Ball milling time/h	% of Yb^{3+}	Lattice parameter/Å	Average crystallite size/nm	R_{wp}%	R_{exp}%	G%
4	1	4.009 (3)	32 ± 1	18.9	13.4	1.4
4	5	4.008 (4)	25 ± 1	18.5	12.5	1.5
4	10	4.01 (6)	21 ± 1	22.3	11.9	1.9

(c) Annealing temperature					
$BaLiF_3$:1% Yb^{3+}, 1% Er^{3+}					
Annealing temperature/°C	Lattice parameter /Å	Average crystallite size /nm	R_{wp}%	R_{exp}%	G%
As-prepared	4.008 (3)	35 ± 1	19.2	13.2	1.5
300	4.006 (2)	50 ± 1	18.5	13.1	1.4
400	4.006 (2)	88 ± 1	20.2	14.2	1.4
500	4.003 (1)	154 ± 3	20.9	13.2	1.6

6.3.2 TEM and SEM micrograph analysis

To reveal the actual size and morphology of the individual crystals, typical TEM micrographs and histograms showing corresponding particle size distributions of ball-milled samples with 1% and 10% YbF_3 concentrations before and after annealing are shown in Figure 6.2.

From the histograms it follows that the average crystallite sizes of as-synthesized nanocrystals containing 1 and 10% YbF_3 is 26 ± 6 nm (Figure 6.2a) and 16 ± 3 nm (Figure 6.2c), respectively, in reasonable agreement with the XRD results. The average crystallite size increases upon annealing to 190 ± 4 nm (Figure 6.2b) and 121 ± 5 nm (Figure 6.2d), respectively, in

$BaLiF_3$:1% Yb^{3+}, 1% Er^{3+} and $BaLiF_3$:10% Yb^{3+}, 1% Er^{3+} samples. This result shows again that with increasing concentrations of the trivalent dopant YbF_3 in $BaLiF_3$, a reduction of the average crystallite size occurs in accord with the powder X-ray diffraction results. Importantly, EDS maps of $BaLiF_3$:10% Yb^{3+}, 1% Er^{3+} (as-prepared and annealed) are also shown in Figure 6.2, confirming uniform distributions of Ba, F, Yb, Er and Cl within the nanocrystals.

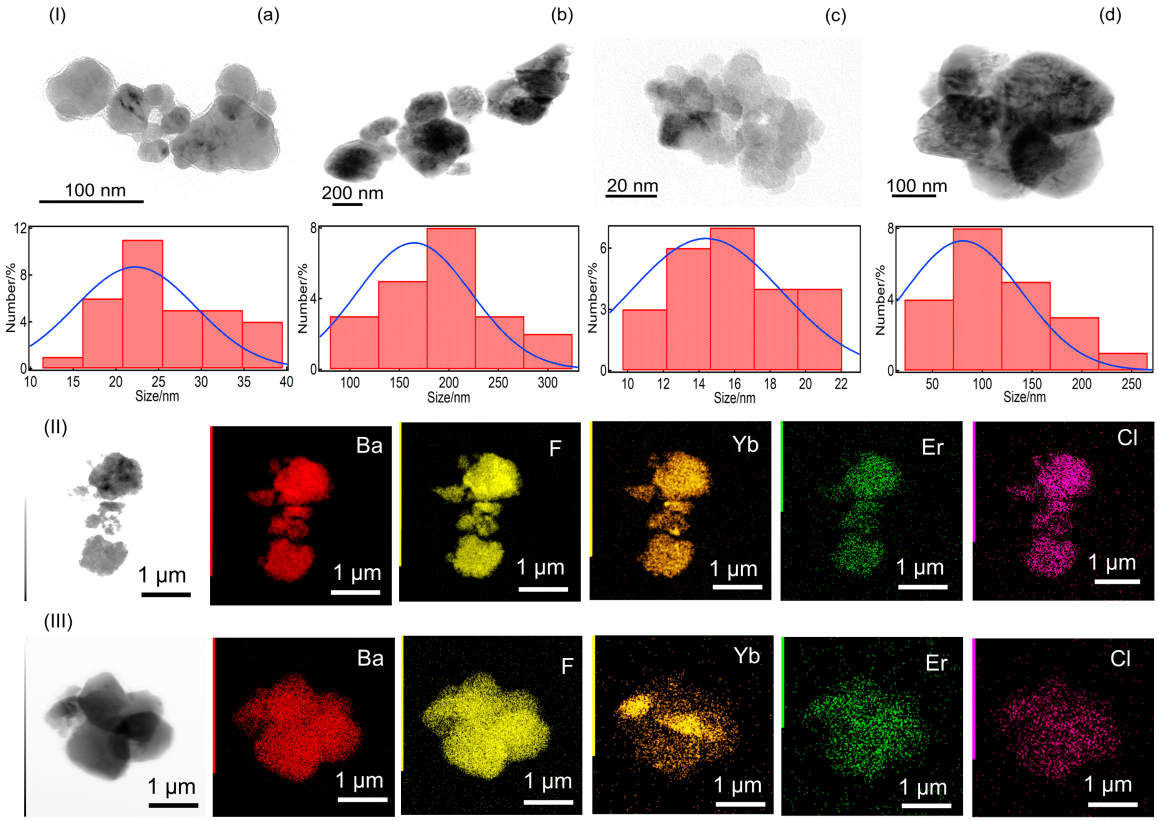

Figure 6.2: Representative TEM images (I) of (a) as-prepared $BaLiF_3$:1% Yb^{3+},1% Er^{3+}, (b) annealed $BaLiF_3$:1% Yb^{3+},1% Er^{3+} at 500 °C, (c) as-prepared $BaLiF_3$:10% Yb^{3+}, 1% Er^{3+}, and (d) annealed $BaLiF_3$:10% Yb^{3+}, 1% Er^{3+} at 500 °C. Corresponding histograms of particle size distribution (from six TEM images) are shown in the lower panel of each TEM image. 2D EDS maps of $BaLiF_3$:10% Yb^{3+}, 1% Er^{3+} before (II) and after (III) annealing are shown in the bottom panels.

In addition, SEM micrographs of $BaLiF_3$:1% Yb^{3+}, 1% Er^{3+} and $BaLiF_3$:10% Yb^{3+}, 1% Er^{3+} (as-prepared and annealed) are shown in Figure 6.3.

It appears that in both cases (i.e. samples containing 1 and 10% YbF_3) the annealing step

increases the average crystallite/particle sizes, which is in agreement with the XRD results discussed above. 2D EDS elemental maps of as-prepared (Figure 6.3, panel II) and annealed (Figure 6.3, panel III) $BaLiF_3$:10% Yb^{3+}, 1% Er^{3+} are also shown in Figure 6.3, and these maps confirm uniform distributions of the detected elements Ba, F, Yb, Er and Cl with measured 67, 23, 9, 0.1 and 0.1 wt-%, respectively (Li is too light to be detected by the SEM-EDS). In comparison, the expected weight percentages for Ba, F, Yb, Er and Cl in $Ba_{0.89}Yb_{0.1}Er_{0.01}LiF_{3.1}Cl_{0.03}$ (corrected for the non-detectability of Li) are 61, 29, 8.6, 0.8 and 0.5 wt-%, respectively. Barium strongly absorbs in the X-ray region and hence, SEM-EDS and TEM-EDS results are semiquantitative at best for the present compound. We note here that the weight percentages are a priori defined as the phosphor is made by ball milling.

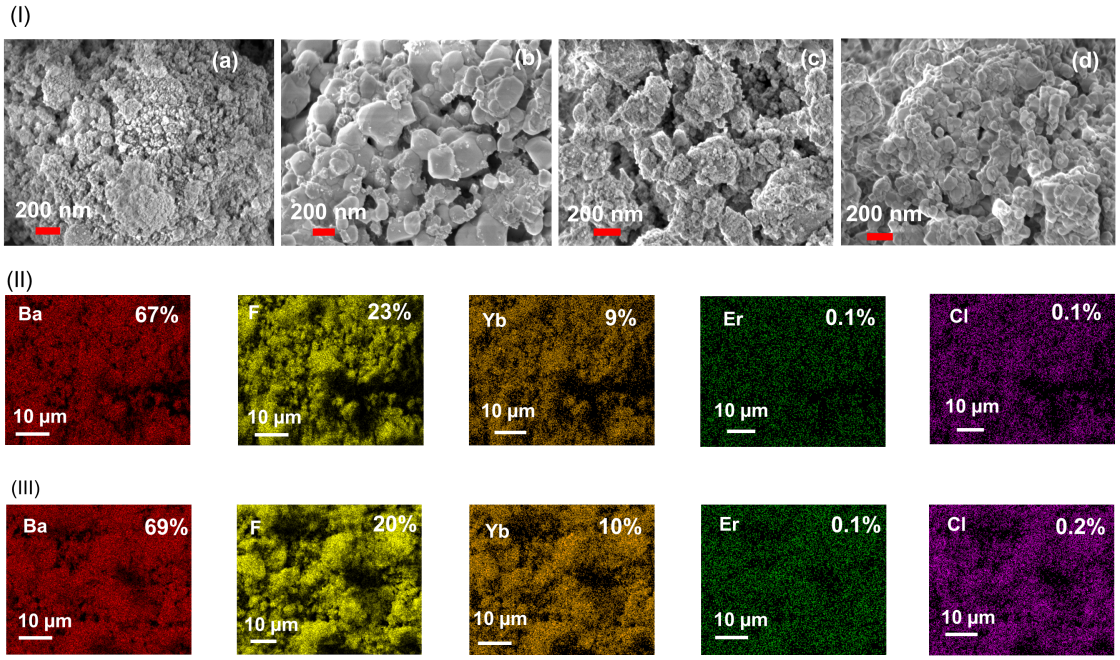

Figure 6.3: SEM image (I) of (a) as-prepared $BaLiF_3$:1% Yb^{3+}, 1% Er^{3+}, (b) $BaLiF_3$:1% Yb^{3+}, 1% Er^{3+} annealed at 500 °C for 1 hour, (c) as-prepared $BaLiF_3$:10% Yb^{3+}, 1% Er^{3+}, (d) $BaLiF_3$:10% Yb^{3+}, 1% Er^{3+} annealed at 500 °C for 1 hour. Elemental 2D EDS maps of $BaLiF_3$:10% Yb^{3+}, 1% Er^{3+} before (II) and after annealing (III). The weight-% is indicated.

6.3.3 Upconversion luminescence

The room temperature upconversion spectrum of nanocrystalline $BaLiF_3$:1% Yb^{3+}, 1% Er^{3+} excited by a temperature and current-controlled 980 nm laser diode is given in Figure 6.4a. Three well-separated upconversion bands were identified at 521, 540 and 650 nm, with the

latter showing the strongest upconversion luminescence under 980 nm laser excitation. These transitions can be assigned to $^2H_{11/2} \rightarrow {}^4I_{15/2}$, $^4S_{3/2} \rightarrow {}^4I_{15/2}$ and $^4F_{9/2} \rightarrow {}^4I_{15/2}$ intraconfigurational f-f electronic transitions of Er^{3+} ions, respectively.

A logarithmic plot of integrated intensities of these three bands (521, 540, and 650 nm) as a function of the excitation power is shown in Figure 6.4b. It is well documented [199] that the upconversion luminescence intensity (I_{UC}) is directly proportional to the excitation power (P) as follows,

$$I_{UC} \propto P^n \tag{6.1}$$

where n is the number of excitation photons required to generate upconversion luminescence. The value of n can be readily determined from the logarithmic plot of the data.

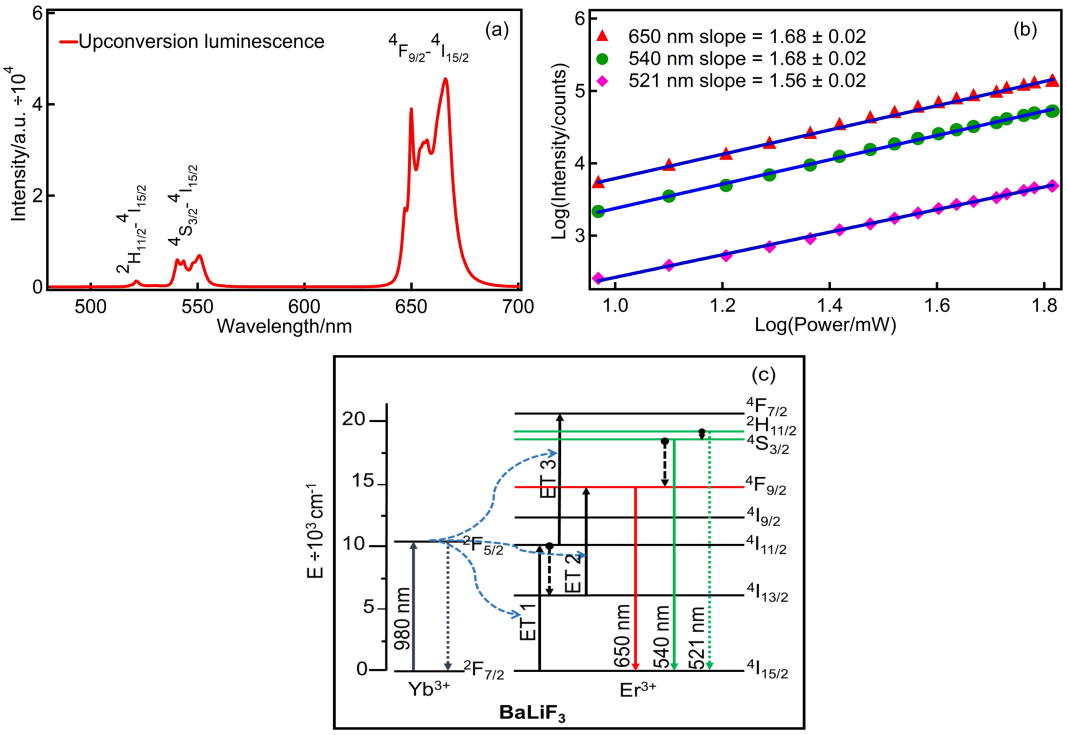

Figure 6.4: (a) Upconversion luminescence spectrum of nanocrystalline $BaLiF_3$:1% Yb^{3+}, 1% Er^{3+} (annealed at 400 °C) excited by a 980 nm laser diode. (b) excitation power dependence of the upconversion luminescence at 521, 540 and 650 nm. Solid lines are fits to Equation 6.1. (c) Energy-level diagram of Yb^{3+} and Er^{3+} and a possible mechanism for upconversion emission based on energy transfer (ET).

From the data presented in Figure 6.4b, n values of 1.56 ± 0.02, 1.68 ± 0.02 and 1.68 ± 0.02 were determined for the three upconversion luminescence bands $^2H_{11/2} \rightarrow {}^4I_{15/2}$ (521 nm),

$^4S_{3/2} \rightarrow {}^4I_{15/2}$ (540 nm) and $^4F_{9/2} \rightarrow {}^4I_{15/2}$ (650 nm), respectively. These values indicate that the upconversion mechanism in nanocrystalline $BaLiF_3:Yb^{3+}$, Er^{3+} is based on a two-photon process, a result that is in accord with the literature [36]. The energy-transfer (ET) based mechanism is illustrated in Figure 6.4c.

Figure 6.5a shows the upconversion spectra of as-prepared $BaLiF_3$:1% Yb^{3+}, 1% Er^{3+} for different ball milling times. As can be seen in Figure 6.5b, the upconversion luminescence gradually decreases with longer ball milling time. This is most likely due to the incorporation of more defects in the host lattice upon prolonged milling. Importantly, a longer milling process (3 and 4 h) reduces the average crystallite size (see **Table 6.1**a) and hence leads to a larger surface to volume ratio, i.e. a closer proximity of the optical centres to the surface defects.

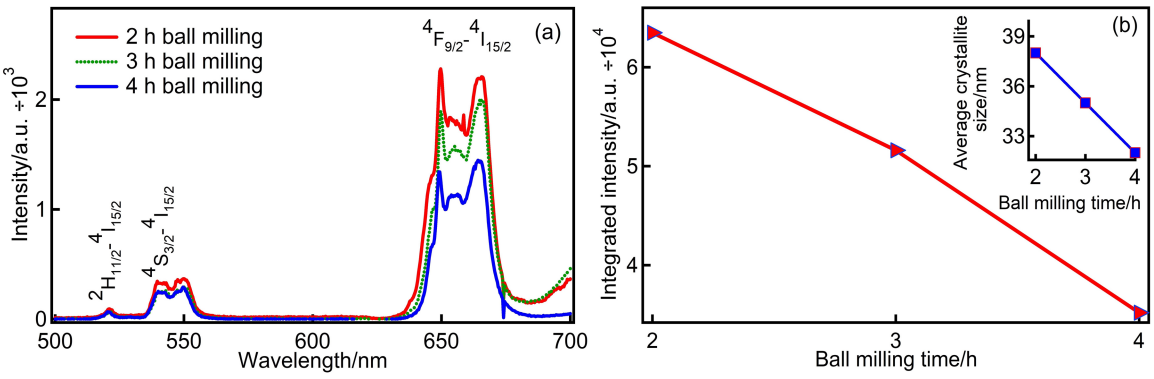

Figure 6.5: (a) Upconversion emission spectra of nanocrystalline $BaLiF_3$:1% Yb^{3+}, 1% Er^{3+} as-prepared by ball milling for 2, 3 and 4 h respectively, (b) dependence of upconversion luminescence (red triangle marker) and average crystallite size (blue rectangle marker; inset) as a function of ball milling time.

To achieve a near 100% purity of $BaLiF_3:Yb^{3+}$, Er^{3+} phase, samples of $BaLiF_3$:1% Er^{3+} with different Yb^{3+} concentrations were prepared by ball milling for an extended time of 4 h. In Figure 6.6a, the upconversion emission spectra of as-prepared $BaLiF_3$:x% Yb^{3+}, 1% Er^{3+} (x = 1, 5 and 10) nanocrystals are shown. As-prepared samples with different Yb^{3+} concentrations show the same upconversion bands located at 521, 540 and 650 nm and the sample doped with the highest Yb^{3+} concentration ($BaLiF_3$:10% Yb^{3+}, 1% Er^{3+}) exhibits the maximum emission intensity (Figure 6.6a) in agreement with the literature [36]. The enhancement of the upconversion intensity is due to the reduced average distance between Er^{3+} and Yb^{3+} ions

with increasing Yb concentration.

The upconversion efficiency of samples (Figure 6.6a) increases upon annealing (Figure 6.6b), as summarized in Figure 6.6c for the three different YbF_3 concentrations. It is most likely that the annealing process reduces the defect density in addition to reducing the surface to volume ratio. Consequently, the ratio of surface defects to volume becomes smaller too [200]. It appears that upon annealing the 5% Yb^{3+} sample shows higher upconversion luminescence intensity in comparison with the 10% Yb^{3+} sample. This is most likely due to self-quenching induced by the higher Yb^{3+} concentration.

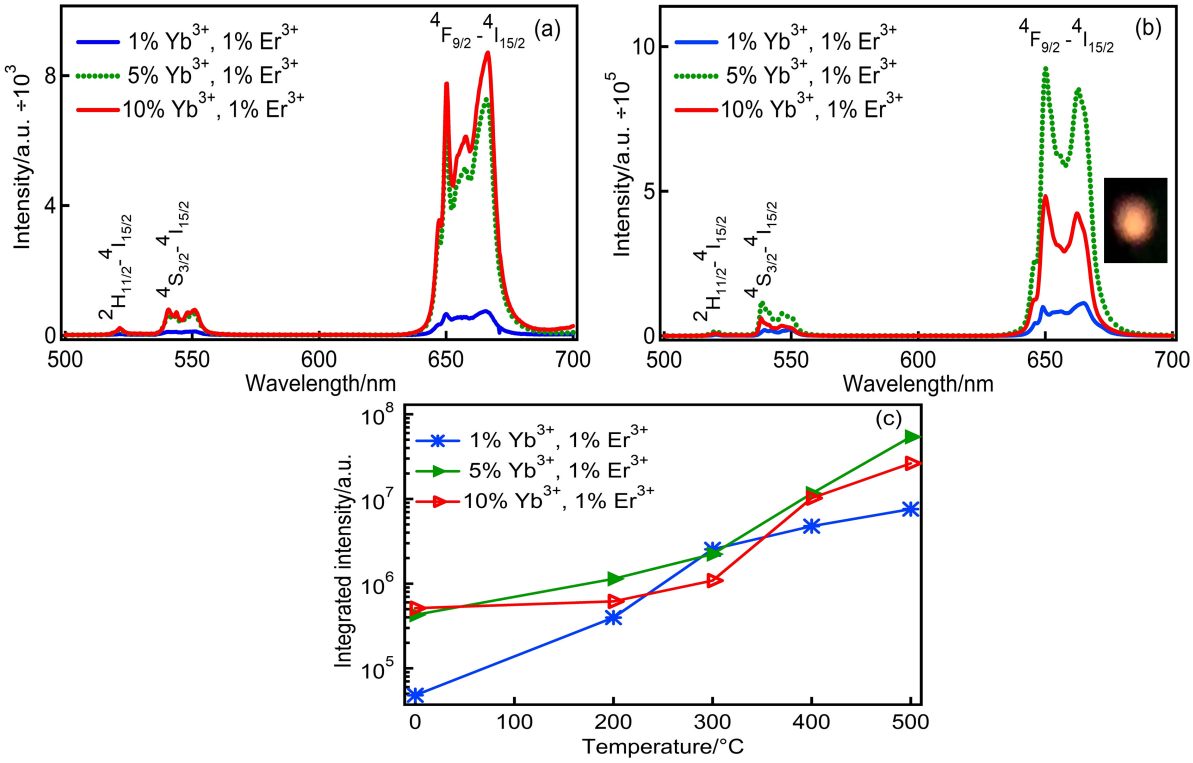

Figure 6.6: Upconversion emission spectra of $BaLiF_3$:1% Yb^{3+}, 1% Er^{3+} (blue solid line), $BaLiF_3$:5% Yb^{3+}, 1% Er^{3+} (green dotted line), $BaLiF_3$:10% Yb^{3+}, 1% Er^{3+} (red solid line) samples (a) before and (b) after annealing at 400 °C for 1 h. The inset shows a photo of the visible upconversion emission in $BaLiF_3$:5% Yb^{3+}, 1% Er^{3+} nanocrystals upon 980 nm excitation. (c) Integrated intensity of the upconversion luminescence as a function of the annealing temperature.

6.3.4 Upconversion efficiency of $BaLiF_3$:Yb^{3+}, Er^{3+} in comparison with $NaYF_4$: Yb^{3+}, Er^{3+}

To evaluate the efficiency of the $BaLiF_3$:Yb^{3+}, Er^{3+} phosphor, the upconversion luminescence intensity of $BaLiF_3$:10% Yb^{3+}, 1% Er^{3+} before and after annealing was compared with that of the best-performing upconverter $NaYF_4$:10% Yb^{3+}, 1% Er^{3+} (hexagonal phase) as is shown in Figure 6.7. Although the as-prepared $BaLiF_3$:Yb^{3+}, Er^{3+} (green solid line) exhibited the weakest upconversion efficiency, the annealed $BaLiF_3$:Yb^{3+}, Er^{3+} (red solid line) had the highest efficiency at 540 and 650 nm. Specifically, the efficiency is about 1 order of magnitude higher for $BaLiF_3$:Yb^{3+}, Er^{3+} upon annealing than in hexagonal $NaYF_4$:10% Yb^{3+}, 1% Er^{3+} as prepared (blue dotted line) as-prepared by ball milling.

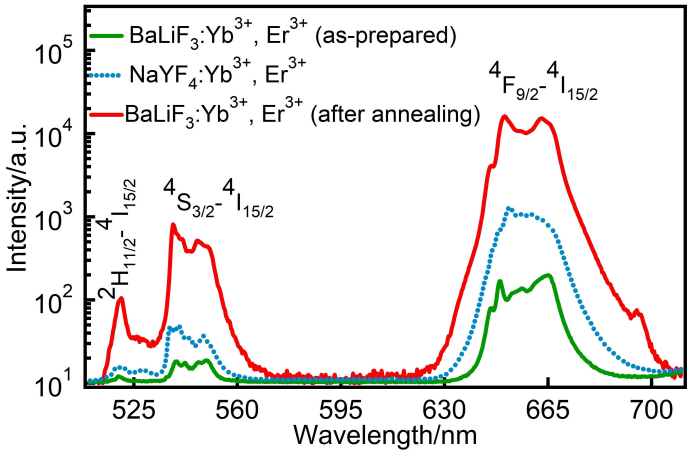

Figure 6.7: Upconversion luminescence spectra (semilogarithmic plot) of $NaYF_4$:10% Yb^{3+}, 1% Er^{3+} (as-prepared by ball milling) and $BaLiF_3$:Yb^{3+}, Er^{3+} (before and after annealing at 500 °C). Spectra were excited at 980 nm.

6.3.5 Photoluminescence

For comparison, the photoluminescence spectra of Er^{3+} and Yb^{3+} in $BaLiF_3$:Yb^{3+}, Er^{3+} are shown in Figure 6.8a and 6.8b, respectively. The photoluminescence spectrum of Er^{3+} (green dotted line) consists of three Er^{3+} bands (521, 540 and 650 nm) which is identical to the upconversion spectrum of $BaLiF_3$:Yb^{3+}, Er^{3+} (shown as a red solid line, Figure 6.8a). The photoluminescence emission of Yb^{3+} at ~980 nm (Figure 6.8b) can be assigned to the $^2F_{5/2}$

$\rightarrow {}^2F_{7/2}$ transition.

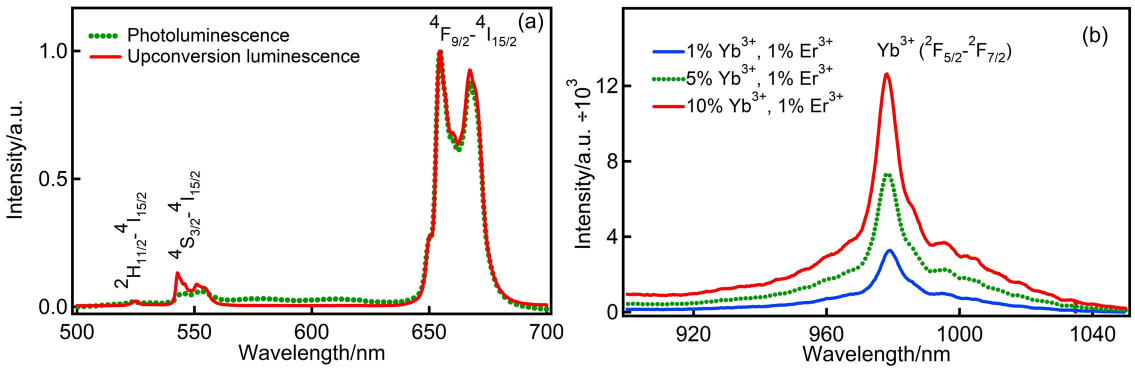

Figure 6.8: Room temperature (a) photoluminescence spectra and UCL spectra of Er^{3+} in $BaLiF_3:Yb^{3+}$, Er^{3+} (same sample) are shown in green dotted and red solid line. (b) Photoluminescence spectra of Yb^{3+} (1%, 5% and 10%) in $BaLiF_3:Yb^{3+}$, Er^{3+} excited by a 365 nm LED (Thorlabs, M365L2).

6.3.6 X-ray storage capability

The X-ray dose dependence of the Er^{3+} upconversion luminescence as well as Er^{3+} and Yb^{3+} photoluminescence in $BaLiF_3$:1% Yb^{3+}, 1% Er^{3+} nanocrystals was further investigated and is presented in Figures 6.9 and 6.10.

The reduction of upconversion luminescence upon X-irradiation follows first order dispersive kinetics where the rate depends on the distance between electron and hole traps created by X-irradiation i.e., the rate is subject to a distribution. For first order dispersive kinetics, a double exponential function is a good approximation [131, 201, 202],

$$I = A_0 + A_1 e^{(-k_1 \times dose)} + A_2 e^{(-k_2 \times dose)} \tag{6.2}$$

where, A_0, A_1, and A_2 are amplitudes and k_1 and k_2 are dose-based reduction rate constants.

More than 65% of the upconversion luminescence is lost upon exposure to X-ray irradiation in the range of $0 \rightarrow 287$ Gy as is shown in Figure 6.9. This is caused by the X-ray induced reduction of the Er^{3+} and Yb^{3+} ions. To check the stability of the upconversion luminescence,

a $BaLiF_3$:5% Yb^{3+}, 1% Er^{3+} sample was exposed to 108 Gy of X-irradiation, which led to a 45% reduction of the initial upconversion luminescence intensity. Subsequently, the sample was kept in the dark and the upconversion luminescence spectrum was periodically measured with 980 nm laser excitation, as illustrated in the inset of Figure 6.9b (green markers). It appears that upconversion luminescence gradually increased over time and reached close to its initial intensity (before X-ray) after 52 h.

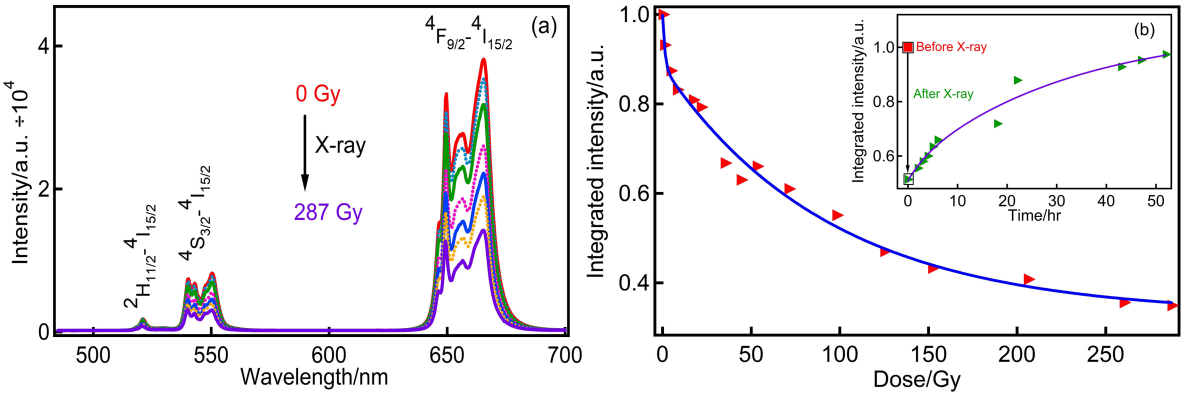

Figure 6.9: (a) Upconversion luminescence spectra of nanocrystalline $BaLiF_3$:1 mol% Yb^{3+}, 1 mol% Er^{3+} as a function of X-ray dose (0, 1, 8, 35, 98, 125 and 287 Gy). (b) Dependence of the integrated upconversion luminescence intensity on the accumulative X-ray dose (red triangles). The blue solid line represents a double exponential fit as per Equation 6.2. The inset shows the time dependence (stability) of the UCL signal (green triangles). The solid line is a bi-exponential fit.

6.3.7 Reduction of Er^{3+} and Yb^{3+} upon X-irradiation

X-ray induced electrons combine with the Er^{3+} and Yb^{3+} ions, leading to divalent Er and Yb. Due to the decrease of the concentration of the two ions upon X-irradiation (Figure 6.10), the upconversion luminescence intensity then decreases as well, as shown in Figure 6.9.

The photoluminescence spectrum of Yb^{2+} ions as a function of cumulative X-irradiation was measured and is presented in the inset of Figure 6.10a. The spectrum consists of a broad band at around 480 nm, which can be assigned to the $4f^{13}5d^1 \rightarrow 4f^{14}$ transition of Yb^{2+} [203, 204]. The increase of the Yb^{2+} peak at 480 nm with increasing X-ray dose confirms the reduction of $Yb^{3+} \rightarrow Yb^{2+}$ and clearly demonstrates that the Yb is built into the $BaLiF_3$ lattice.

Although the reduction of Er^{3+} is clearly visible in the measured photoluminescence intensity as a function of X-ray dose (Figure 6.10c), the Er^{2+} luminescence could not be detected at

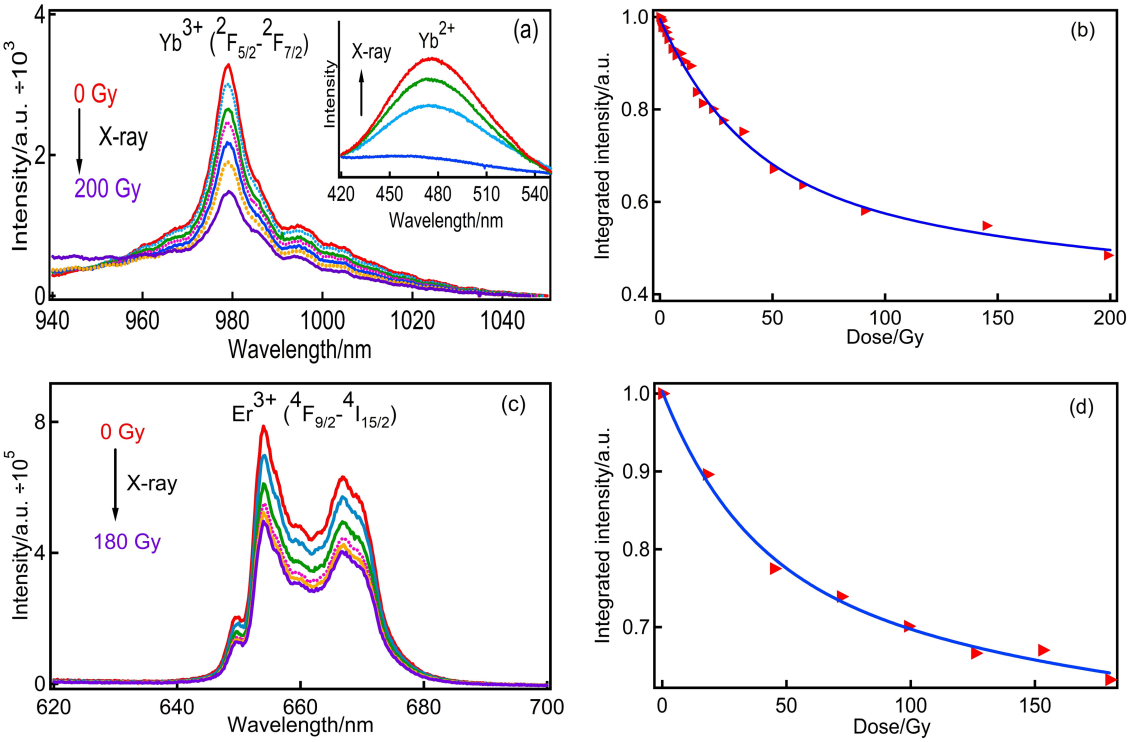

Figure 6.10: Room temperature photoluminescence spectra of (a) Yb^{3+} in nanocrystalline $BaLiF_3$:1 mol% Yb^{3+}, 1 mol% Er^{3+} as a function of X-ray dose (0, 3, 11, 19, 37, 64 and 200 Gy), The inset in (a) depicts the photoluminescence spectrum of Yb^{2+} generated upon X-ray exposure in nanocrystalline $BaLiF_3$:Yb^{3+}, Er^{3+} as a function of X-ray dose (0, 9, 36 and 108 Gy). Spectra were excited by a 265 nm LED. (b) Dependence of the integrated photoluminescence intensity of Yb^{3+} on cumulative X-ray dose. The blue solid line is a bi-exponential fit (Equation 6.2). (c) Photoluminescence spectra of Er^{3+} (excited at 378 nm) in nanocrystalline $BaLiF_3$: Yb^{3+}, Er^{3+} as a function of X-ray dose (0, 18, 72 and 180 Gy). (d) Dependence of the integrated photoluminescence intensity of Er^{3+} on cumulative X-ray dose.

~2000 nm in contrast to SrFCl [205] and CaF_2 [206]. This might be due to the fact that in centrosymmetric $BaLiF_3$, the Er^{2+} transition is very weak. Measuring weak luminescence transitions at wavelengths of around 2 μm is problematic. However, from the literature, it is clear that X-irradiation reduces the Er^{3+} ion in alkaline earth halide systems [207].

The double exponential fit parameters (from Equation 6.2) as presented in **Table 6.2** indicate a stronger dependence on X-irradiation dose of the upconversion luminescence intensity than the Yb^{3+} and Er^{3+} photoluminescence. The energy-transfer-based upconversion mechanism is nonlinearly affected by the decrease in Er^{3+} and Yb^{3+} ions, leading to this effect. It is noted here that a similar X-ray dependence of the upconversion luminescence was observed in nanocrystalline SrFCl:Er^{3+}, Yb^{3+} with reduction rates of 0.08 Gy^{-1} and 0.01 Gy^{-1} for the

UCL intensity [206]. It appears that in both systems, a certain percentage of Er and Yb ions cannot be reduced by X-irradiation as their trivalent oxidation state may be highly stabilized by next nearest neighbour defects such as oxide ions (O^{2-}) in the halide host lattice [188].

Table 6.2: Summary of parameters obtained from bi-exponential fits as per Equation 6.2, for the reduction of photoluminescence (PL) (Figure 6.10b and 6.10d) and upconversion luminescence (UCL) (Figure 6.9b).

Fit parameters	$BaLiF_3$:Yb^{3+},Er^{3+} (Er^{3+}, UCL)	$BaLiF_3$:Yb^{3+},Er^{3+} (Yb^{3+}, PL)	$BaLiF_3$:Yb^{3+},Er^{3+} (Er^{3+}, PL)
A_1	0.54 (± 0.02)	0.26 (± 0.21)	0.55 (± 0.04)
A_2	0.09 (± 0.03)	0.36 (± 0.21)	0.22 (± 0.02)
k_1 /Gy^{-1}	0.0125 (± 0.0001)	0.0039 (± 0.0135)	0.0055 (± 0.4760)
k_2 /Gy^{-1}	0.3991 (± 0.3260)	0.0274 (± 0.0106)	0.0314 (± 0.0555)

6.3.8 X-ray imaging by upconversion luminescence

Upconversion luminescence-based X-ray imaging (computed radiography) results using imaging plates composed of $BaLiF_3$ doped with 5% YbF_3 and 1% $ErCl_3$ are summarized in Figure 6.11. To the best of our knowledge, these are the first, albeit crude, examples of X-ray images based on upconversion luminescence. A steel stencil of 0.128 mm thickness was used as the radiation mask (Figure 6.11b).

The mask was placed on the phosphor film (Figure 6.11a) and X-irradiation was undertaken on the Rigaku Miniflex diffractometer (Cu-Kα X-ray source) at an angle of $2\theta = 90°$, i.e., at an (nonideal) incidence angle of 45°. The exposed plate was then scanned by a focused 980 nm laser diode (see the Experimental Methods section), rendering the image shown in Figure 6.11c.

An upconversion luminescence-based X-ray image of a slanted edge is shown in the inset of Figure 6.11d, with the resulting line spread data points (line spread function, LSF) shown as a function of x (x = pixel; pixel size = 25 μm) and with a Gaussian fit. Finally, a Fourier transformation of the LSF renders the modulation transfer function (MTF = magnitude of Fourier Transform) as a function of the spatial frequency (Nyquist = 0.5 cycles/pixel), as displayed in Figure 6.11e. In Figure 6.11e, the red line is the MTF based on the line spread data points displayed in Figure 6.11d, the blue solid line is the MTF resulting from the Gaussian

fit as shown in Figure 6.11d, and the black dash-dotted line is the ideal MTF.

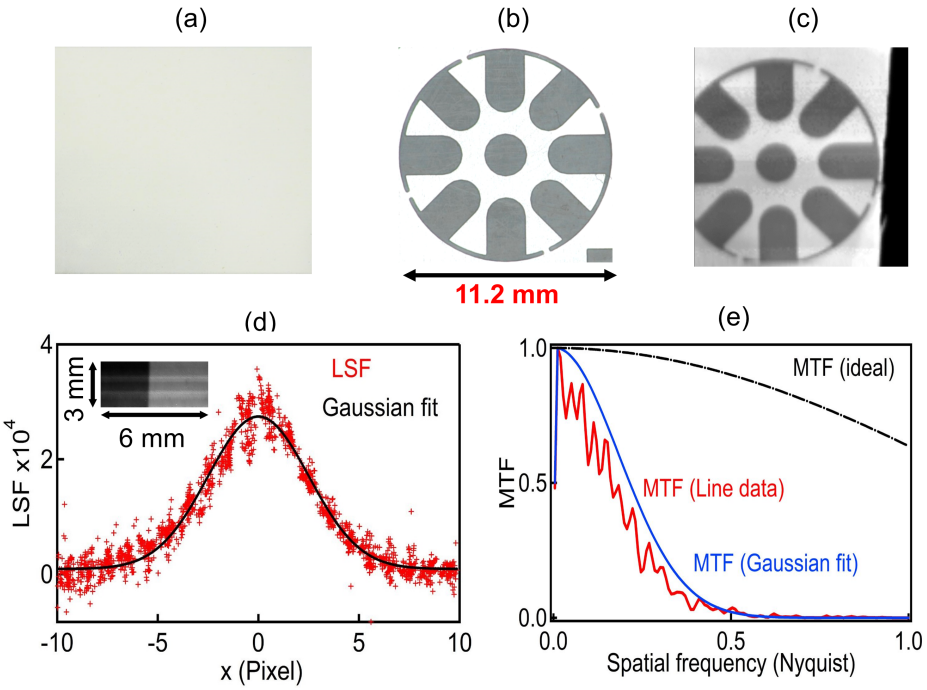

Figure 6.11: (a) $BaLiF_3$:5% YbF_3, 1% Er_3 nanophosphor-based film/imaging plate. (b) Imaged steel mask/stencil (0.128 mm thickness). (c) X-ray image of (b) computed from the UCL signal. (d) Line spread data points as a function of position (pixel, pixel size = 25 mm) obtained from the UCL-computed X-ray image of a slanted edge (6 × 3 mm scan) shown in the inset. The black solid line is a Gaussian fit to these points. (e) Modulation transfer function (MTF) as a function of spatial frequency (normalized to the Nyquist frequency $n_N = 1/(2 \times \text{pixel})$) resulting from the data points in (d) (red line) and the Gaussian fit in (d) (blue line) in comparison with the ideal MTF (black dash-dotted line).

For the present example, the MTF is predominantly limited by a relatively large focal spot of the 980 nm laser used for these preliminary experiments. Nevertheless, the MTF and the image in Figure 6.11c indicate that the present system is capable of reasonable contrast and a resolution of about 10 lp/mm and, hence, could be used for beam conditioning in radiation therapy and other applications, including in situ or in vivo imaging. Importantly, with a more focusable laser, the resolution could easily be increased to 40 lp/mm with increased contrast.

6.4 Summary

A direct and facile preparation route for an efficient nanoscale upconversion material, $BaLiF_3$: Yb^{3+}, Er^{3+} (∼20-30 nm), by utilizing a mechanochemical method is reported. The dependence

of the upconversion luminescence was investigated as a function of ball milling time, concentration of dopant (YbF_3) and post-annealing temperature. Importantly, the upconversion efficiency of as-prepared $BaLiF_3$:Yb^{3+}, Er^{3+} nanocrystals was enhanced by a factor of >100 after annealing. Upon excitation by 980 nm near-infrared (NIR) laser light, nanocrystalline $BaLiF_3$:Yb^{3+}, Er^{3+} exhibited clearly visible bright upconversion luminescence. Importantly, in comparison with hexagonal $NaYF_4$ doped with Yb^{3+} and Er^{3+}, the $BaLiF_3$:Yb^{3+}, Er^{3+} nanocrystals exhibited an order of magnitude higher upconversion luminescence intensities. The 980 nm Yb^{3+} luminescence decreases with increasing X-ray dose due to the reduction of the Er^{3+} and Yb^{3+} ions to their divalent states, resulting in a 65% loss of the original UCL signal in $BaLiF_3$:Yb^{3+}, Er^{3+} nanoparticles upon 287 Gy X-irradiation. The reduction of Yb^{3+} to Yb^{2+} upon cumulative X-ray dose at 480 nm was clearly demonstrated. Preliminary X-ray imaging experiments using the UCL signal are the first of its kind and these results point to potential future applications, ranging from radiation therapy to industrial imaging, dosimetry, and upconversion in vivo imaging.

Chapter 7

Near-infrared F_3^+ colour centre in pure $BaLiF_3$

7.1 Introduction

Colour centres are omnipresent features of ionic crystals and characterised by their sharp, intense zero-phonon line emission which is useful for optical data storage, dosimetry and tunable colour centre laser applications. $BaLiF_3$ has been reported as an ideal system for generation of F-aggregate defects/colour centres. Several intrinsic colour centres including F-centre, F_2, F_2^+, F_3 and F_3^+ [164–166] were reported in $BaLiF_3$ crystal, and their stability were investigated. Importantly, the generation and stability of theses colour centres depends on the quality and growth process of the crystals. However, the earlier studies of the intrinsic F-based colour centres only focussed on investigation of their absorption properties, and a systematic experimental demonstration of other important characteristics, such as their luminescence properties, response to X-ray radiation (for application in dosimetry), and their behaviour under an external magnetic field is missing. Therefore, further systematic studies are clearly required.

This chapter demonstrates the generation of a unique F_3^+ colour centre detected in mechano-chemically synthesized $BaLiF_3$ upon annealing. The photoluminescence property and X-ray sensitivity of the colour centre are systematically investigated. Finally, the effect of a magnetic field up to 9 T on the F_3^+ luminescence (at low temperature) is investigated by a Zeeman experiment.

7.2 Experimental details

7.2.1 Preparation of $BaLiF_3$

Firstly, BaF_2 was prepared by co-precipitation of barium nitrate $Ba(NO_3)_2$ (May & Baker Australia Pty Ltd) and ammonium fluoride NH_4F (Sigma Aldrich, ACS grade) and then dried at 60 °C in an oven for 24 h. Then $BaLiF_3$ powder was prepared by ball milling equimolar quantities of BaF_2 and LiF (Ajax chemicals; Sydney, Australia) on a Retsch Mixer Mill MM 200. Specifically, 1 mmol BaF_2 (0.175 gm) and 1 mmol of LiF (0.026 gm) powders were ball-milled for 3 h at a frequency of 20 Hz.

The ball-milled powder samples were annealed in an open ceramic boat crucible that was placed in an MTI GSL-1100 tube furnace. During the annealing process, the furnace temperature was kept stable and the atmosphere was controlled by a continuous gas flow ($Ar/O_2/N_2/H_2$).

7.2.2 Structural characterization

The structure of the as-prepared powder samples was verified by powder X-ray diffraction utilizing a Rigaku Miniflex-600 benchtop powder diffractometer with a Cu-Kα ($\lambda = 0.154$ nm) radiation source operating at 40 kV and 15 mA. The experimental data was recorded in the 2-θ range of 10° to 90° with an interval of 0.02° and at speed 0.5°/min.

TEM (transmission electron microscopy) was performed by utilizing a FEI Tecnai G2 Spirit TEM . To record high resolution TEM images, powder samples were suspended in ethanol and then dispersed onto copper grids. In addition, SEM (scanning electron microscopy) and SEM-EDS mapping were performed with a Zeiss Crossbeam 540 with SDD EDS (Oxford Instruments X-MaxN).

X-ray photoelectron spectroscopy (XPS) was carried out on an ESCALAB250Xi (Thermo Scientific, UK) spectrometer to investigate the oxidation states of Ba, Li and F before and after annealing.

7.2.3 Photoluminescence spectroscopy

The photoluminescence spectra were excited by a 462 nm blue diode laser and collected on a Spex 500 M monochromator (150 grooves/mm grating blazed at 500 nm) equipped with an Andor iDus Silicon CCD (DV401A-BV) camera cooled to -60 °C. A closed cycle cryostat (CTI-Cryogenics Cryodyne model 22) was utilized to cool the sample for low temperature photoluminescence measurements. A 470 nm pulsed LED was used to conduct the lifetime measurement within the temperature range of 2 to 293 K. A 462 nm laser diode modulated by an Isomet 1250C acousto-optic-modulator was employed to measure the lifetime at high temperature.

The low temperature excitation spectra in the 765 nm region were measured by using a Spex 1704 1 m monochromator (1200 grooves/mm grating) and a 780 nm red LED was used as the light source. The emission was detected by a cooled photomultiplier tube (Hamamatsu R943-02, PMT) that was equipped with three FB 810-10 nm band-pass filters, a FEL 800 nm long-pass filter and an RG 780 nm colour glass filter. A cold stage of a closed cycle refrigerator (Janis/Sumitomo SHI-4.5) was used to cool the sample to low temperatures.

7.2.4 Zeeman experiment

The Zeeman experiments were performed using a commercial physical property measurement system (PPMS-9, Quantum Design) which includes a liquid helium cryostat and a superconducting magnet (9 Tesla). The Zeeman spectra were recorded by using the Spex 500M monochromator equipped with the Andor iDus Silicon CCD (as described above). The spectrometer was coupled to the PPMS system by a 2 m fiber-bundle (Thorlabs BF13LSMA02). In this experiment, the 462 nm laser diode was used to excite the luminescence.

Preliminary Zeeman experiments were conducted over the smaller 0 - 5 Tesla range by employing a Spex 1402 0.75 m monochromator (1200 line/mm grating blazed at 500 nm). The sample was placed in a magneto-optical cryostat (6T SM-4 Oxford Instruments Spectro-mag unit) with the sample at temperatures between 1.8 K and 30 K. Emission within the range of 400 to 850 nm was monitored with a Hamamatsu R-669 photomultiplier tube. The versatile spectrometer system utilized is described in more detail in ref. [207]. A 470 nm blue LED

was used as the excitation source. For wavelength to wavenumber conversions, the refractive index of air was taken into account.

7.3 Characterization of pure $BaLiF_3$

7.3.1 Powder X-ray diffraction (XRD) pattern

The powder X-ray diffraction patterns of nanocrystalline $BaLiF_3$ prepared by ball milling before and after annealing at 800 °C, are shown in Figure 7.1. All the prominent XRD peaks can be indexed to the standard pure cubic $BaLiF_3$ structure with space group Pm-3m. Refinements were performed with input parameters from the CIF file from the Springer Materials database [171] (PDF No. 180715) by using the MAUD software package [170]. The resulting fitting parameters from the Rietveld refinement are summarized in **Table 7.1**.

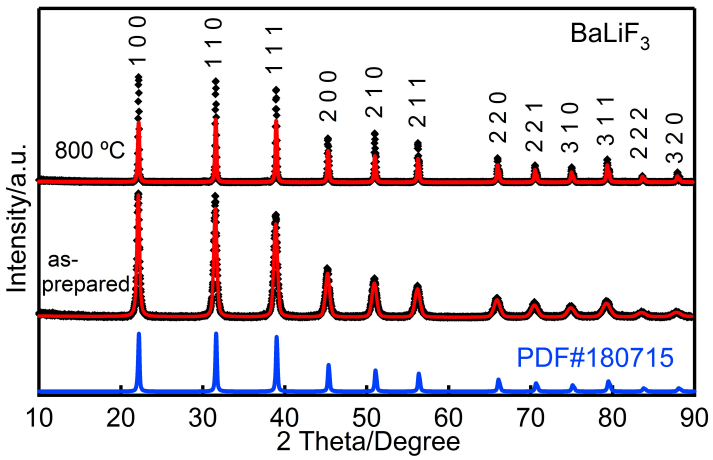

Figure 7.1: Powder X-ray diffraction pattern of as-prepared and 800 °C-annealed $BaLiF_3$. Experimental data and the Rietveld refinements are shown by black diamonds and as red solid lines, respectively. Standard data for cubic $BaLiF_3$ (PDF#180715) [171] is shown for comparison (blue solid trace).

Table 7.1: Rietveld refinement summary.

Name	Lattice Parameter /Å	Average Crystallite Size /nm	R_{wp} %	R_{exp} %	G
Standard $BaLiF_3$	3.996(3)	—	—	—	—
As-prepared	4.008(2)	50 ± 1	20	13	1.5
800 °C	4.002(7)	410 ± 14	27	15	1.8

It can be seen from **Table 7.1**, that post-annealing treatment results in an increase in crystallite size. For example, the average crystallite size of as-prepared $BaLiF_3$ is 50 ± 1 nm whereas after annealing at 800 °C, this increases to 410 ± 14 nm. In **Table 7.1**, the weighted-profile R factor, R_{wp} , the expected R-factor, R_{exp} , and the goodness of fit G (= R_{wp}/R_{exp}) are given (G< 2, is considered to indicate a good fit).

7.3.2 TEM and SEM micrographs

The structural features of nanocrystalline $BaLiF_3$ before and after annealing were further investigated by using transmission electron microscopy (TEM) (Figure 7.2) and scanning electron microscopy (Figure 7.3) and SEM based EDS elemental maps (Figure 7.4).

Figure 7.2 contains typical TEM images of (a) as-prepared $BaLiF_3$ and (b) $BaLiF_3$ annealed at 800 °C for 2 hours. These images demonstrate that the annealing process leads to an increase in the crystallite size.

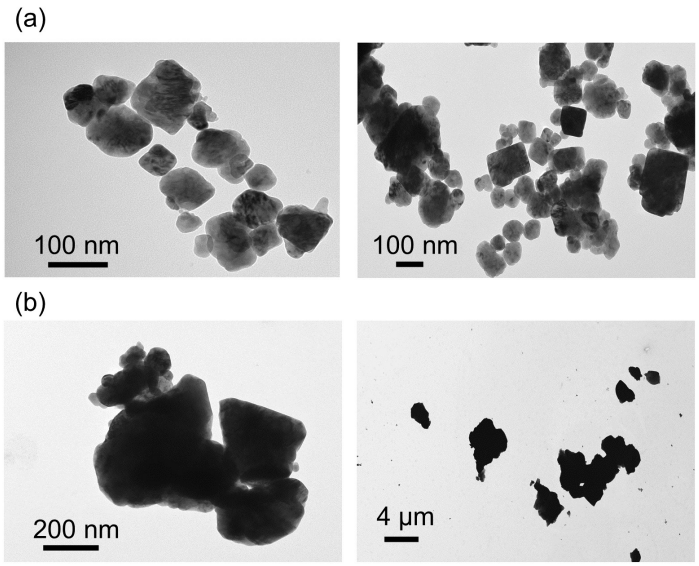

Figure 7.2: Representative TEM images of $BaLiF_3$ prepared by ball milling (a) before and (b) after annealing at 800 °C.

SEM micrographs of as-prepared (panel I) and 800 °C annealed (panel II) $BaLiF_3$ samples are presented in Figure 7.3. It shows the annealing process increases the crystallite and particle size.

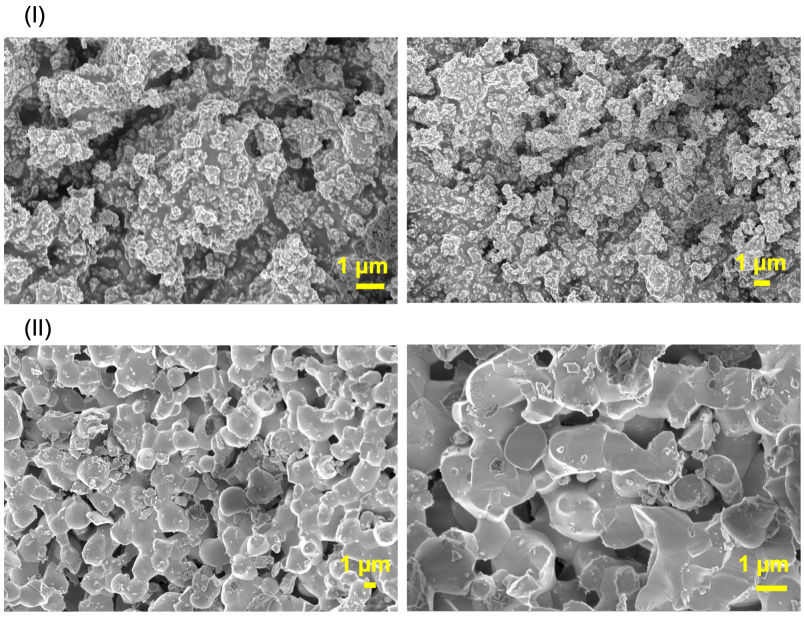

Figure 7.3: SEM micrographs of (I) as-prepared $BaLiF_3$ and (II) $BaLiF_3$ annealed at 800 °C.

2D SEM-EDS elemental maps of as-prepared and annealed $BaLiF_3$ are illustrated in Figure 7.4. It shows uniform distribution of Ba and F (Li is too light to be detected by SEM-EDS).

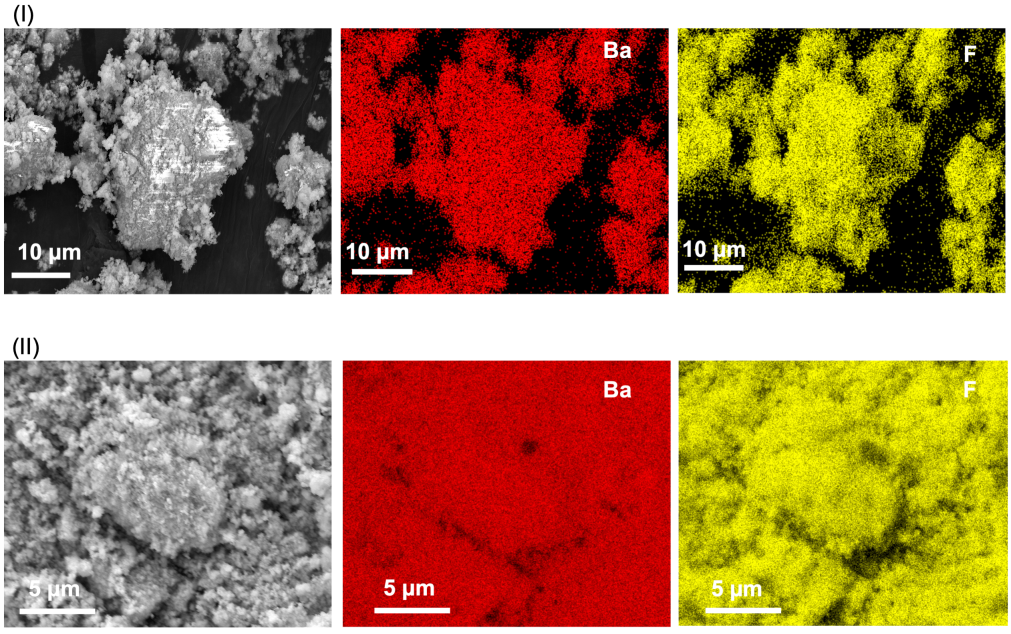

Figure 7.4: SEM based EDS 2D map of (I) as-prepared $BaLiF_3$ and (II) $BaLiF_3$ annealed at 800 °C.

7.3.3 XPS spectra

The elemental composition of $BaLiF_3$ was investigated by using X-ray photoelectron spectroscopy (XPS). The XPS core-level spectra of Ba 3d, Li 1s and F 1s are shown in Figure 7.5.

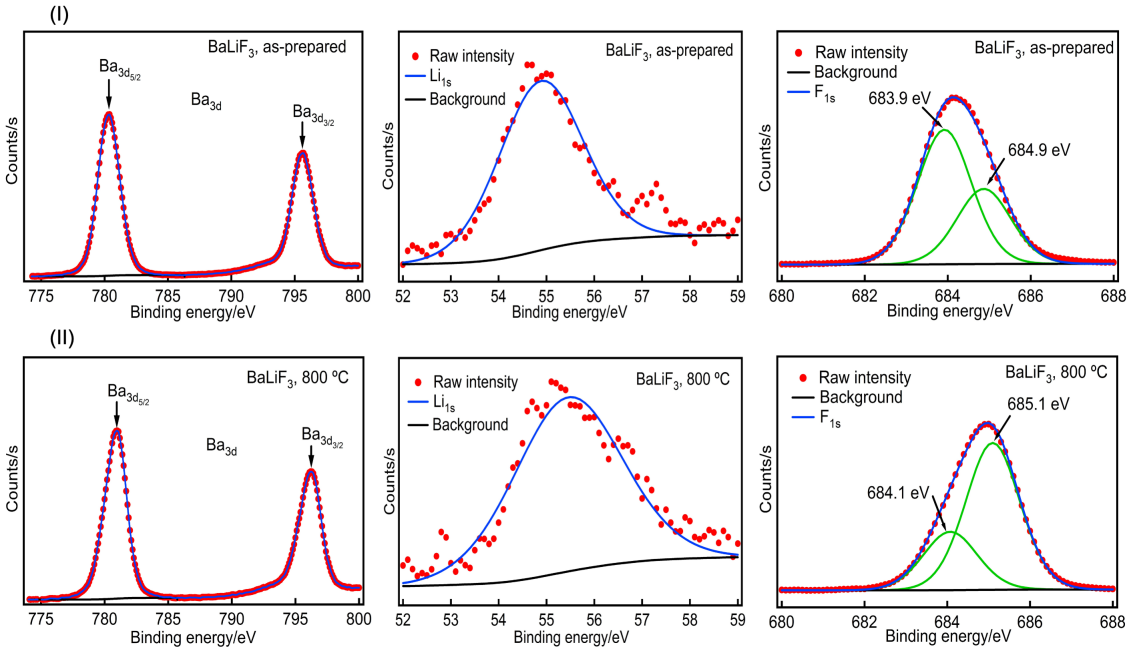

Figure 7.5: High resolution XPS spectra of Ba 3d, Li 1s and F 1s in pure $BaLiF_3$ before (top panel I) and after (bottom panel II) annealing.

In both samples (i.e., as-prepared and annealed), the Ba 3d spectra exhibits two well-separated peaks at ∼795.2 eV and ∼780.3 eV due to the spin-orbit components [208] which is a characteristic of Ba in the Ba^{2+} valence state. The peaks at ∼795.2 eV and ∼780.3 eV correspond to Ba $3d_{3/2}$ and Ba $3d_{5/2}$ core levels, respectively. These values are close to the values reported for Ba 3d in $BaFe_2As_2$ (795.1 eV and 779.7 eV for Ba $3d_{3/2}$ and Ba $3d_{5/2}$, respectively [208]). The spin-orbit energy separation between Ba $3d_{3/2}$ and Ba $3d_{5/2}$ was 15.2 eV for both samples and this is characteristic of the 2+ oxidation state of Ba (Ba^{2+}) [209]. The XPS spectra of Li 1s, located at the binding energy of ∼55.45 eV can be fitted by a single Gaussian. In contrast, the F 1s spectra can be decomposed into two Gaussian profiles (green solid lines). For the as-prepared sample the two fitted peaks are centered at 683.9 eV and 684.9 eV, similar to that reported for BaF_2 and LiF [210, 211]. Importantly, in the annealed sample they are located at

684.1 eV and 685.1 eV, respectively, very close to that of the as-prepared sample. This implies that no significant energy difference is observed for the fluoride F 1s peak before and after annealing.

7.3.4 Photoluminescence Spectroscopy

Figure 7.6 is a plot of the room temperature photoluminescence spectrum of $BaLiF_3$ excited at 462 nm (a) before and (b) after annealing. No emission was detected in as prepared nanocrystalline $BaLiF_3$ (blue trace). In contrast, a relatively intense emission with an electronic origin at ~766.9 nm and with pronounced vibrational side lines was observed after annealing (red markers). The vibrational sideband contains three resolved bands at 773, 788 and 810 nm.

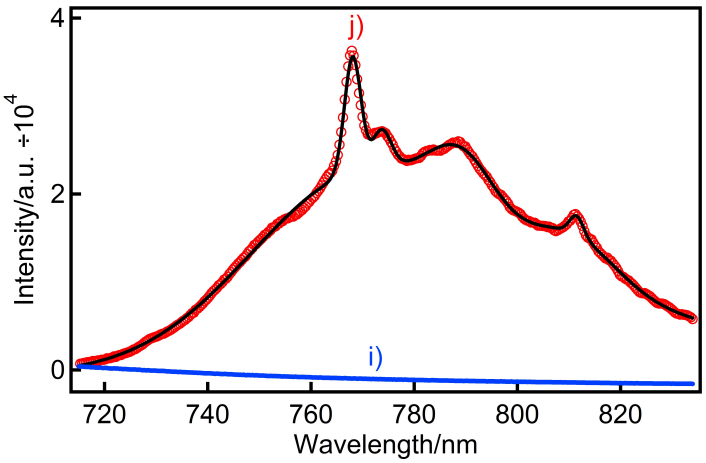

Figure 7.6: Room temperature photoluminescence spectrum of $BaLiF_3$ i) before and j) after annealing. The sample was annealed under an argon gas flow at 700 °C for 2 h. A 462 nm laser diode was used as the excitation source. The black solid line is a multipeak fit to the luminescence spectrum, with the line shape of the origin assumed to be Lorentzian.

The temperature dependence of the photoluminescence spectrum of the annealed sample is shown in Figure 7.7a. At low temperature (8 K) the zero-phonon line (764.8 nm) was more distinct compared to the phonon sideband, and a blue shift of 32 cm^{-1} was observed (Figure 7.7c). At low temperature the width of the zero-phonon line is limited by inhomogeneous broadening whereas at room temperature the homogeneous linewidth dominates. In particular, a linewidth increase (Figure 7.7b) from 20 cm^{-1} at 8 K (inhomogeneous width plus instrumental component) to 50 cm^{-1} at 293 K (homogeneous width) was observed and the transition shifted (Figure 7.7c) to lower energy by 32 cm^{-1} when the temperature was in-

creased from 8 K to 293 K. For comparison, the ruby R_1 linewidth is ~12 cm^{-1} at room temperature and the total red shift between liquid helium and room temperature is ~20 cm^{-1} [212].

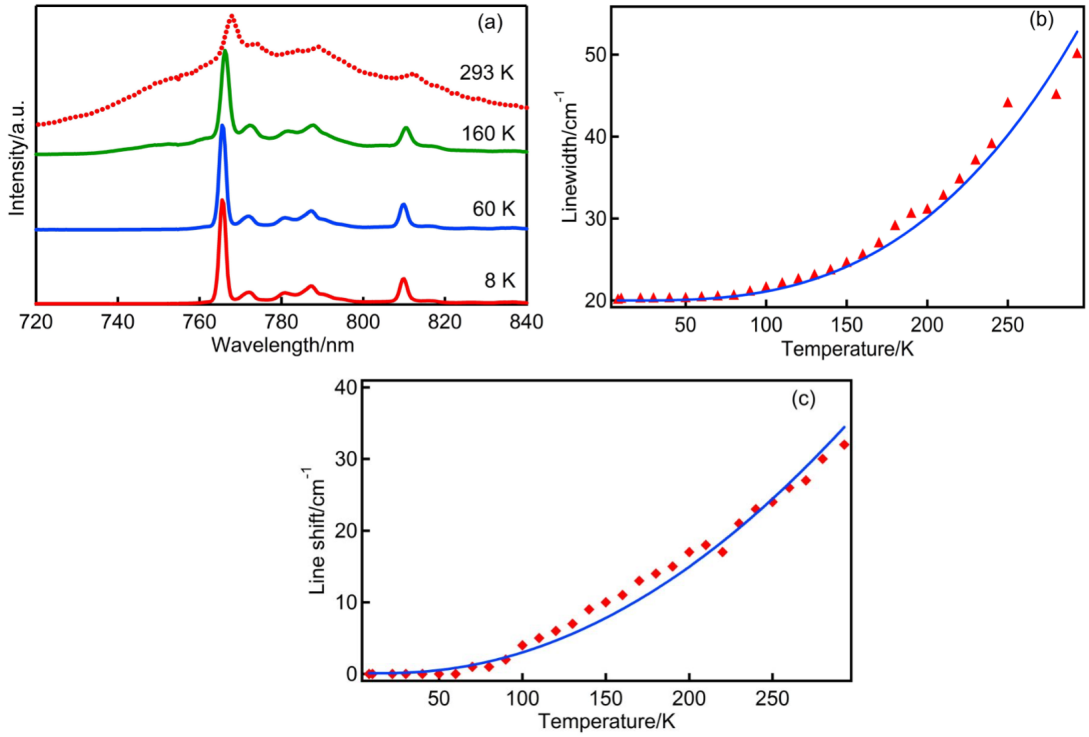

Figure 7.7: (a) Temperature dependence of the photoluminescence spectrum for post-annealed nanocrystalline $BaLiF_3$.The sample was annealed at 600 °C. Temperature dependence of (b) linewidth and (c) line shift of the electronic origin as evaluated from the spectra shown in Figure 7.7a. Solid blue lines represent the McCumber and Sturge fit functions for the linewidth (Figure 7.7b, Equation 7.1) and the line shift (Figure 7.7c, Equation 7.2).

It is well documented that electron-phonon interactions result in thermal broadenings and shifts of energy levels. The effect of temperature on the linewidth and position of the zero-phonon line can be approximated by the McCumber and Sturge formulas [213],

$$\Delta E_{LW} = \Delta E_0 + \bar{\alpha}(\frac{T}{T_{DW}})^7 \int_0^{T_{DW}/T} \frac{x^6 e^x}{(e^x - 1)^2} dx \tag{7.1}$$

$$\Delta E_{LS} = \alpha(\frac{T}{T_{DS}})^4 \int_0^{T_{DS}/T} \frac{x^3}{e^x - 1} dx \tag{7.2}$$

In Equation 7.1, ΔE_{LW} is the temperature-dependent contribution to the linewidth of the

energy level, and ΔE_0 is the residual width due to inhomogeneous broadening, instrumental limitations, and in the ideal case (i.e., with the absence of inhomogeneous broadening and instrumental limitations) dephasing processes. In Equation 7.2, ΔE_{LS} is the thermal shift of the line position. In both cases, $\bar{\alpha}$, α , indicate the coupling co-efficient for the electron-phonon interaction for linewidth and line shift, respectively. T_{DW} and T_{DS} represent the effective Debye temperature for linewidth and line shift for the phonon distribution, respectively. The linewidth data in Figure 7.7b fitted well to Equation 7.1, by using $\bar{\alpha}$ and T_{DW} values of 0.04 cm^{-1} and 180 K, respectively. The Debye temperature of $BaLiF_3$ was experimentally determined as 280 K [214]. The fit of Equation 7.2 to the line shift data shown in Figure 7.7c yields α = 0.02 cm^{-1} and T_{DS} =120 K. It is noteworthy that one should not overinterpret the $\bar{\alpha}$, α , T_{DW} and T_{DS} values as they are not fully independent.

7.3.5 Lifetime measurement

Figure 7.8 shows a graph of the temperature dependence of the luminescence decay of the zero-phonon line in $BaLiF_3$ at temperatures between 2 K to 438 K. The decay curves fit well to a single-exponential function (Figure 7.8, inset) at all temperatures.

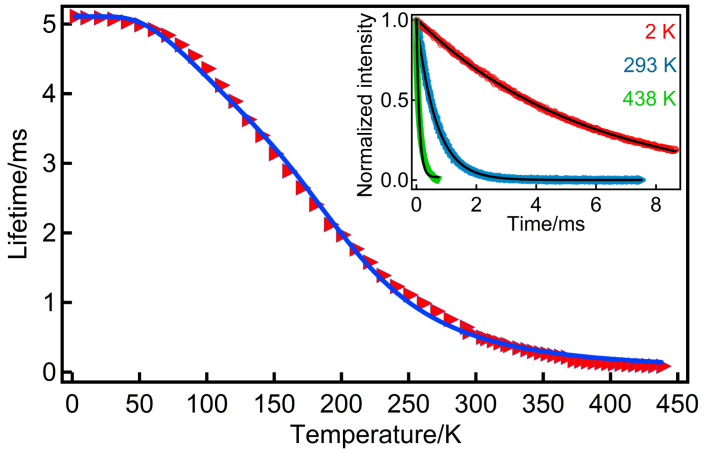

Figure 7.8: Temperature dependence of the excited state lifetime. The solid blue line is a fit to Equation 7.3. The inset shows the luminescence decay of the colour centre at 2 K and 293 K and 438 K (the solid black lines show single exponential fits). The sample was annealed at 600 °C for 2 h. A pulsed 470 nm LED and a 462 nm laser diode were used as the excitation source.

The 765 nm band has a long lifetime of 5.1 ± 0.1 ms (2 K) which is a strong indication of a spin-forbidden transition [215]. Interestingly, this lifetime is comparable to the one of the spin-

forbidden ruby R-lines (∼3.8 ms). Whilst spin-orbit coupling is relatively large for the Cr^{3+} centres, spin-orbit coupling is enhanced for colour centres in $BaLiF_3$ because of the external heavy atom effect due the presence of the Ba ions.The lifetime remains relatively constant in the temperature range of 2 to 60 K but decreases abruptly with increasing temperature above 60 K reaching a room temperature value of 644 ± 2 µs and 84 ± 5 µs at room temperature and 438 K, respectively.

The excited state lifetime as a function of temperature can be determined by Equation 7.3 which rationalize the decreasing luminescence lifetime, due to vibronic coupling with an effective phonon frequency and due to activation to a higher energy level with a faster deactivation rate [216].

$$\tau^{-1} = \tau_0^{-1} coth(\frac{h\omega}{2k_BT}) + \tau_1^{-1} exp(-\frac{\Delta E}{k_BT}) \tag{7.3}$$

τ_0 is the lifetime at lowest temperature (T = 2 K), k_B is Boltzmann's constant and hω is the phonon energy, τ_1^{-1} is the effective decay probability for a higher-energy level and ΔE indicates the activation energy. The first term in Equation 7.3 describes the lifetime shortening by vibronic coupling whereas the second term describes the lifetime shortening via the population of a higher-lying excited state with a shorter lifetime i.e., a faster decay channel. The fit of Equation 7.3 to the data presented in Figure 7.7 yields τ_0 = 5.1 ms, hω = 165 cm^{-1}, τ_1 = 6 µs and ΔE = 979 cm^{-1}.

7.3.6 Zeeman Experiment

As is illustrated in Figure 7.9a, the zero-phonon line displayed two components at 13,071.1 cm^{-1} (764.8 nm) and 13,067.1 cm^{-1} (765 nm) (green dash lines) at 8 K i.e., a splitting of 4.2 cm^{-1} wavenumbers (obtained by a fit to two Gaussian line shape functions) which may be due to the presence of two optically inequivalent sites or a zero-field splitting of the ground or excited state. It is important to mention that this splitting is well resolved only in the sample which was annealed at lower temperatures (600 °C).

Figure 7.9b shows the 1.8 K luminescence spectrum of the zero-phonon line (at 764.8 nm) measured for magnetic fields from 0 to 9 Tesla for a sample annealed at 800 °C. In this case,

the 4.2 cm^{-1} splitting is less visible in the zero-field spectrum compared to the spectrum shown in Figure 7.9a for the sample annealed at 600 °C. With increasing magnetic field flux, the zero-phonon line splits into three components. The 9 T spectrum has peaks corresponding to three transitions centered at ∼764.4 nm, ∼764.83 nm, and ∼765.33 nm, respectively. This result is strong evidence that the splitting observed at low temperature in the absence of a magnetic field is due to the zero-field splitting rather than being due to two optically inequivalent chromophores.

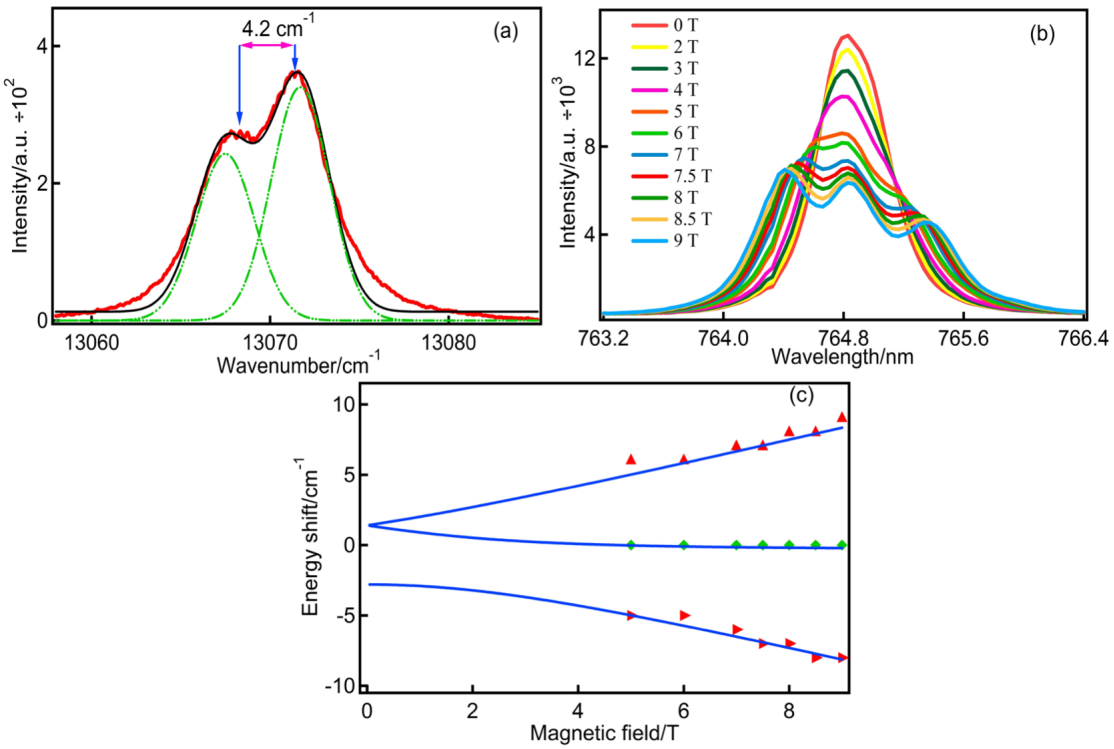

Figure 7.9: (a) Splitting (4.2 cm^{-1}) of the zero-phonon line at 0 T and 8 K (red solid line). This spectrum is fitted to two Gaussian line shapes (green dash line) of equal width (black solid line). (b) Magnetic field induced splitting (Zeeman effect) of the electronic transition at 764.8 nm in $BaLiF_3$. Spectra were measured at different magnetic field strengths ranging from 0 to 9 T at 1.8 K. (c) Zeeman splitting as obtained from Figure 7.9b by using Lorentzian fit functions. The shift relative to 13,070 cm^{-1} is shown. The blue solid lines indicate a simulation of a randomly orientated triplet state by using Equation 7.4 (with S = 1, D = 4.2 and E = 0). A 462 nm blue laser was used as the excitation source.

The Zeeman splitting of the zero-phonon line at 764.8 nm is evaluated from Figure 7.9b by using the sum of three Lorentzian line shapes and it is presented as a function of the magnetic field flux in Figure 7.9c. The observed lack of a significant temperature dependence of Zeeman

split spectrum demonstrates that the magnetic field splitting occurs in the ground state, indicative of a triplet ground state. Such a conclusion can be drawn as the relatively long excited state lifetime of 5 ms would allow thermalization of split excited state levels, and a red shift of the spectrum would be expected with a single dominant lower energy component. The energy level splitting in an external magnetic field can be described by using a spin Hamiltonian (Equation 7.4 [217, 218]) for a randomly oriented triplet system (as shown in Figure 7.9c, blue solid lines) with S = 1, D = 4.2 cm^{-1} and E = 0 cm^{-1}.

$$H = g\mu_B \bar{H}.\bar{S} + (D(S_z^2 - \frac{1}{2}S^2) + E(S_x^2 - S_y^2)) \tag{7.4}$$

In Equation 7.4, D and E describe the zero-field splitting. For the simulated energies, 13,067.3 cm^{-1} and 13,071.5 cm^{-1} (at 0 T), randomly orientated triplet states were averaged in a simulation of 1000 optical centres for each magnetic field strength.

The experimental data (red and green markers) follow the trend of the simulation very well. From the Zeeman spectroscopy it can be concluded that the sharp peak emission in pure $BaLiF_3$ observed upon annealing must be due to the formation of F-centre aggregates [219] (a single F-centre would only have S = 1/2 states).

7.3.7 Excitation spectra measurement

To confirm the above statement, excitation spectra of the zero-phonon line emission were measured as is shown in Figure 7.10a. The excitation spectrum displayed a broad and intense excitation band centered around 488 nm for emission monitored at ~765 nm (Figure 7.10a). Thus the luminescence is most likely due to F_3^+ centres that were reported to absorb at 480 nm in the literature [164, 165].

To further verify that the ground and not the excited state is the triplet state, excitation spectra in the region of the electronic origin were measured by monitoring the relatively intense vibrational side band emission at 810 nm (Figure 7.10b). Importantly, the excitation spectrum confirms that the 764.8 nm emission transition in $BaLiF_3$ is purely electronic as it coincides with the origin in emission (as shown in the Figure 7.10b inset). It is important to note that the excitation spectrum shows a decrease in intensity when the temperature is increased to 25

K (green solid line) from 6 K (red solid line).

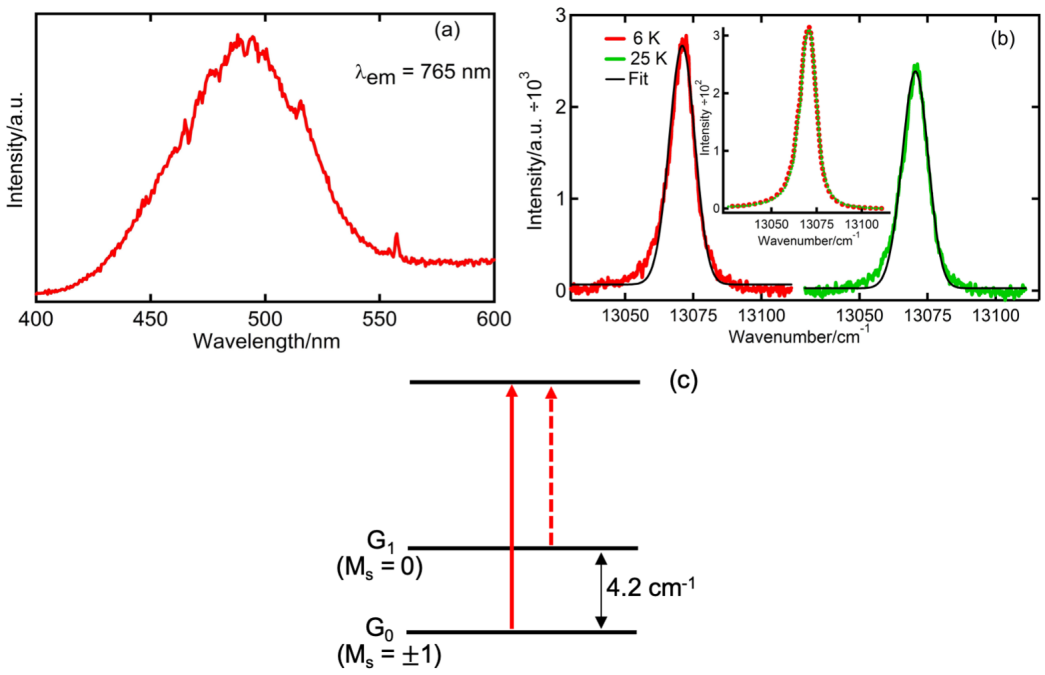

Figure 7.10: Excitation spectra of annealed $BaLiF_3$ for emission observed at (a) 765 nm (77 K) and (b) 810 nm (6 K - red trace, 25 K - green trace). Solid black lines in (b) represent fits obtained by using Equation 7.5 and the inset shows the corresponding photoluminescence spectra (6 K - red dotted line and 25 K - green dotted line) by using 470 nm LED excitation. (c) Energy level diagram for single-triplet transition with a zero-field splitting of 4.2 cm^{-1}. A Fluoromax-3 fluorometer was employed to scan the excitation spectra in the range of 400 to 600 nm. A Spex 1704 1 m monochromator (1200 grooves/mm grating) was used to measure the excitation spectra around 765 nm (13,067 cm^{-1}) range. Samples were annealed at 800 °C.

This phenomenon i.e., the temperature dependence of the excitation spectrum (6 K and 25 K) can be described by a double Gaussian for the two transitions separated by 4.2 cm^{-1}, and the two components are subjected to a Boltzmann distribution of the two levels in the ground state (Equation 7.5).

$$f(x) = A[(\frac{2}{2+exp(\frac{-4.2}{k_BT})})exp(-(\frac{x-x_0}{w})^2) + \frac{1}{2}(\frac{exp(\frac{-4.2}{k_BT})}{2+exp(\frac{-4.2}{k_BT})})exp(-(\frac{x-(x_0-4.2)}{w})^2)] \tag{7.5}$$

In Equation 7.5, f(x) is the sum of two Gaussian line shape functions. A is the amplitude, k_B is the Boltzmann constant (0.695 cm^{-1}/K), x_0 is the wavelength and w is the width.

The 6 K and 25 K excitation spectra were fitted with Equation 7.5 taking the $M_s = \pm 1$ level as the lower state in the triplet ground state in zero field (black solid line in Figure 7.10b). In both cases the best fit yields A = 0.0029, w = 6 cm^{-1} and x_0 = 13,071 cm^{-1}.

This confirms that the $M_s = \pm 1$ triplet component, is the lowest state (G_0, Figure 7.10c).

In addition, the photoluminescence emission at 764.8 nm shows no change in intensity with increasing temperature (from 6 K to 25 K) (red and green dotted line in the Figure 7.10b inset).

In summary, the experimental results indicate that the emission at 764.8 nm is most likely due to a singlet-triplet transition of the F_3^+ colour centre with a triplet ground state.

7.3.8 Effect of gases

An interesting phenomenon associated with the F_3^+ centre was discovered when different atmospheres (Ar, O_2, Air, N_2 and H_2) were used in the annealing process as is illustrated in Figure 7.11.

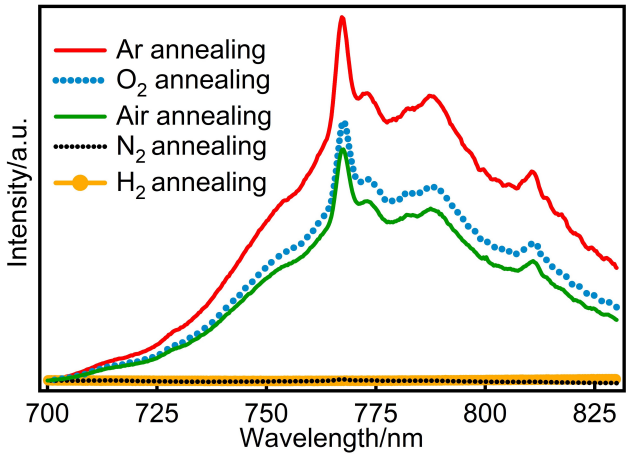

Figure 7.11: Room temperature photoluminescence spectra of $BaLiF_3$ after annealing under argon, oxygen, air, nitrogen and hydrogen gas at 600 °C for 2 h. Spectra were measured at room temperature and excited by a 462 nm laser diode.

All samples were annealed at 600 °C for 2 h and then the photoluminescence spectra were measured at room temperature. Maximum photoluminescence intensity, i.e. creation of F_3^+ centres, was observed for annealing under Ar. In contrast, no luminescence was detected when the sample was annealed under hydrogen. Somewhat surprisingly, similar behaviour was also observed when the sample was annealed under N_2 gas. This experiment implies that H_2 and

N_2 provide a reducing environment and hence prevent the formation of the F_3^+ centre. Whilst it is clear that H_2 is a reducing agent, this is not the case for N_2. A possible explanation for this is that under nitrogen the F_3^+ centre is not formed because of the formation of some nitrogen impurities that are built into the lattice during the high temperature treatment.

7.3.9 X-ray sensitivity

The dependence of the F_3^+ centre upon exposure to X-rays was also explored as is illustrated in Figure 7.12.

An annealed nanocrystalline $BaLiF_3$ sample was exposed to X-rays (Rigaku Miniflex 600, Cu-Kα, 40 kV, 15 mA). Figure 7.12b is a demonstration of the luminescence bleaching of the F_3^+ centre as a function of cumulative X-ray dose. The bleaching process follows first-order dispersive kinetics for which a double exponential function is a reasonable approximation. This result indicates that the X-ray liberated electrons combine with F_3^+ defect centres resulting in a decrease of the luminescence signal.

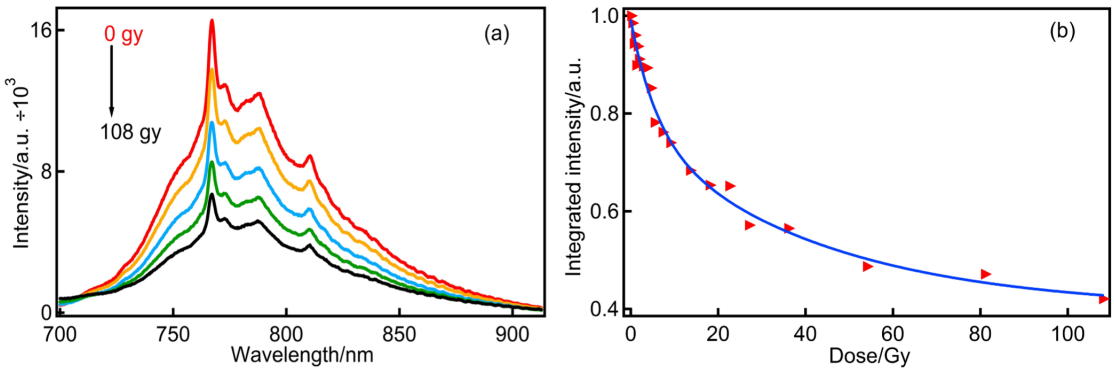

Figure 7.12: (a) X-ray bleaching of the colour centre in nanocrystalline $BaLiF_3$. (b) Normalized integrated luminescence intensity of the colour centre as a function of cumulative X-ray dose. The blue solid line represents a bi-exponential fit function ($I = A_0 + A_1 \exp(-k_1 \times \text{dose}) + A_2 \exp(-k_2 \times \text{dose})$) with fitting parameters $k_1 = 0.02$ Gy^{-1} and $k_2 = 0.17$ Gy^{-1}. The room temperature spectra were excited by a 462 nm laser diode.

7.3.10 Annealing temperature

The photoluminescence intensity of $BaLiF_3$:F_3^+ was found to be highly dependent on the annealing temperature. The room temperature photoluminescence spectra of nanocrystalline $BaLiF_3$ annealed at temperatures between 300 and 800 °C are shown in Figure 7.13a. With

increasing annealing temperature, the F_3^+ centre exhibits an increase in photoluminescence intensity. The maximum signal was obtained at 800 °C (Figure 7.13b) i.e., close to the melting point of $BaLiF_3$. This is most likely based on a change of the microscopic stoichiometry upon annealing leading to a higher concentration of colour centres.

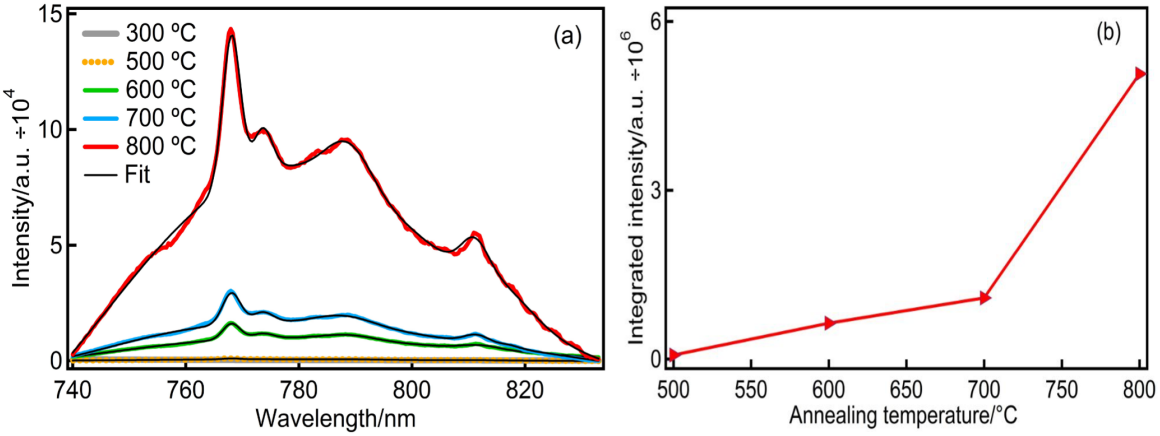

Figure 7.13: (a) Room-temperature photoluminescence spectrum of $BaLiF_3$ after annealing at different temperatures between 300 °C and 800 °C for 2 h under argon. (b) Dependence of the integrated photoluminescence intensity (red line and markers) of the colour centre as a function of annealing temperature. Luminescence spectra were fitted by using a multipeak fit with a Lorentzian line shape assumed for the electronic origin (black solid line).

7.3.11 Stability of the colour centre

To check the stability of the F-aggregate colour centre, annealed $BaLiF_3$ samples were kept in a dark environment or exposed to natural sunlight for several hours (Figure 7.14).

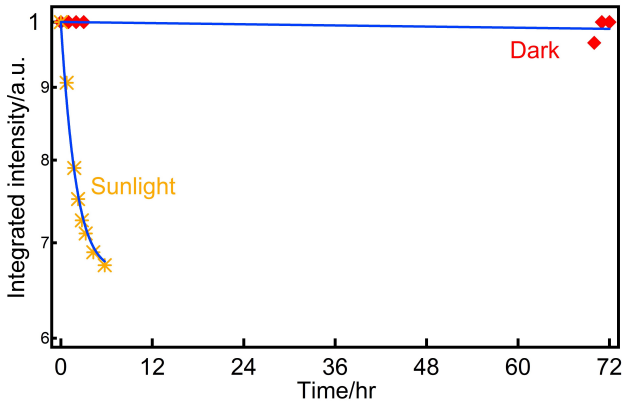

Figure 7.14: Stability of the F_3^+ centre in pure $BaLiF_3$ under different environmental conditions. Red and yellow data sets represent the stability of the colour centre in the dark or under natural sunlight exposure, respectively. Samples were annealed in Ar at 800 °C.

In the dark, the colour centre is stable, and no bleaching is observed over ∼4 days within the experimental accuracy. In contrast, ∼35% bleaching was observed after ∼10 h exposure to natural sunlight. It is noted here that for this experiment the photoluminescence spectra were excited by using low laser power in order to avoid bleaching during the readout process.

7.3.12 Impurity

One of the common features of F-based colour centres is that the presence of any impurities reduces their relative concentrations. This phenomenon is also observed in the present system as shown in Figure 7.15. This figure demonstrates that the intensity of the F_3^+ band decreases when impurity ions (Sm^{3+}, Mn^{2+} Cr^{3+}, Fe^{3+}, Fe^{2+}) and O^{2-} (BaO), are introduced into the $BaLiF_3$ host. Similar behaviour was also observed for the colour centre in alkali halide crystals, which might be because impurity ions act as strong electron or hole traps and have large electron absorption cross-sections.

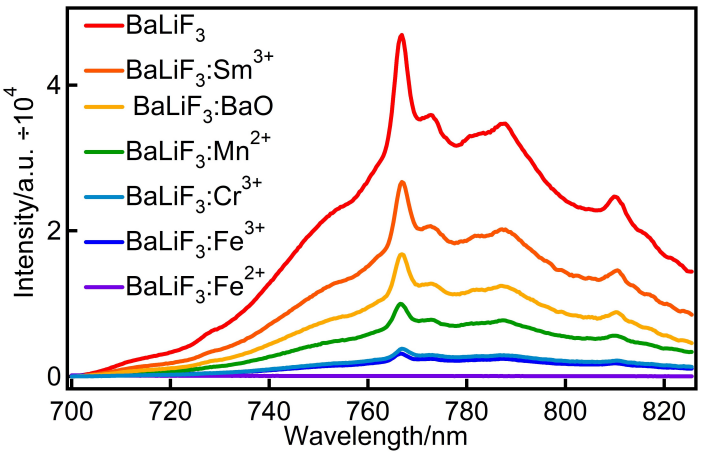

Figure 7.15: Room temperature photoluminescence spectra of F_3^+ in $BaLiF_3$, $BaLiF_3$:Sm^{3+}, $BaLiF_3$:BaO, $BaLiF_3$:Mn^{3+}, $BaLiF_3$:Cr^{3+}, $BaLiF_3$:Fe^{3+} and $BaLiF_3$:Fe^{2+} (traces from top to bottom), respectively. All samples were annealed at 600 °C for 2 h. The concentration of the dopants was 0.27 atom-%.

7.4 Summary

A colour centre was demonstrated in pure $BaLiF_3$ which displayed an electronic origin at 765 nm. This centre consists of three fluoride anion vacancies filled with two electrons. This is the first time the F_3^+ photoluminescence spectrum has been reported. Relatively intense

F_3^+ luminescence was obtained by annealing under Ar, O_2 and air whereas N_2 and H_2 gases act as reducing environments. Due to the relatively weak electron-phonon coupling, the low temperature photoluminescence spectrum (2 K) of $BaLiF_3$:F_3^+ is well-structured with a sharp zero-phonon line at ∼764.8 nm and this origin is still clearly visible at ∼766.9 nm in the room temperature spectrum. The 764.8 nm transition shows a zero-field splitting of 4.2 cm^{-1} at low temperature and the triplet ground state is subjected to Zeeman splitting in the presence of a magnetic field. The relatively long 5 ms luminescence lifetime at 2 K corroborates the spin-forbidden nature of the transition and provides supporting evidence for its assignment to a singlet → triplet emission. The stability of the colour centre in ambient conditions (dark or sunlight) and under X-ray radiation was further explored. The presence of any impurities decreased the concentration of the F_3^+ luminescence.

These results appear to be the first report of F_3^+ colour centre singlet-triplet luminescence with a triplet ground state. The present system has potential in dosimetry and as a nanoscale colour centre lasing medium.

Chapter 8

Conclusion

8.1 Summary and Conclusion

This thesis has investigated luminescence properties and the X-ray storage capability of an interesting host matrix, namely, barium lithium fluoride ($BaLiF_3$) nanocrystals activated with a range of rare-earth ions. Specifically, a detailed preparation and structural and optical characterization of the inverse-perovskite $BaLiF_3$ activated with various rare-earth ions (Sm, Tm, Eu, Er and Yb) and non-activated $BaLiF_3$ has been presented. Furthermore, the radiation (X-ray) storage capability of activated and pure $BaLiF_3$ nanocrystal has been explored using room temperature and low temperature photoluminescence spectroscopy, including photoluminescence in magnetic fields up to 9 T, as well as photoluminescence excitation spectroscopy. In addition, upconversion luminescence spectroscopy of co-doped $BaLiF_3$ has been performed. The research motivation, background and experimental techniques involved in this thesis were presented in **Chapters 1-3**, respectively. The subsequent chapters, including, **Chapter 4, 5, 6, and 7**, investigated the photoluminescence and upconversion luminescence property of singly doped (Sm^{3+} and Tm^{3+}), co-doped (Er^{3+} and Yb^{3+}) and pure $BaLiF_3$ respectively.

Chapter 4 demonstrated the X-ray and UV storage properties of nanocrystalline $BaLiF_3$ (∼36 nm) doped with Sm^{3+} as-synthesized by ball milling. Explicitly, the reduction of Sm^{3+} to Sm^{2+} ions were investigated in the visible range (at 694 nm) by X-ray and UV exposure. It was observed that, in centrosymmetric $BaLiF_3$, the magnetic dipole forbidden Sm^{2+} $^5D_0$ $\rightarrow$ $^7F_0$ transition (at 681 nm) is very weak and the magnetic dipole allowed $^5D_0 \rightarrow {}^7F_1$ Sm^{2+}

transition (at 694 nm) dominates the photoluminescence spectrum. However, an admixture of 20% Sr i.e., $Ba_{0.8}Sr_{0.2}LiF_3:Sm^{3+}$ breaks the symmetry and lowers the local symmetry. As a result, the electric dipole transition $^5D_0 \rightarrow {}^7F_0$ at 681 nm gained intensity. The photoluminescence intensity of Sm^{2+} ions at 694 nm exhibited a gradual increase upon increasing UV and X-irradiation. This indicated that nanocrystalline $BaLiF_3:Sm^{3+}$ is an efficient photoluminescent phosphor. In addition, the lifetime range of Sm^{2+} (694 nm) in the X-ray and UV-irradiated sample was found to be between ∼4 to 12 ms and 19 ms, respectively and the decays are indicative of donor-donor, donor-acceptor and donor-acceptor only energy transfer. The photobleaching process of X-ray induced Sm^{2+} was explained by considering a standard gamma distribution which provided evidence that the Sm^{2+} centres are separated from hole traps by a few interionic spacings of ∼15 Å.

Chapter 5 demonstrated a mechanochemical synthesis route for nanocrystalline $BaLiF_3$ (∼46 nm) doped with trivalent Tm^{3+} along with its X-ray sensitivity before and after X-irradiation. After X-ray exposure, infrared Tm^{2+} ($^2F_{5/2} \rightarrow {}^2F_{7/2}$ transition) emission was observed at 1136 nm. The reverse photobleaching of X-ray induced Tm^{2+} was investigated as a function of excitation power density, indicating a single photoionization process, and an interatomic spacing of ∼17 Å between the Tm^{2+} ions and the hole traps. The X-ray induced Tm^{2+} was found to be relatively stable in the dark but was found to bleach rapidly under exposure to sunlight. These results demonstrated that the infrared emission of Tm^{2+} can be generated in nanocrystalline $BaLiF_3$ upon X-ray exposure which might be useful for solar radiation converter/concentrator applications. The response of nanocrystalline $BaLiF_3:Tm^{3+}$ to X-irradiation was further compared with that of $BaLiF_3:Eu^{3+}$ and $BaLiF_3:Sm^{3+}$ nanocrystals prepared by ball milling. While $BaLiF_3:Tm^{3+}$ exhibited infrared Tm^{2+} emission at 1136 nm, $BaLiF_3:Eu^{3+}$ and $BaLiF_3:Sm^{3+}$ exhibited Eu^{2+} and Sm^{2+} emission at 421 nm and 694 nm, respectively.

Chapter 6 presented the potential of $BaLiF_3$ as a host matrix for the upconversion sensitizer (Yb^{3+})-activator (Er^{3+}) pair as-prepared by ball milling (∼20-30 nm average crystallite size). The dependence of the upconversion luminescence (UCL) was investigated as a function of ball milling time, concentration of dopant (YbF_3) and post-annealing temperature. In particular, the infrared 980 nm-excited upconversion luminescence of $BaLiF_3:Yb^{3+}$, Er^{3+}

samples before and after annealing was investigated and it was demonstrated that the upconversion efficiency was enhanced by 2 orders of magnitudes by the post-annealing treatment. In addition, nanocrystalline $BaLiF_3$:Yb^{3+}, Er^{3+} exhibited clearly visible bright upconversion luminescence after annealing. The UCL signal of $BaLiF_3$:Yb^{3+}, Er^{3+} was compared with that of the well-known $NaYF_4$:Yb^{3+}, Er^{3+} UCL nanophosphor. The X-ray storage capability of $BaLiF_3$:Yb^{3+}, Er^{3+} was explored. It was observed that the photoluminescence intensities of Er^{3+} and Yb^{3+} ions decreased gradually with cumulative X-ray doses due to X-ray-induced reduction of $Er^{3+} \rightarrow Er^{2+}$ and $Yb^{3+} \rightarrow Yb^{2+}$, and as a result, the upconversion luminescence decreased. The gradual increase of Yb^{2+} photoluminescence spectrum was observed upon cumulative X-irradiation. In a novel development, 2D X-ray imaging based on the UCL signal was demonstrated for the first time.

Chapter 7 explored the properties of a unique colour centre in mechanochemically synthesized $BaLiF_3$ that is luminescent at ∼765 nm (2 K) for potential applications in optical data storage, dosimetry and as a solid-state laser. The colour centre is due to the formation of a F_3^+ centre in the fluoride octahedra with three fluoride anion vacancies (3 F^+) filled with two electrons (2 e^-). The F_3^+ band occurred after annealing (≥500 °C) in mechanochemically prepared pristine $BaLiF_3$ and that was characterized by a structured emission with a relatively sharp zero-phonon line at ∼765 nm. Due to the relatively weak electron-phonon coupling, the low temperature photoluminescence spectrum (2 K) of $BaLiF_3$:F_3^+ was well-resolved into the sharp zero-phonon line at ∼764.8 nm and this origin was clearly visible at ∼766.9 nm even at the room temperature. Relatively intense F_3^+ emission was achieved by annealing in Ar, O_2 and air whereas N_2 and H_2 gases acted as reducing environment. The 764.8 nm band illustrated a zero-field splitting at low temperature and exhibited triplet Zeeman splitting in the presence of magnetic field (9 T) which is due to the spin S = 1 in the ground state. The luminescence exhibited a 5 ms long lifetime at 2 K corroborating that it is a forbidden transition (singlet to triplet emission). The colour centre was stable in the dark but photoionized rapidly by natural sunlight and X-irradiation. Additionally, it was observed that the presence of any impurities deceases the concentration of the F_3^+ luminescence. To the best of our knowledge this is the first experimental observation of a F_3^+ colour centre in $BaLiF_3$ which displayed singlet-triplet emission. These results point to a unique optical system for a colour centre-based nano-laser,

applicable in the near-infrared region.

Overall, this thesis presents a detailed understanding of the potential, characteristics, and performance of the inverse-perovskite $BaLiF_3$, and makes significant inroads into the understanding of rare-earth ions (Eu, Sm and Tm, Er and Yb) doped $BaLiF_3$ nanocrystals for a variety of applications such as radiation monitoring systems and X-ray imaging. Specifically, experimental results presented in **Chapter 4** demonstrated the X-ray storage potential of the Sm^{3+} doped $BaLiF_3$ nanophosphor which can be used in dosimetry applications. The utility of $BaLiF_3$ as a potential host matrix was further demonstrated in **Chapter 5** which depicted that luminescence within a broad optical range (e.g., from UV to IR) can be achieved by selecting an appropriate activator, such as Tm, Eu or Sm. Additionally, the X-ray recording capability was demonstrated in **Chapter 6** by using co-doped $BaLiF_3$:Yb^{3+}, Er^{3+} nanophosphor that points to their possible applications in X-ray dosimetry and bioimaging. Finally, **Chapter 7** provided the generation and characteristics of a unique spin forbidden emission from a singlet excited state to a triplet ground state by a F_3^+ colour centre in undoped $BaLiF_3$. The experimental evidence also indicated that the F_3^+ centre has potential for data storage, imaging and dosimetry.

8.2 Future developments

The studies presented in this dissertation advance the current understanding of doped and pristine $BaLiF_3$ nanocrystals for their application as storage phosphor. However, there is still plenty of scope for further investigations such as to improve the storage capability of activated $BaLiF_3$, as suggested below:

1. This thesis mainly investigated activated and non-activated $BaLiF_3$ nanocrystals prepared by ball milling method. However, other synthesis routes, including a co-precipitation method can be adopted to synthesize these nanocrystals, since their performance i.e., the storage capability may critically depend on the specific preparation process as demonstrated for other phosphors [134, 136]. It will provide a direct comparison of the performance of these phosphors which will be useful for their practical applications. Additionally, it is well-established

that incorporation of divalent ions is a key parameter for generation of efficient luminescence [220–222]. Thus, rare-earth ions in their divalent oxidation state such as Eu^{2+}, Sm^{2+} and Tm^{2+} can be doped into the host lattice $BaLiF_3$ and their luminescence and X-ray storage capability could be thoroughly investigated.

2. As shown in **Chapter 7**, the F_3^+ colour centre observed in pure $BaLiF_3$ upon annealing displays a zero-phonon line at near-infrared region, and spectral hole-burning of this line can be the subject of further investigations. In this context, it is important to note that, hole-burning is an optical pumping process that creates a spectral hole/dip in the inhomogeneously broadened transition by depleting the ground state at the laser frequency, a phenomenon that can be due to a range of mechanisms, such as population storage in the excited state (transient hole-burning), slight rearrangements of the surrounding of the resonant centres (non-photochemical hole-burning) or excited state photochemistry e.g. photoionization (photochemical hole-burning) [14, 223]. It is a powerful tool which allows high resolution spectroscopy [132], and may further help to understand the optical data storage potential of the studied F_3^+ centre. It can be assumed that the centre would exhibit photochemical hole-burning via the photoionization process. Recently, Wang et al., [224] performed the room-temperature spectral hole-burning of X-ray induced Sm^{2+} in the $^7F_0 \rightarrow {}^5D_0$ transition in nanocrystalline $Ba_{0.5}Sr_{0.5}FCl_{0.5}Br_{0.5}$:$Sm^{3+}$ prepared by ball milling. Such investigation can be carried out on the F_3^+ transition in $BaLiF_3$ which is important for further development in this field.

3. The understanding of rare-earth ions doped and undoped $BaLiF_3$ presented in this thesis can be further implemented and explored in other host materials, including $BaMgF_4$ [225–227], Cs_2NaYCl_6 [228] and Cs_2NaYF_6 [11]. Such investigations is crucial for the development of new luminescent materials and their optical phenomena may lead to new applications such as quantum information processing.

Appendix

A.1 Powder X-ray diffraction pattern of $BaLiF_3$ doped with SmF_3

The powder X-ray diffraction patterns of $BaLiF_3$:Sm^{3+} as-synthesized by ball milling for different ball milling periods and with different concentration of SmF_3 are displayed in Figure A.1a and A.1b respectively.

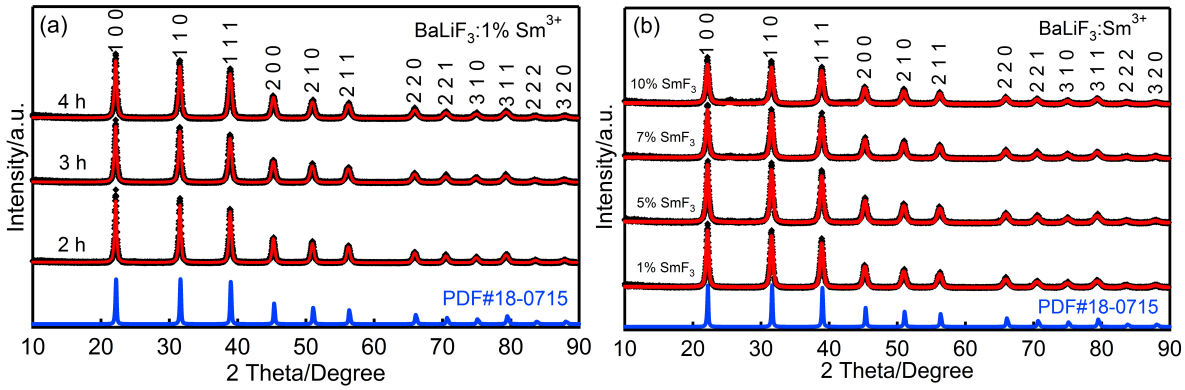

Figure A.1: Powder X-ray diffraction pattern of ball-milled $BaLiF_3$:Sm^{3+} as a function of (a) ball milling time, (b) concentration of SmF_3 along with standard pure $BaLiF_3$ diffraction file (PDF#18-0715). Miller indices of all diffraction peaks are indicated. Rietveld refinements are shown in red solid lines and experimental data are presented in black diamonds

In the X-ray diffraction pattern, all the prominent peaks can be indexed to the pure cubic perovskite structure (space group Pm-3m). This is a clear indication of phase purity of the powder samples obtained by ball milling. From powder X-ray diffraction pattern, it appears

that 3 to 4 hours ball milling is enough for the formation of single phase $BaLiF_3$:1% SmF_3 (Figure A.1a). On the other hand, increasing SmF_3 concentration results diffraction peaks from regent. Particularly, weak residual peaks of BaF_2 is observed for the samples activated with 7% and 10% SmF_3.

A.1.1 Rietveld analysis of XRD pattern

Rietveld analysis of the X-ray diffraction patterns (by MAUD software) is summarized and presented in **Table A.1**.

Table A.1: Summary of Rietveld refinement parameters as obtained from MAUD where R_{wp} and R_{exp} are the weighted-profile R-factor and expected R-factor, respectively. $G = R_{wp}/R_{exp}$ determines the goodness of fit, with $G < 2$ indicating an acceptable refinement.

(a) Ball milling time					
$BaLiF_3$:1% Sm^{3+}					
Ball milling time /h	Lattice parameter /Å	Average crystallite size /nm	R_{wp} %	R_{exp} %	G %
2	4.006 (2)	44 ± 1	18.6	12.9	1.4
3	4.007 (3)	38 ± 1	18.9	13.1	1.4
4	4.006 (3)	37 ± 1	19.6	13.1	1.5
(b) Concentration of SmF_3					
$BaLiF_3$:x% Yb^{3+}, 1% Er^{3+}					
Concentration /mol%	Lattice parameter /Å	Average crystallite size /nm	R_{wp} %	R_{exp} %	G %
1	4.006 (3)	37 ± 1	19.6	13.1	1.5
5	4.005 (3)	30 ± 1	18.9	13.1	1.5
7	4.006 (3)	28 ± 1	19.8	13.1	1.5
10	4.006 (4)	25 ± 1	22.7	13.0	1.5
(c) Undoped $BaLiF_3$					
$BaLiF_3$:1% Yb^{3+}, 1% Er^{3+}					
Ball milling time /h	Lattice parameter /Å	Average crystallite size /nm	R_{wp} %	R_{exp} %	G %
3	4.008 (2)	50 ± 1	20	13	1.5

It illustrates that the powder samples prepared by ball milling for 2 hours to 4 hours yields an average crystallite size of 44 ± 1 nm to 37 ± 1 nm respectively. It is found that pro-longed ball milling reduces the average crystallite size. Similarly, increasing dopant concentration (1% -

10%) also plays an important role to decrease the crystallite size (37 ± 1 nm to 25 ± 2 nm) due to the presence of significant concentration of SmF_3 into the host lattice.

For comparison, Rietveld analysis of undoped $BaLiF_3$ prepared by following same preparation method and conditions is presented in **Table A.1**. It illustrates the average size of the crystallites for undoped sample is ∼50 ± 1 nm, whereas that is ∼ 38 ± 1 for $BaLiF_3$:1% SmF_3.

A.2 X-ray sensitivity

The X-ray sensitivity of $BaLiF_3$:1 mol% SmF_3 prepared by ball milling for 2 to 4 hours is compared in Figure A.2a.

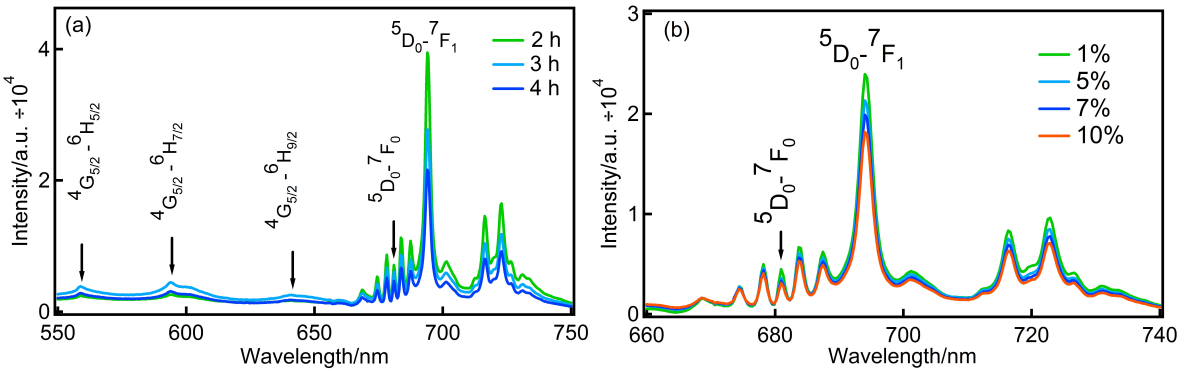

Figure A.2: (a) Evolution of Sm^{2+} $^5D_0 \rightarrow {}^7F_1$ transition at 694 nm as a function of increasing periods of ball milling. (b) Ball-milled $BaLiF_3$ activated with x% Sm^{3+} (x = 1 mol%, 5 mol%, 7 mol% and 10 mol%) after X-irradiation in the region of Sm^{2+} $^5D_0 \rightarrow {}^7F_1$ transition. All samples were initially exposed to 9 Gy of X-ray and the room temperature photoluminescence spectra were excited at 462 nm.

It appears from this experiment that in contrast to the sample ball-milled for 3 and 4 hours, 2 hours ball-milled sample contains significant amount of Sm^{2+} after X-irradiation. This clearly indicates that pro-longed ball milling reduces the X-ray storage capability which is due to the incorporation of more defects into the system and also because of the uniform distribution of Sm^{3+} ions throughout the crystallites. It is also possible that smaller particle size reduces the luminescence properties of nanocrystalline $BaLiF_3$:1 mol% SmF_3.

The X-ray storage efficiency of $BaLiF_3$:1 mol% Sm^{3+}, $BaLiF_3$:5 mol% Sm^{3+}, $BaLiF_3$:7 mol% Sm^{3+} and $BaLiF_3$:10 mol% Sm^{3+} nanocrystals prepared after 4 hours ball milling is further

investigated (Figure A.2b). It follows from this demonstration that with increasing amount of defect centres (1 - 10 mol% SmF_3) the luminescence intensity of Sm^{2+} $^5D_0 \rightarrow {}^7F_1$ decreases. Specifically, the sample contains 1 mol% SmF_3 exhibits maximum luminescence.

A.3 Post-annealing effect on X-ray reduction

The reduction of Sm^{3+} to Sm^{2+} in $BaLiF_3$ activated with 1 mol% Sm^{3+} is observed further upon annealing in air (Figure A.3).

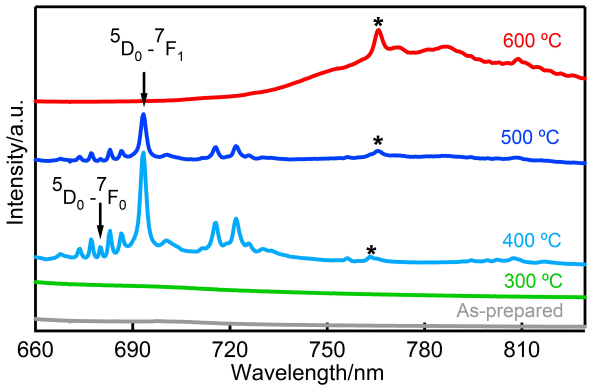

Figure A.3: Room temperature photoluminescence spectra of ball-milled $BaLiF_3$:1 mol% Sm^{3+} before and after annealing at different temperatures from 300 to 600 °C for 1 h in air. Luminescence spectra were excited by a 462 nm laser diode. All the prominent transitions are labeled and the development of a defect with increasing annealing temperature is denoted by ($\star$)

It appears that at 400 °C the conversion of $Sm^{3+} \rightarrow Sm^{2+}$ occurs and the photoluminescence intensity of Sm^{2+} ($^5D_0 \rightarrow {}^7F_1$) transition at 694 nm reaches to a maximum. However, the luminescence intensity of the Sm^{2+} ions decreases when the annealing temperature is raised to 500 °C and finally for the sample annealed at 600 °C, no Sm^{2+} emission is observed. This is due to the progression of a defect centre at 768 nm into the host lattice upon increasing annealing temperature. In fact, the existence of the defect is visible in 400 °C annealed sample however it starts to become prominent at 500 °C which effect the conversion process by decreasing the Sm^{2+} luminescence intensity. At 600 °C, only the defect centre is visible in the photoluminescence spectra. This experimental result signifies that heat treatment on $BaLiF_3$:Sm^{3+} phosphor (500 °C) activates a defect centre into the host which fades the Sm^{2+} luminescence.

Bibliography

[1] D. S. Brettle, A. Workman, R. P. Ellwood, J. H. Launders, K. Horner, and R. M. Davies, "The imaging performance of a storage phosphor system for dental radiography," *The British Journal of Radiology*, vol. 69, no. 819, pp. 256–261, 1996.

[2] E. Samei and M. J. Flynn, "An experimental comparison of detector performance for direct and indirect digital radiography systems," *Medical Physics*, vol. 30, no. 4, pp. 608–622, 2003.

[3] M. J. Yaffe and J. A. Rowlands, "X-ray detectors for digital radiography," *Physics in Medicine & Biology*, vol. 42, no. 1, p. 1, 1997.

[4] R. F. Mould, "The early history of X-ray diagnosis with emphasis on the contributions of physics 1895-1915," *Physics in Medicine & Biology*, vol. 40, no. 11, p. 1741, 1995.

[5] J. M. Spaeth, "Recent developments in X-ray storage phosphor materials," *Radiation Measurements*, vol. 33, no. 5, pp. 527–532, 2001.

[6] J. A. Rowlands, "The physics of computed radiography," *Physics in Medicine & Biology*, vol. 47, no. 23, p. R123, 2002.

[7] J. Freudenberger, E. Hell, and W. Knüpfer, "Perspectives of medical X-ray imaging," *Nuclear Instruments and Methods in Physics Research Section A: Accelerators, Spectrometers, Detectors and Associated Equipment*, vol. 466, no. 1, pp. 99–104, 2001.

[8] A. Hessenbruch, "X-rays for medical use," *Physics Education*, vol. 30, no. 6, p. 347, 1995.

[9] H. MacMahon, S. Sanada, K. Doi, M. Giger, X. W. Xu, F. F. Yin, S. M. Montner,

and M. Carlin, "Direct comparison of conventional and computed radiography with a dual-image recording technique." *Radiographics*, vol. 11, no. 2, pp. 259–268, 1991.

[10] W. Huda, L. N. Rill, D. K. Benn, and J. C. Pettigrew, "Comparison of a photostimulable phosphor system with film for dental radiology," *Oral Surgery, Oral Medicine, Oral Pathology, Oral Radiology, and Endodontology*, vol. 83, no. 6, pp. 725–731, 1997.

[11] J. M. Spaeth, T. Hangleiter, F. K. Koschnick, and T. Pawlik, "X-ray storage phosphors," *Radiation Effects and Defects in Solids*, vol. 135, no. 1-4, pp. 1–10, 1995.

[12] S. Schweizer, "Physics and current understanding of X-ray storage phosphors," *Physica Status Solidi (a)*, vol. 187, no. 2, pp. 335–393, 2001.

[13] M. Sonoda, M. Takano, J. Miyahara, and H. Kato, "Computed radiography utilizing scanning laser stimulated luminescence," *Radiology*, vol. 148, no. 3, pp. 833–838, 1983.

[14] Z. Liu, "Spectroscopy of a Samarium (iii) activated X-ray storage phosphor," Ph.D. dissertation, University of New South Wales, Canberra, School of Physical, Environmental & Mathematical Sciences, 2012.

[15] H. von Seggern, "X-ray imaging with photostimulable phosphors," *Nuclear Instruments and Methods in Physics Research Section A: Accelerators, Spectrometers, Detectors and Associated Equipment*, vol. 322, no. 3, pp. 467–471, 1992.

[16] I. Kashima, "Computed radiography with photostimulable phosphor in oral and maxillofacial radiology," *Oral Surgery, Oral Medicine, Oral Pathology, Oral Radiology, and Endodontology*, vol. 80, no. 5, pp. 577–598, 1995.

[17] R. S. Eachus, R. H. D. Nuttall, M. T. Olm, W. G. McDugle, F. K. Koschnick, T. Hangleiter, and J.-M. Spaeth, "Oxygen defects in BaFBr and BaFCl," *Physical Review B*, vol. 52, no. 6, p. 3941, 1995.

[18] H. V. Seggern, "Photostimulable X-ray storage phosphors: a review of present understanding," *Brazilian Journal of Physics*, vol. 29, pp. 254–268, 1999.

[19] A. R. Cowen, A. Workman, and J. S. Price, "Physical aspects of photostimulable phosphor computed radiography," *The British Journal of Radiology*, vol. 66, no. 784, pp. 332–345, 1993.

[20] L. Bøtter-Jensen, S. W. S. McKeever, and A. G. Wintle, *Optically stimulated luminescence dosimetry.* Elsevier, 2003.

[21] G. J. Heyes, A. J. Mill, and M. W. Charles, "Enhanced biological effectiveness of low energy X-rays and implications for the UK breast screening programme," *The British Journal of Radiology*, vol. 79, no. 939, pp. 195–200, 2006.

[22] A. B. de Gonzalez and S. Darby, "Risk of cancer from diagnostic X-rays: estimates for the UK and 14 other countries," *The Lancet*, vol. 363, no. 9406, pp. 345–351, 2004.

[23] K. Takahashi, K. Kohda, J. Miyahara, Y. Kanemitsu, K. Amitani, and S. Shionoya, "Mechanism of photostimulated luminescence in BaFX:Eu^{2+} (X = Cl, Br) phosphors," *Journal of Luminescence*, vol. 31, pp. 266–268, 1984.

[24] K. Takahashi, "Progress in science and technology on photostimulable BaFX:Eu^{2+} (X = Cl, Br, I) and imaging plates," *Journal of Luminescence*, vol. 100, no. 1-4, pp. 307–315, 2002.

[25] H. Riesen and Z. Liu, *Optical storage phosphors and materials for ionizing radiation. Current Topics in Ionizing Radiation Research (Ed. Nenoi, M.).* (InTech), 2012.

[26] H. H. Rüter, H. Seggern, R. Reininger, and V. Saile, "Creation of photostimulable centers in BaFBr:Eu^{2+} single crystals by vacuum ultraviolet radiation," *Physical Review Letters*, vol. 65, no. 19, p. 2438, 1990.

[27] A. R. Cowen, A. G. Davies, and S. M. Kengyelics, "Advances in computed radiography systems and their physical imaging characteristics," *Clinical Radiology*, vol. 62, no. 12, pp. 1132–1141, 2007.

[28] B. Mijnheer, "State of the art of in vivo dosimetry," *Radiation Protection Dosimetry*, vol. 131, no. 1, pp. 117–122, 2008.

[29] H. P. Busch and K. Faulkner, "Image quality and dose management in digital radiography: a new paradigm for optimisation," *Radiation Protection Dosimetry*, vol. 117, no. 1-3, pp. 143–147, 2005.

[30] M. Ishii and M. Kobayashi, "Single crystals for radiation detectors," *Progress in Crystal Growth and Characterization of Materials*, vol. 23, pp. 245–311, 1992.

[31] W. Gellermann, "Color center lasers," *Journal of Physics and Chemistry of Solids*, vol. 52, no. 1, pp. 249–297, 1991.

[32] G. A. Appleby, A. Edgar, and G. V. M. Williams, "Structure and photostimulated luminescent properties of Eu-doped M_2BaX_4 (M = Cs, Rb; X = Br, Cl)," *Journal of Applied Physics*, vol. 96, no. 11, pp. 6281–6285, 2004.

[33] J. Grimm and H. U. Güdel, "Five different types of spontaneous emission simultaneously observed in Tm^{2+} doped $CsCaBr_3$," *Chemical Physics Letters*, vol. 404, no. 1-3, pp. 40–43, 2005.

[34] J. Grimm, J. F. Suyver, E. Beurer, G. Carver, and H. U. Güdel, "Light-emission and excited-state dynamics in Tm^{2+} doped $CsCaCl_3$, $CsCaBr_3$, and $CsCaI_3$," *The Journal of Physical Chemistry B*, vol. 110, no. 5, pp. 2093–2101, 2006.

[35] S. L. Baldochi, A. M. E. Santo, E. Martins, M. Duarte, M. M. F. Vieira, J. N. D. Vieira, and S. P. Morato, "Growth and characterization of $BaLiF_3$:TM (Ni^{2+}, Co^{2+}) for laser applications," *Journal of Crystal Growth*, vol. 166, no. 1-4, pp. 375–379, 1996.

[36] Q. Qiang, W. Chen, X. Ma, and Y. Wang, "The crystal structure and upconversion properties of Yb^{3+}, Er^{3+}/Ho^{3+} codoped $BaLiF_3$ microcrystals with different morphologies," *Dalton Transactions*, vol. 44, no. 13, pp. 6242–6248, 2015.

[37] M. A. Dubinskii, K. L. Schepler, V. V. Semashko, R. Y. Abdulsabirov, B. M. Galjautdinov, S. L. Korableva, and A. K. Naumov, "Ce^{3+}:$LiBaF_3$ as new prospective active material for tunable UV laser with direct UV pumping." in *Advanced Solid State Lasers*. Optical Society of America, 1997, p. US9.

[38] C. R. Ronda, T. Jüstel, and H. Nikol, "Rare earth phosphors: fundamentals and applications," *Journal of Alloys and Compounds*, vol. 275, pp. 669–676, 1998.

[39] G. Blasse and B. C. Grabmaier, "A general introduction to luminescent materials," in *Luminescent Materials*. Springer, Berlin, 1994, pp. 1–9.

[40] B. Valeur and J. C. Brochon, *New trends in fluorescence spectroscopy: applications to chemical and life sciences*. Springer Science & Business Media, 2012, vol. 1.

[41] F. Auzel, "Upconversion and anti-stokes processes with f and d ions in solids," *Chemical Reviews*, vol. 104, no. 1, pp. 139–174, 2004.

[42] J. Zhou, Q. Liu, W. Feng, Y. Sun, and F. Li, "Upconversion luminescent materials: advances and applications," *Chemical Reviews*, vol. 115, no. 1, pp. 395–465, 2015.

[43] T. Aoki, "Photoluminescence spectroscopy," *Characterization of Materials*, pp. 1–12, 2002.

[44] A. Meijerink, W. J. Schipper, and G. Blasse, "Photostimulated luminescence and thermally stimulated luminescence of Y_2SiO_5-Ce, Sm," *Journal of Physics D: Applied Physics*, vol. 24, no. 6, p. 997, 1991.

[45] T. Hangleiter, F. K. Koschnick, J. M. Spaeth, R. H. D. Nuttall, and R. S. Eachus, "Temperature dependence of the photostimulated luminescence of X-irradiate BaFBr:Eu^{2+}," *Journal of Physics: Condensed Matter*, vol. 2, no. 32, p. 6837, 1990.

[46] D. Chen, Y. Yu, F. Huang, P. Huang, A. Yang, Z. Wang, and Y. Wang, "Monodisperse upconversion Er^{3+}/Yb^{3+}: MFCl (M = Ca, Sr, Ba) nanocrystals synthesized via a seed-based chlorination route," *Chemical Communications*, vol. 47, no. 39, pp. 11 083–11 085, 2011.

[47] M. Ding, D. Chen, T. Chen, C. Lu, Y. Ni, and Z. Xu, "Hydrothermal synthesis and upconversion luminescence properties of BaFCl:Yb^{3+}/Er^{3+} microhseets," *Materials Letters*, vol. 128, pp. 101–104, 2014.

[48] K. T. Dissanayake and F. A. Rabuffetti, "Infrared-to-visible upconversion luminescence in Er:Yb:SrFBr nanocrystals," *Journal of Materials Chemistry C*, vol. 4, no. 13, pp. 2447–2451, 2016.

[49] J. Zhou, G. Chen, Y. Zhu, L. Huo, W. Mao, D. Zou, X. Sun, E. Wu, H. Zeng, J. Zhang, L. Zhang, J. Qiu, and S. Xu, "Intense multiphoton upconversion of Yb^{3+}-Tm^{3+} doped β-$NaYF_4$ individual nanocrystals by saturation excitation," *Journal of Materials Chemistry C*, vol. 3, no. 2, pp. 364–369, 2015.

[50] F. Wang and X. Liu, "Recent advances in the chemistry of lanthanide-doped upconversion nanocrystals," *Chemical Society Reviews*, vol. 38, no. 4, pp. 976–989, 2009.

[51] M. Haase and H. Schäfer, "Upconverting nanoparticles," *Angewandte Chemie International Edition*, vol. 50, no. 26, pp. 5808–5829, 2011.

[52] J. S. Chivian, W. E. Case, and D. D. Eden, "The photon avalanche: A new phenomenon in Pr^{3+}-based infrared quantum counters," *Applied Physics Letters*, vol. 35, no. 2, pp. 124–125, 1979.

[53] L. D. Carlos, R. A. S. Ferreira, V. de Zea Bermudez, B. Julian-Lopez, and P. Escribano, "Progress on lanthanide-based organic-inorganic hybrid phosphors," *Chemical Society Reviews*, vol. 40, no. 2, pp. 536–549, 2011.

[54] X. Qin, X. Liu, W. Huang, M. Bettinelli, and X. Liu, "Lanthanide-activated phosphors based on 4f-5d optical transitions: theoretical and experimental aspects," *Chemical Reviews*, vol. 117, no. 5, pp. 4488–4527, 2017.

[55] T. Moeller, *The Chemistry of the Lanthanides: Pergamon Press: Oxford, U.K.* Elsevier, 2013, vol. 26.

[56] J. W. M. Verwey, G. J. Dirksen, and G. Blasse, "The luminescence of divalent and trivalent rare earth ions in the crystalline and glass modifications of SrB_4O_7," *Journal of Physics and Chemistry of Solids*, vol. 53, no. 3, pp. 367–375, 1992.

[57] B. G. Wybourne, *Spectroscopic properties of rare earths.* Wiley, New York, 1965.

[58] W. T. Carnall, P. R. Fields, and K. Rajnak, "Spectral intensities of the trivalent lanthanides and actinides in solution. I. Pr^{3+}, Nd^{3+}, Er^{3+}, Tm^{3+}, and Yb^{3+}," *The Journal of Chemical Physics*, vol. 49, no. 10, pp. 4424–4442, 1968.

[59] P. Pal, "Photophysical properties of Samarium (II) doped in inorganic crystals: effect of chemical environment, external pressure and temperature," Ph.D. dissertation. [Online]. Available: https://archive-ouverte.unige.ch/unige:24868

[60] L. R. Morss, "Thermochemical properties of yttrium, lanthanum, and the lanthanide elements and ions," *Chemical Reviews*, vol. 76, no. 6, pp. 827–841, 1976.

[61] G. Meyer, "Reduced halides of the rare-earth elements," *Chemical Reviews*, vol. 88, no. 1, pp. 93–107, 1988.

[62] E. Loh, "$4f^n \rightarrow 4f^{n-1}5d$ absorption spectra of rare-earth ions," *Physical Review Letters*, vol. 175, no. 2, pp. 533–536, 1968.

[63] W. T. Carnall, G. L. Goodman, K. Rajnak, and R. S. Rana, "A systematic analysis of the spectra of the lanthanides doped into single crystal LaF_3," *The Journal of Chemical Physics*, vol. 90, no. 7, pp. 3443–3457, 1989.

[64] G. F. Imbusch and R. Kopelman, "Optical spectroscopy of electronic centers in solids," in *Laser spectroscopy of solids*. Springer, 1981, pp. 1–37.

[65] A. S. M. M. Alam and B. D. Bartolo, "Thermal dependence of fluorescence and lifetimes of Sm^{2+} in several host lattices," *The Journal of Chemical Physics*, vol. 47, no. 10, pp. 3790–3801, 1967.

[66] M. Secu, L. Matei, T. Serban, E. Apostol, G. Aldica, and C. Silion, "Preparation and optical properties of BaFCl:Eu^{2+} X-ray storage phosphor," *Optical Materials*, vol. 15, no. 2, pp. 115–122, 2000.

[67] P. P. Sorokin, M. J. Stevenson, J. R. Lankard, and G. D. Pettit, "Spectroscopy and optical maser action in SrF_2:Sm^{2+}," *Physical Review*, vol. 127, no. 2, p. 503, 1962.

[68] K. Tanaka, S. Okamoto, Y. Kanemitsu, and T. Kushida, "Reversible photochromic processes in BaClF:Sm^{2+}," *Journal of Luminescence*, vol. 94, pp. 519–522, 2001.

[69] J. Wang, Y. Huang, Y. Li, and H. J. Seo, "The reduction and luminescence characteristics of Sm^{2+} doped in $Ba_3BP_3O_{12}$ crystal," *Journal of the American Ceramic Society*, vol. 94, no. 5, pp. 1454–1459, 2011.

[70] B. W. Bryant, "Spectra of doubly and triply ionized ytterbium, Yb_{III} and Yb_{IV}," *Journal of the Optical Society of America*, vol. 55, no. 7, pp. 771–779, 1965.

[71] A. Boumriche, J. Y. Gesland, A. Bulou, M. Rousseau, J. L. Fourquet, and B. Hennion, "Structure and dynamics of the inverted perovskite $BaLiF_3$," *Solid State Communications*, vol. 91, no. 2, pp. 125–128, 1994.

[72] D. Wiedemann, F. Meutzner, O. Fabelo, and S. Ganschow, "The inverse perovskite $BaLiF_3$: single-crystal neutron diffraction and analyses of potential ion pathways," *Acta Crystallographica Section B: Structural Science, Crystal Engineering and Materials*, vol. 74, no. 6, pp. 643–650, 2018.

[73] T. Yi, W. Chen, L. Cheng, R. D. Bayliss, F. Lin, M. R. Plews, D. Nordlund, M. M. Doeff, K. A. Persson, and J. Cabana, "Investigating the intercalation chemistry of alkali ions in fluoride perovskites," *Chemistry of Materials*, vol. 29, no. 4, pp. 1561–1568, 2017.

[74] R. D. Shannon, "Revised effective ionic radii and systematic studies of interatomic distances in halides and chalcogenides," *Acta Crystallographica Section A: Crystal Physics, Diffraction, Theoretical and General Crystallography*, vol. 32, no. 5, pp. 751–767, 1976.

[75] M. A. Pena and J. L. G. Fierro, "Chemical structures and performance of perovskite oxides," *Chemical Reviews*, vol. 101, no. 7, pp. 1981–2018, 2001.

[76] V. M. Goldschmidt, "Die gesetze der krystallochemie," *Naturwissenschaften*, vol. 14, no. 21, pp. 477–485, 1926.

[77] A. Düvel, M. Wilkening, R. Uecker, S. Wegner, V. Šepelák, and P. Heitjans, "Mechanosynthesized nanocrystalline $BaLiF_3$: The impact of grain boundaries and struc-

tural disorder on ionic transport," *Physical Chemistry Chemical Physics*, vol. 12, no. 37, pp. 11 251–11 262, 2010.

[78] H. Riesen and W. A. Kaczmarek, "Efficient X-ray generation of Sm^{2+} in nanocrystalline $BaFCl/Sm^{3+}$: a photoluminescent X-ray storage phosphor," *Inorganic Chemistry*, vol. 46, no. 18, pp. 7235–7237, 2007.

[79] A. Bensalah, K. Shimamura, T. Fujita, H. Sato, M. Nikl, and T. Fukuda, "Growth and characterization of $BaLiF_3$ single crystal as a new optical material in the VUV region," *Journal of Alloys and Compounds*, vol. 348, no. 1-2, pp. 258–262, 2003.

[80] C. E. Andersen, S. K. Nielsen, S. Greilich, J. Helt-Hansen, J. C. Lindegaard, and K. Tanderup, "Characterization of a fiber-coupled luminescence dosimetry system for online in vivo dose verification during brachytherapy," *Medical Physics*, vol. 36, no. 3, pp. 708–718, 2009.

[81] G. Dhanaraj, K. Byrappa, V. Prasad, and M. Dudley, *Springer handbook of crystal growth*. Springer Science & Business Media, 2010.

[82] S. L. Baldochi and J. Y. Gesland, "Crystal growth of pure and lead doped barium-lithium fluoride," *Materials Research Bulletin*, vol. 27, no. 7, pp. 891–900, 1992.

[83] V. A. Bron, "Some crystal-chemical relationships in the activated sintering of highly refractory oxides in the solid phase," *Soviet Powder Metallurgy and Metal Ceramics*, vol. 1, no. 5, pp. 339–344, 1964.

[84] L. D. B. Arceo, J. J. Cruz-Rivera, J. G. Cabañas-Moreno, M. U. K. Tsuchiya, and H. A. Calderón, "Characterization of Cu-Co alloys produced by mechanosynthesis and spark plasma sintering," in *Journal of Metastable and Nanocrystalline Materials*, vol. 8. Trans Tech Publ, 2000, pp. 641–648.

[85] R. G. Bernard, "Processes involved in sintering," *Powder Metallurgy*, vol. 2, no. 3, pp. 86–103, 1959.

[86] F. Thümmler and W. Thomma, "The sintering process," *Metallurgical Reviews*, vol. 12, no. 1, pp. 69–108, 1967.

[87] S. L. James, C. J. Adams, C. Bolm, P. Carsten, T. Friščić, F. Grepioni, K. D. M. Harris, G. Hyett, W. Jones, A. Krebs, J. Mack, L. Maini, A. G. Orpen, I. P. Parkin, W. C. Shearouse, J. W. Steed, and D. C. Waddell, "Mechanochemistry: opportunities for new and cleaner synthesis," *Chemical Society Reviews*, vol. 41, no. 1, pp. 413–447, 2012.

[88] K. D. M. Harris, "How grinding evolves," *Nature Chemistry*, vol. 5, no. 1, pp. 12–14, 2013.

[89] V. V. Boldyrev and K. Tkáčová, "Mechanochemistry of solids: past, present, and prospects," *Journal of Materials Synthesis and Processing*, vol. 8, no. 3, pp. 121–132, 2000.

[90] V. V. Boldyrev, "Mechanochemistry and mechanical activation of solids," *Russian Chemical Reviews*, vol. 75, no. 3, p. 177, 2006.

[91] E. G. Avvakumov, E. G. Avvakumov, G. V. Avvakumov, M. Senna, and N. V. Kosova, *Soft mechanochemical synthesis: a basis for new chemical technologies*. Springer Science & Business Media, 2001.

[92] C. Suryanarayana, "Mechanical alloying and milling," *Progress in materials science*, vol. 46, no. 1-2, pp. 1–184, 2001.

[93] T. Friscic and W. Jones, "Recent advances in understanding the mechanism of cocrystal formation via grinding," *Crystal Growth and Design*, vol. 9, no. 3, pp. 1621–1637, 2009.

[94] L. Takacs, "The mechanochemical reduction of AgCl with metals," *Journal of Thermal Analysis and Calorimetry*, vol. 90, no. 1, pp. 81–84, 2007.

[95] L. M. Kubalova, V. I. Fadeeva, I. A. Sviridov, and S. A. Fedotov, "The synthesis of nanocrystalline $Ni_{75}Nb_{12}B_{13}$ alloys by high energy ball milling of elemental components," *Journal of alloys and compounds*, vol. 483, no. 1-2, pp. 86–88, 2009.

[96] V. E. Oliker, V. L. Sirovatka, T. Y. Gridasova, I. I. Timofeeva, and A. I. Bykov, "Mechanochemical synthesis and structure of Ti-Al-B-based alloys," *Powder Metallurgy and Metal Ceramics*, vol. 47, no. 9, pp. 546–556, 2008.

[97] M. Karolus, E. Jartych, and D. Oleszak, "Structure and magnetic properties of nanocrystalline Fe-Mo alloys prepared by mechanosynthesis," *Acta Physica Polonica A*, vol. 2, no. 102, pp. 253–258, 2002.

[98] M. H. Medina and G. A. P. Alcázar, "Structural and magnetic properties of $Fe_{0.45}Mn_{0.25}Al_{0.30}$ alloys prepared by mechanical alloying," *Physica Status Solidi (b)*, vol. 243, no. 6, pp. 1390–1399, 2006.

[99] T. Takatoshi, Q. Zhang, and F. Sait, "Mechanochemical synthesis of rutile-type $CrMO_4$ (M = V, Sb) and their solid solutions," *Journal of Solid State Chemistry*, vol. 179, no. 2, pp. 433–437, 2006.

[100] T. Takatoshi, Q. Zhang, and F. Saito, "Mechanochemical synthesis of rare earth orthovanadates from R_2O_3 (R = rare earth elements) and V_2O_5 powders," *Journal of Alloys and Compounds*, vol. 427, no. 1-2, pp. 219–222, 2007.

[101] Q. Zhang, J. Lu, and F. Saito, "Mechanochemical synthesis of $LaCrO_3$ by grinding constituent oxides," *Powder Technology*, vol. 122, no. 2-3, pp. 145–149, 2002.

[102] I. Szafraniak-Wiza, B. Hilczer, A. Pietraszko, and E. Talik, "Phase formations during mechanochemical synthesis of $PbTiO_3$," *Journal of Electroceramics*, vol. 20, no. 1, pp. 21–25, 2008.

[103] V. Nachbaur, G. Tauvel, T. Verdier, M. Jean, J. Juraszek, and D. Houvet, "Mecanosynthesis of partially inverted zinc ferrite," *Journal of Alloys and Compounds*, vol. 473, no. 1-2, pp. 303–307, 2009.

[104] H. Yang, X. Zhang, W. Ao, and G. Qiu, "Formation of $NiFe_2O_4$ nanoparticles by mechanochemical reaction," *Materials Research Bulletin*, vol. 39, no. 6, pp. 833–837, 2004.

[105] G. Ye and T. Troczynski, "Mechanochemical activation-assisted low-temperature synthesis of $CaZrO_3$," *Journal of the American Ceramic Society*, vol. 90, no. 1, pp. 287–290, 2007.

[106] A. Gajović, I. Djerdj, K. Furić, R. Schlögl, and D. S. Su, "Preparation of nanostructured $ZrTiO_4$ by solid state reaction in equimolar mixture of TiO_2 and ZrO_2," *Crystal Research and Technology: Journal of Experimental and Industrial Crystallography*, vol. 41, no. 11, pp. 1076–1081, 2006.

[107] A. Mergen, "Mechanochemical synthesis of $MgTa_2O_6$ ceramic," *Ceramics International*, vol. 35, no. 3, pp. 1151–1157, 2009.

[108] P. Ferrer, J. E. Iglesias, A. P. Ayala, I. Guedes, and A. Castro, "Study of the aurivillius phases $Bi_4Sr_{n-3}Ti_nO_{3n+3}$ (n = 4, 5) synthesized by mechanochemical activation," *Solid State Communications*, vol. 136, no. 11-12, pp. 621–626, 2005.

[109] A. A. Cristóbal, E. F. Aglietti, M. S. Conconi, and J. M. P. López, "Structural alterations during mechanochemical activation of a titanium-magnetite mixture," *Materials Chemistry and Physics*, vol. 111, no. 2-3, pp. 341–345, 2008.

[110] V. Šepelák, I. Bergmann, A. Diekmann, P. Heitjans, and K. D. Becker, "Mechanosynthesis of nanocrystalline iron germanate Fe_2GeO_4 with a nonequilibrium cation distribution," *Reviews on Advanced Materials Science*, vol. 18, no. 4, pp. 349–352, 2008.

[111] P. M. Botta, E. F. Aglietti, and J. M. P. López, "Kinetic study of $ZnFe_2O_4$ formation from mechanochemically activated Zn-Fe_2O_3 mixtures," *Materials Research Bulletin*, vol. 41, no. 4, pp. 714–723, 2006.

[112] L. N. Patro and K. Hariharan, "Frequency dependent conduction characteristics of mechanochemically synthesized $NaSn_2F_5$," *Materials Science and Engineering: B*, vol. 162, no. 3, pp. 173–178, 2009.

[113] Y. Yamane, K. Yamada, and K. Inoue, "Mechanochemical synthesis and order-disorder phase transition in fluoride ion conductor $RbPbF_3$," *Solid State Ionics*, vol. 179, no. 17-18, pp. 605–610, 2008.

[114] M. M. Ahmad, Y. Yamane, K. Yamada, and S. Tanaka, "Dielectric relaxation properties of $Pb_{1-x}Sn_xF_2$ solid solutions prepared by mechanochemical milling," *Journal of Physics D: Applied Physics*, vol. 40, no. 19, p. 6020, 2007.

[115] R. H. Pawelke, M. Felderhoff, C. Weidenthaler, B. Bogdanovic, and F. Schueth, "Mechanochemical synthesis of ternary potassium transition metal chlorides," *Zeitschrift für Anorganische und Allgemeine Chemie*, vol. 635, no. 2, pp. 265–270, 2009.

[116] V. Manivannan, P. Parhi, and J. W. Kramer, "Metathesis synthesis and characterization of complex metal fluoride, KMF_3 (M = Mg, Zn, Mn, Ni, Cu and Co) using mechanochemical activation," *Bulletin of Materials Science*, vol. 31, no. 7, pp. 987–993, 2008.

[117] J. Lee, H. Shin, J. Lee, H. Chung, Q. Zhang, and F. Saito, "Mechanochemical syntheses of perovskite $KM^{II}F_3$ with cubic structure (M^{II}= Mg, Ca, Mn, Fe, Co, Ni, and Zn)," *Materials Transactions*, vol. 44, no. 7, pp. 1457–1460, 2003.

[118] A. Düvel, S. Wegner, K. Efimov, A. Feldhoff, P. Heitjans, and M. Wilkening, "Access to metastable complex ion conductors via mechanosynthesis: preparation, microstructure and conductivity of (Ba, Sr)LiF_3 with inverse perovskite structure," *Journal of Materials Chemistry*, vol. 21, no. 17, pp. 6238–6250, 2011.

[119] B. Nensel, P. Thielemann, and G. Decker, "Are storage phosphors a useful tool for soft X-ray imaging diagnostics? spectral sensitivity and spatial resolution in the 0.07 to 14 nm range," *Journal of Applied Physics*, vol. 83, no. 4, pp. 2276–2281, 1998.

[120] H. V. Seggern, T. Voigt, W. Knüpfer, and G. Lange, "Physical model of photostimulated luminescence of X-ray irradiated BaFBr:Eu^{2+}," *Journal of Applied Physics*, vol. 64, no. 3, pp. 1405–1412, 1988.

[121] E. Borg and H. G. Gröndahl, "On the dynamic range of different X-ray photon detectors in intra-oral radiography. a comparison of image quality in film, charge-coupled device and storage phosphor systems." *Dentomaxillofacial Radiology*, vol. 25, no. 2, pp. 82–88, 1996.

[122] M. Thoms, H. V. Seggern, and A. Winnacker, "Spatial correlation and photostimulability of defect centers in the X-ray-storage phosphor BaFBr:Eu^{2+}," *Physical Review B*, vol. 44, no. 17, p. 9240, 1991.

[123] F. K. Koschnick, J. M. Spaeth, R. S. Eachus, W. G. McDugle, and R. H. D. Nuttall, "Experimental evidence for the aggregation of photostimulable centers in BaFBr:Eu^{2+} single crystals by cross relaxation spectroscopy," *Physical Review Letters*, vol. 67, no. 25, p. 3571, 1991.

[124] H. Riesen, K. Badek, T. M. Monro, and N. Riesen, "Highly efficient valence state switching of samarium in BaFCl:Sm nanocrystals in the deep UV for multilevel optical data storage," *Optical Materials Express*, vol. 6, no. 10, pp. 3097 – 3108, 2016.

[125] H. P. Beck, "A study on mixed halide compounds MFX (M = Ca, Sr, Eu, Ba; X = Cl, Br, I)," *Journal of Solid State Chemistry*, vol. 17, no. 3, pp. 275–282, 1976.

[126] J. C. Gacon, G. Grenet, J. C. Souillat, and M. Kibler, "Experimental and calculated energy levels of Sm^{2+}:BaClF," *The Journal of Chemical Physics*, vol. 69, no. 2, pp. 868–880, 1978.

[127] J. Qiang, L. Yongsheng, L. Renfu, L. Liqin, L. Wenqin, and C. Xueyuan, "Optical spectroscopy of Eu^{3+}-doped BaFCl nanocrystals," *The Journal of Physical Chemistry C*, vol. 113, no. 6, pp. 2309–2315, 2009.

[128] J. M. Rey, H. Bill, H. Hagemann, and F. Kubel, "Ordering of the heavy anions in mixed $BaFBr_{0.5}I_{0.5}$ crystals: Experimental results," *Physical Review B*, vol. 72, no. 18, p. 184107, 2005.

[129] Y. Shen and K. L. Bray, "Effect of pressure and temperature on 4f- 4f luminescence properties of Sm^{2+} ions in MFCl crystals (M = Ba, Sr, and Ca)," *Physical Review B*, vol. 58, no. 18, p. 11944, 1998.

[130] M. Falin, H. Bill, and D. Lovy, "EPR of Sm^{3+} in BaFCl single crystals," *Journal of Physics: Condensed Matter*, vol. 16, no. 8, p. 1293, 2004.

[131] Z. J. Kiss and H. A. Weakliem, "Stark effect of 4f states and linear crystal field in BaCiF:Sm^{2+}," *Physical Review Letters*, vol. 15, no. 10, p. 457, 1965.

[132] Z. Liu, T. Massil, and H. Riesen, "Spectral hole-burning properties of Sm^{2+} ions generated by X-rays in BaFCl:Sm^{3+} nanocrystals," *Physics Procedia*, vol. 3, no. 4, pp. 1539–1545, 2010.

[133] Z. Liu, M. A. Stevens-Kalceff, X. Wang, and H. Riesen, "Mechanochemical synthesis of nanocrystalline BaFCl:Sm^{3+} storage phosphor by ball milling," *Chemical Physics Letters*, vol. 588, pp. 193–197, 2013.

[134] Z. Liu, M. Stevens-Kalceff, and H. Riesen, "Photoluminescence and cathodoluminescence properties of nanocrystalline BaFCl:Sm^{3+} X-ray storage phosphor," *The Journal of Physical Chemistry C*, vol. 116, no. 14, pp. 8322–8331, 2012.

[135] L. Zhang, J. Yu, and S. Huang, "Fluorescence line narrowing and inhomogeneous broadening of Sm^{2+} in $BaFCl_xBr_{1-x}$," *Journal of Luminescence*, vol. 45, no. 1-6, pp. 301–303, 1990.

[136] J. Zhang, N. Riesen, L. T. Kasim, K. Badek, and H. Riesen, "Mechanochemical preparation of nanocrystalline metal halide phosphors," *Journal of Materials Science*, vol. 53, no. 19, pp. 13 643–13 659, 2018.

[137] C. Wei, S. Huang, and J. Yu, "Two-photon hole burning and fluorescence-line-narrowing studies on $BaFCl_{0.5}Br_{0.5}$:Sm^{2+} at 77 K," *Journal of Luminescence*, vol. 43, no. 3, pp. 161–166, 1989.

[138] R. Jaaniso and H. Bill, "Room temperature persistent spectral hole burning in Sm-doped $SrFCl_{1/2}Br_{1/2}$ mixed crystals," *Europhysics Letters*, vol. 16, no. 6, p. 569, 1991.

[139] X. Wang, Z. Liu, M. A. Stevens-Kalceff, and H. Riesen, "A facile method for the preparation of Eu^{2+}-doped nanocrystalline BaFCl," *Materials Research Bulletin*, vol. 48, no. 10, pp. 369–3694, 2013.

[140] J. Zhang and H. Riesen, "Controlled generation of Tm^{2+} ions in nanocrystalline BaFCl:Tm^{3+} by X-ray irradiation," *The Journal of Physical Chemistry A*, vol. 121, no. 4, pp. 803–809, 2017.

[141] M. Xian-guo, W. Yong-sheng, S. Li, J. Hui, and Z. Lin, "Optical storage studies on the trapping states of BaFCl:Eu^{2+}," *Journal of Physics: Condensed Matter*, vol. 15, no. 14, p. 2407, 2003.

[142] W. Chen, N. Kristianpoller, A. Shmilevich, D. Weiss, R. Chen, and M. Su, "X-ray storage luminescence of BaFCl:Eu^{2+} single crystals," *The Journal of Physical Chemistry B*, vol. 109, no. 23, pp. 11 505–11 511, 2005.

[143] P. Leblans, L. Struye, and P. Willems, "A new needle-crystalline computed radiography detector," *Journal of Digital Imaging*, vol. 13, no. 1, pp. 117–120, 2000.

[144] H. Vrielinck, F. Loncke, J.-P. Tahon, P. Leblans, P. Matthys, and F. Callens, "Electron nuclear double resonance study of photostimulated luminescence active centers in CsBr:Eu^{2+} medical imaging plates," *Physical Review B*, vol. 83, no. 5, p. 054102, 2011.

[145] M. Inokuti and F. Hirayama, "Influence of energy transfer by the exchange mechanism on donor luminescence," *The Journal of Chemical Physics*, vol. 43, no. 6, pp. 1978–1989, 1965.

[146] J. Zimmermann, S. Hesse, H. von Seggern, M. Fuchs, and W. Knüpfer, "Radiation hardness of CsBr:Eu^{2+}," *Journal of Luminescence*, vol. 114, no. 1, pp. 24–30, 2005.

[147] U. Rogulis, S. Schweizer, S. Assmann, and J.-M. Spaeth, "Ga^{2+} hole centers and photostimulated luminescence in the X-ray storage phosphor RbBr:Ga^{+}," *Journal of Applied Physics*, vol. 84, no. 8, pp. 4537–4542, 1998.

[148] U. Rogulis, S. Schweizer, S. Assmann, and J. M. Spaeth, "Photostimulated luminescence process in the X-ray storage phosphor CsBr:Ga^{+}," *Journal of Applied Physics*, vol. 87, no. 1, pp. 207–211, 2000.

[149] D. Babel, R. Haegele, G. Pausewang, and F. Wall, "Ueber kubische und hexagonale elpasolithe $A^I_2B^IM^{III}F_6$," *Materials Research Bulletin*, vol. 8, no. 12, pp. 1371–1382, 1973.

[150] A. Gros, F. Gaume, and J. C. Gacon, "Synthesis of new luminescent materials activated

with divalent Samarium," *Journal of Solid State Chemistry*, vol. 36, no. 3, pp. 324–330, 1981.

[151] A. Meijerink and G. J. Dirksen, "Spectroscopy of divalent Samarium in $LiBaF_3$," *Journal of Luminescence*, vol. 63, no. 4, pp. 189 – 201, 1995.

[152] C. T. Xia and C. S. Shi, "$BaLiF_3$ (Eu^{2+}): A promising X-ray storage phosphor," *Materials Research Bulletin*, vol. 32, no. 1, pp. 107–112, 1997.

[153] A. Meijerink, "Spectroscopy and vibronic transitions of divalent Europium in $LiBaF_3$," *Journal of Luminescence*, vol. 55, no. 3, pp. 125 – 138, 1993.

[154] G. Zhu, Q. Yang, X. Shi, W. Zheng, and Y. Liu, "Hydrothermal synthesis and optical properties of Tb/Ce doped barium lithium fluoride," *Optical Materials*, vol. 35, no. 6, pp. 1309 – 1314, 2013.

[155] M. Mortier, J. Y. Gesland, M. Rousseau, F. Auzel, and D. Meichenin, "Ni^{2+}:$BaLiF_3$: A promising RT tunable solid state laser material," *Radiation Effects and Defects in Solids*, vol. 136, no. 1-4, pp. 65 – 68, 1995.

[156] A. M. E. Santo, S. P. Morato, and S. L. Baldochi, "Ni^{2+} distribution in $BaLiF_3$ crystals prepared by the zone-melting technique," *Journal of Crystal Growth*, vol. 203, no. 1-2, pp. 156–162, 1999.

[157] A. Ercoli, A. Scacco, F. Somma, M. Cremona, R. M. Montereali, S. Martelli, G. Petrocco, L. Scopa, R. A. Nunes, and L. C. S. do Carmo, "F-aggregate centres in KCl films," *Radiation Effects and Defects in Solids*, vol. 132, no. 2, pp. 143–155, 1994.

[158] B. Fritz and E. Menke, "Laser effect in KCl with F_A(Li) centers," *Solid State Communications*, vol. 3, no. 3, pp. 61–63, 1965.

[159] L. F. Mollenauer and D. H. Olson, "A broadly tunable CW laser using color centers," *Applied Physics Letters*, vol. 24, no. 8, pp. 386–388, 1974.

[160] T. T. Basiev, S. B. Mirov, and V. V. Osiko, "Room-temperature color center lasers," *IEEE Journal of Quantum Electronics*, vol. 24, no. 6, pp. 1052 – 1069, 1988.

[161] C. R. Riley and W. A. Sibley, "Color centers in $KMgF_3$," *Physical Review B*, vol. 1, no. 6, p. 2789, 1970.

[162] T. P. P. Hall and A. Leggeat, "Defect centres in $KMgF_3$ produced by X-irradiation at room temperature," *Solid State Communications*, vol. 7, no. 22, pp. 1657–1659, 1969.

[163] C. R. Riley, S. I. Yun, and W. A. Sibley, "Luminescence from color centers in $KMgF_3$," *Physical Review B*, vol. 5, no. 8, p. 3285, 1972.

[164] L. Prado, L. Gomes, S. L. Baldochi, S. P. Morato, and N. D. V. Jr, "Electron-irradiation-induced defects in crystals," *Journal of Physics: Condensed Matter*, vol. 10, no. 37, p. 8247, 1998.

[165] L. Prado, L. Gomes, S. L. Baldochi, S. P. Morato, and J. N. D. Vieira, "F-aggregate centers formation in $BaLiF_3$ crystals," *Radiation Effects and Defects in Solids*, vol. 149, no. 1-4, pp. 249–255, 1999.

[166] I. Tale, P. Kulis, U. Rogulis, V. Tale, J. Trokss, A. Veispals, M. Barboza-Flores, and H. J. Fitting, "Colour centres in $LiBaF_3$," *Journal of Luminescence*, vol. 72, pp. 722–723, 1997.

[167] A. Podinsh and W. A. Sibley, "Radiation-defect absorption in $RbMgF_3$," *Physical Review B*, vol. 18, no. 11, p. 5921, 1978.

[168] J. Nahum and D. A. Wiegand, "Optical properties of some F-aggregate centers in LiF," *Physical Review*, vol. 154, no. 3, p. 817, 1967.

[169] J. Zhang and H. Riesen, "Mechanochemical preparation of nanocrystalline $NaYF_4$:Gd^{3+}/Yb^{3+}/Tm^{3+}: An efficient upconversion phosphor," *Chemical Physics Letters*, vol. 641, pp. 1–4, 2015.

[170] *MAUD:Material Analysis Using Diffraction*, (accessed August, 2017). [Online]. Available: http://maud.radiographema.eu

[171] SpringerMaterials. [Online]. Available: https://materials.springer.com

[172] C. A. Schneider, W. S. Rasband, and K. W. Eliceiri, "NIH Image to ImageJ: 25 years of image analysis," *Nature methods*, vol. 9, no. 7, pp. 671–675, 2012.

[173] *Fluromax-3*, 2001. [Online]. Available: https://www.horiba.com/fileadmin/uploads/Scientific/Downloads/UserArea/Fluorescence/Legacy/Total_FluoroMax3_Manual.pdf

[174] W. S. Slutter, J. Marcovecchio, R. E. Heinz, and D. A. Kolb, "Czerny-turner monochromator," 1993, US Patent 5,192,981.

[175] *Quantum DesignInc.Physical Property Measurement System (PPMS)*. [Online]. Available: https://www.qdusa.com/products/ppms.html

[176] S. L. Baldochi, K. Shimamura, K. Nakano, N. Mujilatu, and T. Fukuda, "Growth and optical characteristics of Ce-doped and Ce:Na-codoped $BaLiF_3$ single crystals," *Journal of Crystal Growth*, vol. 200, no. 3-4, pp. 521–526, 1999.

[177] S. A. Korba, H. Meradji, S. Ghemid, and B. Bouhafs, "First principles calculations of structural, electronic and optical properties of $BaLiF_3$," *Computational Materials Science*, vol. 44, no. 4, pp. 1265 – 1271, 2009.

[178] V. Luana, A. Costales, and A. M. Pendás, "Ions in crystals: The topology of the electron density in ionic materials. II. the cubic alkali halide perovskites," *Physical Review B*, vol. 55, no. 7, p. 4285, 1997.

[179] J. Zhang and H. Riesen, "Photostimulated and persistent luminescence of samarium ions in BaFCl," *Journal of Luminescence*, vol. 207, pp. 188–194, 2019.

[180] M. Chua, P. A. Tanner, and M. F. Reid, "Energy transfer by electric dipole-magnetic dipole interaction in cubic crystals," *Solid State Communications*, vol. 90, no. 9, pp. 581–583, 1994.

[181] D. Huber, *Laser spectroscopy of solids*. Springer Science & Business Media, 1981, vol. 49.

[182] M. Otmar, K. M. Krämer, and E. van der Kolk, "Efficient luminescent solar concentrators based on self-absorption free, Tm^{2+} doped halides," *Solar Energy Materials and Solar Cells*, vol. 140, pp. 115–120, 2015.

[183] E. P. J. Merkx, M. P. Plokker, and E. van der Kolk, "The potential of transparent sputtered NaI:Tm^{2+}, $CaBr_2$:Tm^{2+}, and CaI_2:Tm^{2+} thin films as luminescent solar concentrators," *Solar Energy Materials and Solar Cells*, vol. 223, p. 110944, 2021.

[184] Q. Jiang, L. H. Liang, and D. S. Zhao, "Lattice contraction and surface stress of fcc nanocrystals," *The Journal of Physical Chemistry B*, vol. 105, no. 27, pp. 6275–6277, 2001.

[185] W. J. Schipper, A. Meijerink, and G. Blasse, "The luminescence of Tm^{2+} in strontium tetraborate," *Journal of Luminescence*, vol. 62, no. 2, pp. 55–59, 1994.

[186] C. Wickleder, "Spectroscopic properties of $SrZnCl_4$:M^{2+} and $BaZnCl_4$:M^{2+} (M = Eu, Sm, Tm)," *Journal of Alloys and Compounds*, vol. 300, pp. 193 – 198, 2000.

[187] A. V. Chadwick, J. H. Strange, G. A. Ranieri, and M. Terenzi, "Studies of ionic motion in perovskite fluorides," *Solid State Ionics*, vol. 9, pp. 555–558, 1983.

[188] N. Chowdhury, N. Riesen, and H. Riesen, "Efficient generation of stable Sm^{2+} in nanocrystalline $BaLiF_3$:Sm^{3+} by UV-and X-irradiation," *The Journal of Physical Chemistry C*, vol. 123, no. 41, pp. 25 477–25 481, 2019.

[189] J. Grimm, O. S. Wenger, K. W. Krämer, and H. U. Güdel, "4f-4f and 4f-5d excited states and luminescence properties of Tm^{2+}-doped CaF_2, $CaCl_2$, $SrCl_2$ and $BaCl_2$," *Journal of Luminescence*, vol. 126, no. 2, pp. 590–596, 2007.

[190] Y. Liu, D. Tu, H. Zhu, E. Ma, and X. Chen, "Lanthanide-doped luminescent nanobioprobes: from fundamentals to biodetection," *Nanoscale*, vol. 5, no. 4, pp. 1369–1384, 2013.

[191] Q. Liu, W. Feng, and F. Li, "Water-soluble lanthanide upconversion nanophosphors: Synthesis and bioimaging applications in vivo," *Coordination Chemistry Reviews*, vol. 273, pp. 100–110, 2014.

[192] T. R. Hinklin, S. C. Rand, and R. M. Laine, "Transparent, polycrystalline upconverting nanoceramics: towards 3-D displays," *Advanced Materials*, vol. 20, no. 7, pp. 1270–1273, 2008.

[193] M. Menyuk, K. Dwight, and J. W. Pierce, "$NaYF_4$:Yb, Er—an efficient upconversion phosphor," *Applied Physics Letters*, vol. 21, no. 4, pp. 159–161, 1972.

[194] K. W. Krämer, D. Biner, G. Frei, H. U. Güdel, M. P. Hehlen, and S. R. Lüthi, "Hexagonal sodium yttrium fluoride based green and blue emitting upconversion phosphors," *Chemistry of Materials*, vol. 16, no. 7, pp. 1244–1251, 2004.

[195] K. Zheng, L. Wang, D. Zhang, D. Zhao, and W. Qin, "Power switched multiphoton upconversion emissions of Er^{3+} in Yb^{3+}/Er^{3+} codoped β-$NaYF_4$ microcrystals induced by 980 nm excitation," *Optics Express*, vol. 18, no. 3, pp. 2934–2939, 2010.

[196] J. Zhao, X. Liu, D. Cui, Y. Sun, Y. Yu, Y. Yang, C. Du, Y. Wang, K. Song, K. Liu, S. Lu, X. Kong, and H. Zhang, "A facile approach to fabrication of hexagonal-phase $NaYF_4$:Yb^{3+}, Er^{3+} hollow nanospheres: formation mechanism and upconversion luminescence," pp. 1813–1819, 2010.

[197] D. Ma, D. Yang, J. Jiang, P. Cai, and S. Huang, "One-dimensional hexagonal-phase $NaYF_4$: controlled synthesis, self-assembly, and morphology-dependent upconversion luminescence properties," *CrystEngComm*, vol. 12, no. 5, pp. 1650–1658, 2010.

[198] C. Duan, L. Liang, L. Li, R. Zhang, and Z. P. Xu, "Recent progress in upconversion luminescence nanomaterials for biomedical applications," *Journal of Materials Chemistry B*, vol. 6, no. 2, pp. 192–209, 2018.

[199] M. Pollnau, D. R. Gamelin, S. R. Lüthi, H. U. Güdel, and M. P. Hehlen, "Power dependence of upconversion luminescence in lanthanide and transition-metal-ion systems," *Physical Review B*, vol. 61, no. 5, p. 3337, 2000.

[200] R. K. Sharma, Y. N. Chouryal, A. I. Slesarev, K. V. Ivanovskikh, I. I. Leonidov, S. Nigam, and P. Ghosh, "A closer look at the defects and luminescence of nanocrystalline fluorides synthesized via ionic liquids: the case of Ce^{3+}-doped BaF_2," *New Journal of Chemistry*, vol. 44, no. 1, pp. 200 – 209, 2020.

[201] L. Lutterotti, R. Vasin, and H. R. Wenk, "Rietveld texture analysis from synchrotron

diffraction images. I. calibration and basic analysis," *Powder Diffraction*, vol. 29, no. 1, pp. 76 – 84, 2014.

[202] M. V. Shestakov, L. F. Chibotaru, V. K. Tikhomirov, V. D. Rodriguez, J. J. Velázquez, and V. V. Moshchalkov, "Theory of the kinetics of luminescence and its temperature dependence for Ag nanoclusters dispersed in a glass host," *Physical Chemistry Chemical Physics*, vol. 15, no. 38, pp. 15 949 – 15 953, 2013.

[203] M. Henke, J. Persson, and S. Kück, "Preparation and spectroscopy of Yb^{2+}-doped $Y_3Al_5O_{12}$, $YAlO_3$, and $LiBaF_3$," *Journal of Luminescence*, vol. 87, pp. 1049–1051, 2000.

[204] Y. Huang, P. Wei, S. Zhang, and H. J. Seo, "Luminescence properties of Yb^{2+} doped $NaBaPO_4$ phosphate crystals," *Journal of the Electrochemical Society*, vol. 158, no. 5, p. H465, 2011.

[205] J. Zhang, N. Riesen, and H. Riesen, "Mechanochemically prepared SrFCl nanophosphor co-doped with Yb^{3+} and Er^{3+} for detecting ionizing radiation by upconversion luminescence," *Nanoscale*, vol. 9, no. 41, pp. 15 958–15 966, 2017.

[206] D. S. McClure and Z. Kiss, "Survey of the spectra of the divalent rare-earth ions in cubic crystals," *The Journal of Chemical Physics*, vol. 39, no. 12, pp. 3251–3257, 1963.

[207] E. Krausz, "Selective and differential optical spectroscopies in photosynthesis," *Photosynthesis research*, vol. 116, no. 2, pp. 411–426, 2013.

[208] A. Gauzzi, H. J. Mathieu, J. H. James, and B. Kellett, "AES, XPS and SIMS characterization of $YBa_2Cu_3O_7$ superconducting high T_c thin films," *Vacuum*, vol. 41, no. 4-6, pp. 870–874, 1990.

[209] A. B. Andrade, N. S. Ferreira, and M. E. G. Valerio, "Particle size effects on structural and optical properties of BaF_2 nanoparticles," *RSC advances*, vol. 7, no. 43, pp. 26 839–26 848, 2017.

[210] S. P. Kowalczyk, F. R. McFeely, L. Ley, R. A. Pollak, and D. A. Shirley, "X-ray photoemission studies of the alkali halides," *Physical Review B*, vol. 9, no. 8, p. 3573, 1974.

[211] C. Ro and R. W. Linton, "Characterization of LiF using XPS," *Surface Science Spectra*, vol. 1, no. 3, pp. 277–283, 1992.

[212] H. Riesen and A. Szabo, "Revisiting the temperature dependence of the homogeneous R_1 linewidth in ruby," *Chemical Physics Letters*, vol. 484, no. 4-6, pp. 181–184, 2010.

[213] X. Chen and B. D. Bartolo, "Phonon effects on sharp luminescence lines of Nd^{3+} in $Gd_3Sc_2Ga_3O_{12}$ garnet (GSGG)," *Journal of luminescence*, vol. 54, no. 5, pp. 309–318, 1993.

[214] B. G. Yalcin, B. Salmankurt, and S. Duman, "Investigation of structural, mechanical, electronic, optical, and dynamical properties of cubic $BaLiF_3$, $BaLiH_3$, and $SrLiH_3$," *Materials Research Express*, vol. 3, no. 3, p. 036301, 2016.

[215] R. Vreeker, S. Kuzakov, and M. Glasbeek, "Electron tunnelling from excited F_2^{2+} centres to F^+ centres in calcium, oxide studied from phosphorescence-microwave double-resonance spectroscopy," *Journal of Physics C: Solid State Physics*, vol. 19, no. 8, p. 1215, 1986.

[216] Y. Zhydachevskii, D. Galanciak, S. Kobyakov, M. Berkowski, A. Kamińska, A. Suchocki, Y. Zakharko, and A. Durygin, "Photoluminescence studies of Mn^{4+} ions in $YAlO_3$ crystals at ambient and high pressure," *Journal of Physics: Condensed Matter*, vol. 18, no. 49, p. 11385, 2006.

[217] P. Kottis and R. Lefebvre, "Calculation of the electron spin resonance line shape of randomly oriented molecules in a triplet state. I. the $\Delta m = 2$ transition with a constant linewidth," *The Journal of Chemical Physics*, vol. 39, no. 2, pp. 393–403, 1963.

[218] P. Kottis and R. Lefebvre, "Calculation of the electron spin resonance line shape of randomly oriented molecules in a triplet state. II. correlation of the spectrum with the zero-field splittings. introduction of an orientation-dependent linewidth," *The Journal of Chemical Physics*, vol. 41, no. 2, pp. 379–393, 1964.

[219] D. J. Gravesteijn and M. Glasbeek, "Optically detected magnetic resonance and spin

coherence in the phosphorescent state of exchange-coupled F^+-center pairs in CaO," *Physical Review B*, vol. 19, no. 11, p. 5549, 1979.

[220] T. Sizova, E. Radzhabov, R. Shendrik, A. Egranov, and A. Myasnikova, "Optical absorption spectra of X-ray irradiated alkaline earth fluoride crystals doped with divalent rare-earth ions studied by thermal bleaching," *Radiation Measurements*, vol. 125, pp. 25–28, 2019.

[221] X. Wang and H. Riesen, "Mechanochemical synthesis of an efficient nanocrystalline BaFBr:Eu^{2+} X-ray storage phosphor," *RSC advances*, vol. 5, no. 104, pp. 85 506–85 510, 2015.

[222] X. L. Wang, M. A. Stevens-Kalceff, and H. Riesen, "Mechanochemical preparation of nanocrystalline BaFCl doped with samarium in the 2+ oxidation state," *Inorganic chemistry*, vol. 53, no. 17, pp. 8839–8841, 2014.

[223] H. P. Trommsdorff, A. Corval, and L. V. Laue, "Spectral hole burning: Spontaneous and photoinduced tunneling reactions in low temperature solids," *Pure and Applied Chemistry*, vol. 67, no. 1, pp. 191–198, 1995.

[224] X. Wang, H. Riesen, M. A. Stevens-Kalceff, and R. Rajan, "Room temperature hole-burning of X-ray induced Sm^{2+} in nanocrystalline $Ba_{0.5}Sr_{0.5}FCl_{0.5}Br_{0.5}$:$Sm^{3+}$ prepared by mechanochemistry," *The Journal of Physical Chemistry A*, vol. 118, no. 40, pp. 9445–9450, 2014.

[225] E. Banks, A. M. Srivastava, and A. Halperin, "Different sites for divalent europium luminescence in $BaMgF_4$," *Journal of Solid State Chemistry*, vol. 67, no. 1, pp. 104–108, 1987.

[226] F. Preishuber-Pflügl and M. Wilkening, "Evidence of low dimensional ion transport in mechanosynthesized nanocrystalline $BaMgF_4$," *Dalton Transactions*, vol. 43, no. 26, pp. 9901–9908, 2014.

[227] B. P. Kore, S. Tamboli, N. S. Dhoble, A. K. Sinha, M. N. Singh, S. J. Dhoble, and H. C.

Swart, "Efficient resonance energy transfer study from Ce 3þ to Tb 3þ in $BaMgF_4$," *Materials Chemistry and Physics*, vol. 30, p. 1e12, 2016.

[228] J. R. G. Thorne, A. Karunathilake, H. Choi, R. G. Denning, and T. Luxbacher, "Two-photon spectroscopy of Samarium (III) in the elpasolite Cs_2NaYCl_6:Sm^{3+}," *Journal of Physics: Condensed Matter*, vol. 11, no. 40, p. 7867, 1999.